PHYSICS OF THE CURRENT INJECTION PROCESS DURING LOCALIZED HELICITY INJECTION

by

Edward Thomas Hinson

A dissertation submitted in partial fulfillment of

the requirements for the degree of

Doctor of Philosophy

(Nuclear Engineering and Engineering Physics)

at the

UNIVERSITY OF WISCONSIN–MADISON

2015

Date of final oral examination: 10/16/2015

The dissertation is approved by the following members of the Final Oral Committee:
David Anderson, Jim and Anne Sorden Professor, Electrical and Computer Engineering
James Blanchard, Duane H. and Dorothy M. Bluemke Professor, Engineering Physics
Raymond Fonck, Steenbock Professor in Physical Science, Engineering Physics
Chris Hegna, Professor, Engineering Physics
John Sarff, Professor, Physics

Abstract

An impedance model has been developed for the arc-plasma cathode electron current source used in localized helicity injection tokamak startup. According to this model, a potential double layer (DL) is established between the high-density arc plasma ($n_{arc} \sim 10^{21}\,\mathrm{m}^{-3}$) in the electron source, and the less-dense external tokamak edge plasma ($n_{edge} \sim 10^{18}\,\mathrm{m}^{-3}$) into which current is injected. The DL launches an electron beam at the applied voltage with cross-sectional area close to that of the source aperture: $A_{inj} \approx 2\,\mathrm{cm}^2$. The injected current, I_{inj}, increases with applied voltage, V_{inj}, according to the standard DL scaling, $I_{inj} \sim V_{inj}^{3/2}$, until the more restrictive of two limits to beam density n_b arises, producing $I_{inj} \sim V_{inj}^{1/2}$, a scaling with beam drift velocity. For low external tokamak edge density n_{edge}, space-charge neutralization of the intense electron beam restricts the injected beam density to $n_b \sim n_{edge}$. At high J_{inj} and sufficient edge density, the injected current is limited by expansion of the DL sheath, which leads to $n_b \sim n_{arc}$. Measurements of n_{arc}, I_{inj}, n_{edge}, V_{inj}, support these predicted scalings, and suggest n_{arc} as a viable control actuator for the source impedance. Magnetic probe signals ≈ 300 degrees toroidally from the injection location are consistent with expectations for a gyrating, coherent electron beam with a compact areal cross-section. Technological development of the source has allowed an extension of the favorable $I_{inj} \sim V_{inj}^{1/2}$ to higher power without electrical breakdown.

ACKNOWLEDGMENTS

Many people have positively impacted my graduate career. I would like to thank my advisor, Raymond Fonck, both for his sage guidance at crucial junctures during the development of the work described here, and for his cultivation of a dynamic, productive, supportive scientific group. Working at Pegasus has been an honor for which I am very grateful.

I am also grateful to Carl Sovinec and Chris Hegna for their regular attendance at our group meetings, and their insights and critiques over the years. By fortunate coincidence, Dr. Hegna taught almost all of my higher-level plasma courses, which were uniformly excellent. I'd like to acknowledge Greg Winz for teaching me a great deal about vacuum technology and design, and Ben Lewicki for designing power supplies that work well enough that the students can generally focus on other things. Additional thanks goes to both of them for building the injectors described in this work. Ben Ford ensured we all work in a safe lab environment, was generally a jack-of-all-trades, and kept track of the vast tide of pieces and parts that make Pegasus go. Thanks to Mike Bongard, for his reliably precise, careful work, and his excellent feedback. Thanks to Devon Battaglia for the extra guidance he gave when I was still a new student.

The other graduate students - Jayson Barr, Justin Perry, Kathreen Thome, Dinh Truong, Grant Bodner, Nate Woodruff, Mindy Bakken, Matt Kriete and many others, also taught me quite a bit and made Pegasus a fun place to work at. It was a pleasure to spend these years with you. Thanks especially to Galen Burke and Dave Schlossberg for being low-key office mates, helpful research colleagues, and great friends.

Thanks to my parents, for supporting my schooling and raising me to know the joy of learning new things. Lastly, I'd like to thank Dr. Erin Ronayne, for her unflagging encouragement and support. Her companionship has made me a better person.

DISCARD THIS PAGE

Table of Contents

DISCARD THIS PAGE

List of Figures

Figure Page

Figure Page

Figure Page

DISCARD THIS PAGE

List of Tables

Chapter 1

Introduction

1.1 Spherical Tokamaks

Low aspect ratio tokamak designs allow access to a unique and important physics regime. Extremely low aspect ratio “spherical” tokamaks have been considered as candidates for material test facilities, in support of the conventional tokamak program [9, 10]. Spherical tokamaks have much smaller aspect ratio, or toroidal major radius to minor radius, $A \equiv R/a$ compared to conventional tokamaks, and possess key advantages in toroidal field utilization over traditional high-aspect ratio designs. The aspect ratio is reduced by minimizing the vessel’s inner radius, the centerstack radius, so that $A \lesssim 2$. A comparison is shown in Fig. 1.1 of a spherical tokamak (top) to a conventional aspect ratio tokamak (bottom). This is important since available toroidal field (TF) strength is a primary driver of overall device cost.

A number of important figures of merit quantitatively demonstrate what is meant by efficient field utilization and will be reviewed in the following. Low aspect ratio devices possess a large field gradient in the radial direction and magnetic flux lines are concentrated in the higher-field, ’good’ curvature region near the center stack, where kinetic pressure and field energy gradient forces oppose each other. Thus, the shape of the plasma conforms to the center stack. See Fig. 1.1, where a spherical tokamak with this natural shaping effect depicted. This is a stabilizing effect, primarily because more toroidal flux is incorporated into the volume of the plasma, and is quantified with parameters elongation, κ, and triangularity

δ. It is referred to as natural shaping, as it occurs in STs without the additional coils used in conventional tokamaks to enforce roughly the same shape. Due to this conformation to the center stack at the high field side, the edge safety factor q_ψ, which is a key metric for plasma stability, is increased significantly over that of conventional tokamaks.

This inward concentration of field lines in the centerstack region, and natural shaping, allow for higher field line-averaged, effective field strength along a line of flux. STs as a result have access to operation at higher plasma pressures p for a given toroidal field strength B_T. This ratio, quantified with $\beta_t = \frac{<p>}{B_T^2/2\mu_0}$, is a figure of merit which is optimized in low-aspect ratio geometries.

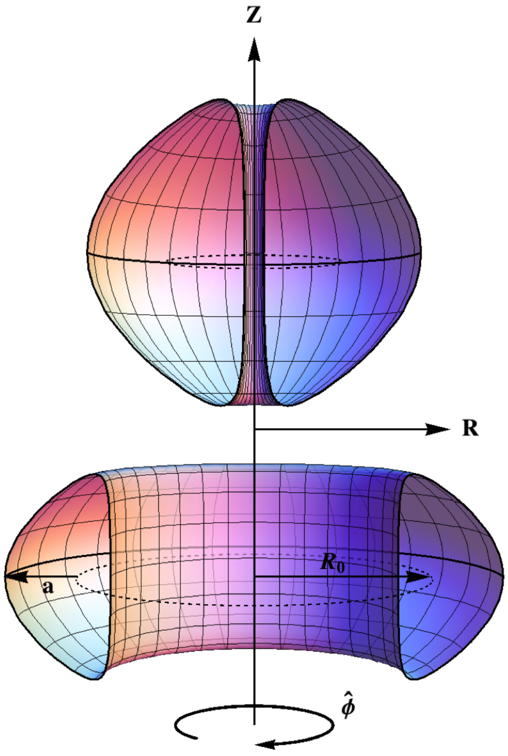

Figure 1.1: High aspect ratio tokamak, spherical tokamak toroidal field comparison. Top: Spherical tokamak with aspect ratio $A = 1.1$ and TF-gradient induced natural elongation. Bottom: A conventional tokamak with $A = 3.7$. Elongation $\kappa = 1.95$ and triangularity $\delta = 0.5$ for both geometries.

The toroidal field gradient also produces highly pitched field lines on the outboard side, and the fields resulting from poloidal currents along these lines of flux generate a strong on-axis paramagnetism [10], which can increase the total field by a factor of two over the vacuum field. Conventional tokamaks typically have paramagnetic enhancements of a few percent.

Another important figure of merit which is optimized in low-aspect ratio devices, normalized plasma current I_N, is given by

$$I_N = \frac{I_p\,[\mathrm{MA}]}{aB_{\phi 0}} = 5A\frac{I_p\,[\mathrm{A}]}{I_{TF}\,[\mathrm{A}]} \tag{1.1}$$

Normalized current is a quantitative measure of the efficiency of the toroidal field in sustaining a stable plasma current. Again the reduction in toroidal field made possible by efficient field utilization makes this parameter very large in low-aspect ratio geometry. Fig. 1.2 shows the toroidal field utilization I_p/I_{TF} operating space of a number of devices at fixed edge q_ψ and elongation as a function of aspect ratio. Clearly, lower aspect ratio devices optimize this figure of merit. High normalized current allows access to operations at high β_t.

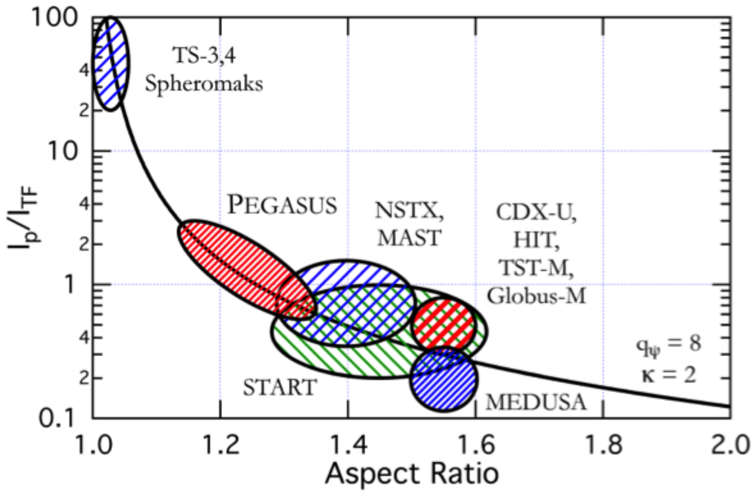

Figure 1.2: Toroidal field utilization factor (at fixed edge q_ψ and elongation κ) vs aspect ratio

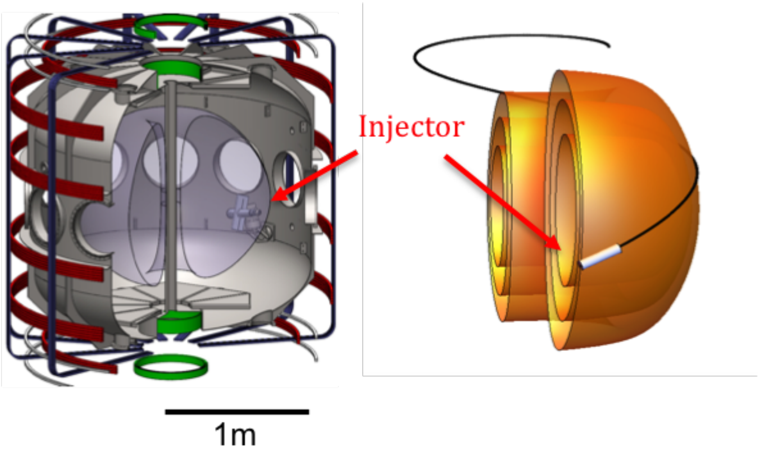

Figure 1.3: Left: Pegasus Toroidal Experiment vacuum vessel with injector and representative plasma. Right: Depiction of plasma and edge stream.

1.2 Spherical Tokamak Startup and Current Growth

1.2.1 Localized Helicity Injection Basics

Alternatives to ohmic induction as a plasma current start-up and drive technique are generally understood to be critical to all future tokamak devices. Problems for traditional high-aspect ratio tokamaks, such as finite ohmic inductive flux swing and spatial constraints, with the need for neutron shielding and breeding blankets, are naturally shared by the spherical tokamak (ST) concept. However, low-aspect ratio geometry forces ohmic solenoid components into a much smaller radius center-stack. Thus, in addition to the fundamental limit to ohmic induction as a steady-state current drive scheme inherent in its pulsed nature, ohmic induction in STs would be more expensive from an engineering standpoint due to their lack of central solenoid cross-sectional area. Namely, achieving the same flux swing within a smaller cross-sectional area device requires a greater field swing, potentially challenging material strength limits. Given the need in nuclear devices for neutron shielding of these components, it is unclear whether ohmic drive would be feasible for a spherical tokamak.

Development of non-inductive forms of start-up are key to the future of the ST concept. In order to address this need, the Pegasus Toroidal Experiment [11], an ultra-low aspect ratio ST ($A = 1.13 - 1.3$), is developing Localized Helicity Injection (LHI) start up.

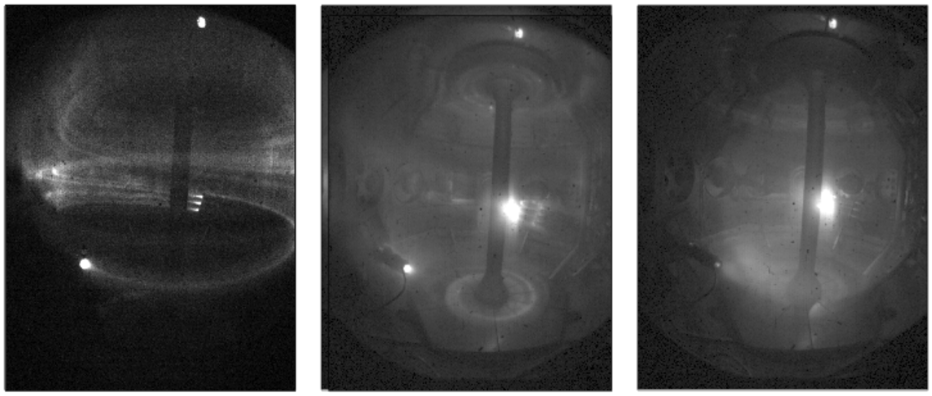

Figure 1.4: Sequence of plasma states in an LHI-initiated ST. Left: Coherent streams. Middle: Tokamak-like plasma driven by continuous LHI. Right: Quiescent plasma after injector shutoff.

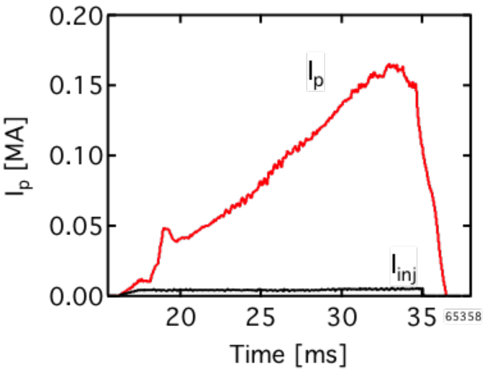

Figure 1.5: Typical LHI discharge, achieving $I_p = 170\,\mathrm{kA}$ from injected current $I_{inj} = 5\,\mathrm{kA}$, produced in Pegasus Toroidal Experiment.

LHI employs current sources, or helicity injectors, to inject current streams parallel to the vacuum field. This is depicted in Fig. 1.3. The injected current is increased until the streams weaken the vacuum field and become unstable. This turbulent system then undergoes Taylor relaxation to become a tokamak-like state. This is indicated in Fig. 1.4, which shows the three stages of LHI-initiated discharge development: 1) Relatively weak coherent current streams follow nominally the vacuum field lines; 2) After relaxation to a tokamak-like state, the current grows through continuous helicity injection; and 3) transition to a MHD-quiescent tokamak plasma upon termination of LHI. The technique can also benefit from added current drive via poloidal field induction as poloidal coils are ramped to values consistent with radial equilibrium for increasing values of I_p. To date, I_p up to 0.18MA have been initiated via LHI with I_{inj}=3.7kA, without any solenoidal induction. An example discharge is shown in Fig. 1.5.

The LHI process creates a plasma with total plasma current many times greater than that expected from injected current following the vacuum field. Resistive MHD simulations suggest that after relaxation, the field line topology is stochastic, but when its current profile is averaged toroidally, the resulting current and field structure resembles that of a tokamak [12]. Simulation and experiment [13, 14] suggest that after injectors are shut off, flux surfaces 'heal' from their stochastic topology, becoming closed and obtaining tokamak-like confinement. As a result, helicity injection can be used as a tokamak startup and current growth scheme despite poor confinement predicted to be present during its use. The healed surfaces enable hand-off to subsequent current drive techniques.

Resistive MHD simulations of LHI accomplished using the NIMROD code have been conducted. These simulations have produced a new phenomenological understanding of the current growth process during LHI. [15, 1] In these simulations, current growth occurs as a result of adjacent passes of a helical current structure produced by the injected streams intermittently reconnecting to inject current rings into the core confinement region. This process is depicted in Fig. 1.6, where a resulting current ring is indicated with a blue arrow. The simulation results are suggestive of many experimental features characteristic of LHI, which will be described in Chapter 5.

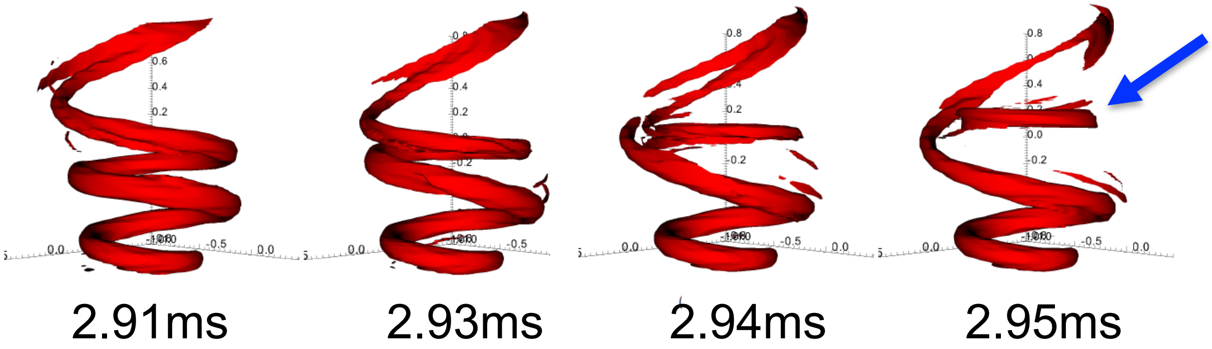

Figure 1.6: From [1], a current filament (red) reconnects to inject a ring (indicated with blue arrow) into the confinement region.

1.2.2 Magnetic Helicity

Helicity is a property of magnetic fields which can be thought of roughly as a measure of the degree of linkedness of the flux tubes. It describes the relation between magnetic topology and current. The mathematical definition of helicity is:[16]

$$K \equiv \int \mathbf{A} \cdot \mathbf{B} \, \mathrm{d}^3 x \tag{1.2}$$

where $\mathbf{B}$ is the magnetic field, and $\mathbf{A}$ the magnetic field vector potential, $\nabla \times \mathbf{A} = \mathbf{B}$.

It is evident from its dependence on $\mathbf{A}$ that helicity must inherit a dependence on gauge selection, but roughly, one may imagine an isolated field line, with implied vector potential circulating about it in the azimuthal direction. Current injected along this field line produces an azimuthal field parallel to the guiding field's $\mathbf{A}$. In addition, the self-field of the current flowing along the field line produces it's own potential $\mathbf{A}$ which is parallel to the original line of flux. This then constitutes positive helicity content (see Fig. 1.7). In real situations, the topology is more complex than this simplified example, but current injection along field lines still constitutes added helicity and vice versa.

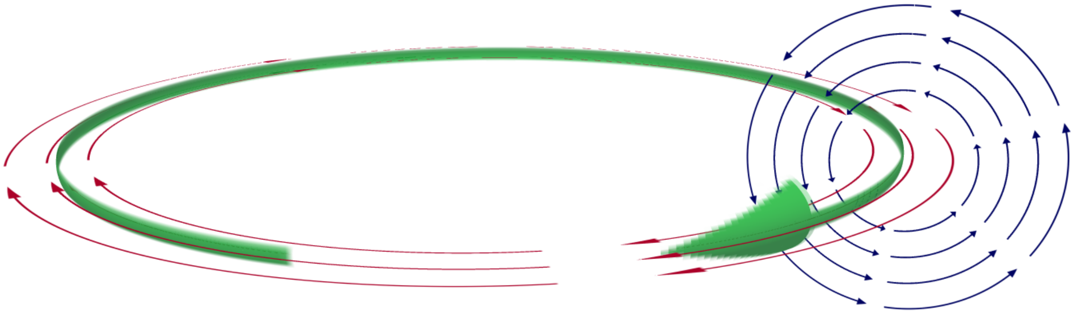

Figure 1.7: Current (large arrow) propagating along toroidal flux creates poloidal flux (right), which links the toroidal flux and constitutes helicity.

1.2.3 Taylor Relaxation and the Conservation of Helicity

Helicity is an important property of magnetic fields in a conductive fluid because of its tendency to dissipate more slowly than magnetic energy content when that fluid experiences turbulence [17, 18]. Magnetic turbulence and field reconnection arising from resistive instabilities reduce stored magnetic energy in an unstable magnetic topology, but on time scales short compared with the resistive timescales over which helicity is conserved. This rapid energy dissipation leaves the plasma in a well-defined lowest energy state, consistent with a given helicity, or field-aligned current. Helicity injection current drive is the process of producing this minimum energy "Taylor state" plasma with a given field-aligned plasma current. It is this plasma configuration which is handed-off to subsequent current drive schemes.

R. J. Taylor has shown [18], in particular for spheromaks and reverse field pinches, which are more prone to resistive instabilities and the energy dissipation that results from them, that the energy-minimized field configurations consistent with helicity conservation are given by eigenfunctions of the "force free" state:

$$\nabla \times \mathbf{B} = \mu_0 \mathbf{J} = \lambda_0 \mathbf{B} \tag{1.3}$$

where λ_0 is the lowest non-zero eigenvalue, and is independent of position. [17, 18] Continuously driven plasmas, with a given fixed value of λ_{edge} imposed at the edge, are expected to fill in, so that internal λ_0 approaches the driven edge value of $\bar{\lambda}_{edge} = \mu_0 I_{inj}/\bar{\psi}_{inj}$, where I_{inj} is injected current at the edge and $\bar{\psi}_{inj}$ is the average flux on the surfaces subject to injection. The result is a tendency for tokamak-like plasma current to increase toward $J \rightarrow \bar{\lambda}_{edge} B/\mu_0$, provided sufficient helicity input.

Whether a plasma relaxes to the Taylor state relies on the condition that its initial configuration be sufficiently unstable to the resistive instabilities which drive the plasma toward a relaxed state. Tokamaks can be quite stable to these resistive instabilities, but in reverse field pinches and spheromaks, and in tokamaks with very unstable edge currents, a Taylor state is expected. In DC helicity injection schemes, very unstable edge currents are injected into a volume where tokamak-like magnetic field boundary conditions are imposed. The injected current undergoes Taylor relaxation to produce a tokamak-like plasma with a λ_0 limited by the driven $\bar{\lambda}_{edge}$. The resultant minimum-energy magnetic topology is tokamak-like, in that it resembles a tokamak's closed, nested flux surface field structure in a toroidally-averaged sense, and possesses properties (such as toroidal plasma current I_p) which depend on injected current and injector properties.

1.3 Plasma Current Limits

The constraints defined above - defined by Taylor state topology and conservation of helicity, can each be used to obtain a limit to tokamak-like plasma current I_p, which depend upon injector and device parameters.

1.3.1 Taylor Relaxation Current Limit

The Taylor relaxation process, where an internal λ_p rises toward an imposed average $\bar{\lambda}_{edge}$ suggests a maximum plasma current at $\lambda_p = \bar{\lambda}_{edge}$. Returning to [18]

$$\nabla \times \mathbf{B} = \mu_0 \mathbf{J} = \lambda \mathbf{B} \tag{1.4}$$

The global nature of λ in the Taylor-relaxed configuration suggests that by imposing a λ_{edge}, one can expect the interior region undergoing turbulence to relax such that its value approaches the imposed edge value:

$$\lambda_p \leq \overline{\lambda}_{edge} \tag{1.5}$$

where this averaged edge value $\bar{\lambda}_{edge}$ results from average poloidal flux, $\bar{\psi}_{edge}$ over the radial width of the injector w at midplane. Using this definition of $\bar{\lambda}_{edge}$ and solving in terms of quantities relevant to tokamak geometry,

$$\frac{\mu_0 I_p}{\Psi} \leq \frac{\mu_0 I_{inj}}{\bar{\psi}_{edge}} \tag{1.6}$$

where Ψ is the areal-average toroidal flux, I_p is plasma current, and I_{inj} is injected current. Using

$$f_G = \left[\left(\frac{\mu_0 I_p / 2\pi a}{B_{z,p} + B_{z,v}} \right) \frac{< B_\phi >}{B_{\phi,0}} \right]^{\frac{1}{2}} \tag{1.7}$$

Eq. 1.6 can be written as [19, 20]:

$$I_p \leq f_G \left(\frac{\varepsilon A_p I_{TF} I_{inj}}{2\pi R_{edge} w} \right)^{\frac{1}{2}} \tag{1.8}$$

where $< B_\phi >$ is the volume-averaged toroidal field, $B_{\phi,0}$ is the on-axis toroidal field, I_{TF} is the toroidal rod current, R_{edge} is the major radius of the plasma edge at midplane, w is the radial width of the injected current region at the midplane edge, A_p is the plasma cross-sectional area, ε is inverse aspect ratio, and $B_{z,inj}$ has been divided into two components, representing contributions of the toroidal plasma current ($B_{z,p}$) and PF coils ($B_{z,v}$). The term f_G is approximately unity for circular, high-aspect ratio plasmas and rises to approximately 3 for large, shaped, low-aspect ratio plasmas. Eq. 1.8 represents the maximum expected current for a Taylor state, and is one key constraint on tokamak-like plasmas created via LHI.

1.3.2 Helicity Balance Current Limit

Helicity can be thought of roughly as a metric for field-aligned current. A conserved quantity of helicity thus implies a specific plasma current. This relationship can be obtained by considering the time derivative of helicity. The integral in Eq. 1.2 can be manipulated to obtain [21]:

$$\frac{dK}{dt} = -2\int_V \mathbf{E}\cdot\mathbf{B}d^3x - 2\frac{\partial\psi}{\partial t}\Psi - 2\int_A \Phi\cdot\mathbf{B}\cdot d\mathbf{S} \tag{1.9}$$

where ψ is the poloidal flux outside the bounding magnetic surface, Ψ the toroidal flux within the integral's bounding surface, and Φ the electric potential between two points on the bounding magnetic surface connected by a field line. B is the open flux magnetic field piercing the bounding magnetic surface, E is the electric field along that magnetic field line. The first term on the the right-hand side is a helicity dissipation term, the second and third surface terms correspond to AC and DC helicity injection, respectively. The dissipation term defines the quantity of helicity removed from the plasma, and thus the minimum injection rate necessary for steady-state helicity content and associated I_p.

Balancing helicity input from a current source in the plasma edge with resistive dissipation in the core in a toroidal configuration that conserves helicity gives a limit to the plasma current in equilibrium. Eq. 1.9 can be rewritten in this case as: [22]

$$I_p = (V_{ind} + V_{eff})\,\frac{A_p}{2\pi R_0 < \eta >} \tag{1.10}$$

where

$$V_{eff} = \frac{A_{inj}B_nV_{inj}}{\mathit{\Psi}} \tag{1.11}$$

where I_p is tokamak plasma current, A_p is the plasma cross-sectional area, R_0 is plasma major radius, $\langle\eta\rangle$ is the volume-averaged resistance, V_{ind} is the inductive loop voltage from poloidal/ohmic induction, A_{inj} is the area of the injector, $\mathit{\Psi}$ is toroidal flux enclosed by the plasma, and B_n is the toroidal field at the location of the injector. V_{eff} is the effective loop voltage resulting from helicity injection, and is a key figure of merit for helicity injection schemes, relating plasma performance and injector construction/operational requirements. Maximum achievable currents in Pegasus helicity-injected discharges have been found to be roughly in accordance with both this and the Taylor relaxation limit. [22]

1.4 Injectors for LHI

As is apparent from Eq. 1.8 and Eq. 1.10, the source used to drive current for LHI exerts crucial impact on the discharge current I_p. Limits to achievable plasma current separately invoke voltage V_{inj} and current I_{inj} of injection, as well as geometric parameters of the injector.

In Pegasus, specially-developed arc plasma cathode electron guns are used for injection. Figure 1.8 shows the implementation. The setup of the sources is conceptually simple, requiring hardware on only a single port at startup, and two DC power supplies. Injection is accomplished using a two-stage circuit topology, with the arc anode and injection cathode joined as a single electrode. The arc stage provides a dense source of electrons for the injection circuit to extract into the edge, along the magnetic field. The injection stage is comprised of the vacuum vessel as the anode, and the arc anode electrode as injection cathode. The arc plasma thus functions as the cathode for the injection circuit. The V_{inj} required to draw current I_{inj} from a the arc plasma cathode is determined by plasma physics.

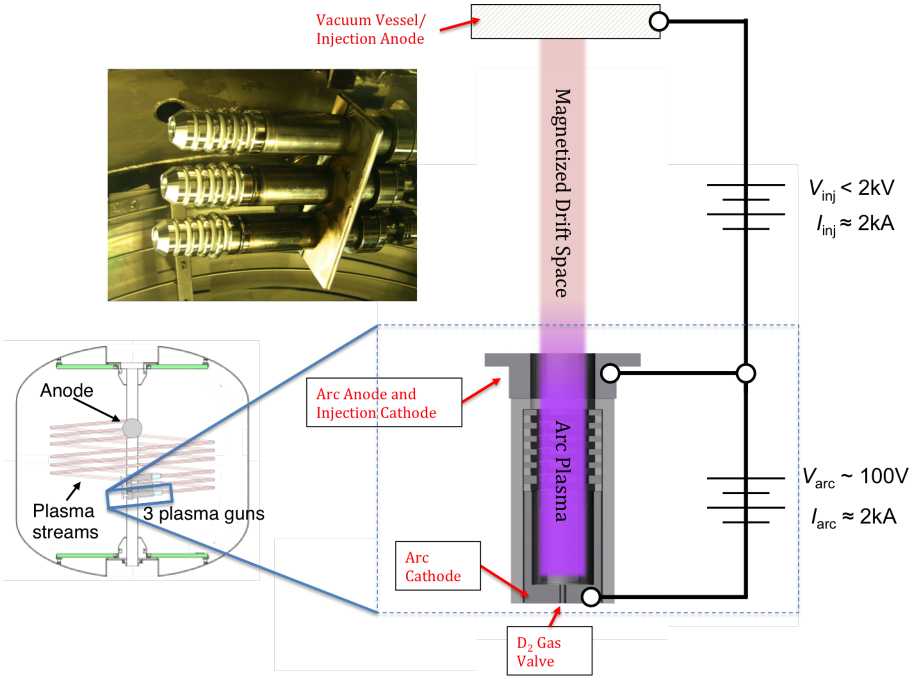

Figure 1.8: Midplane Injection Schematic Left bottom: injectors depicted at their midplane position. Left top: photo of midplane injectors during installation. Right: Schematic diagram cutaway of injector circuit.

1.5 Injector Impedance

Obtaining a target I_p consistent with the limits reviewed above imposes requirements on the injector. Careful optimization of injector parameters A_{inj}, I_{inj}, and V_{inj}, is necessary for efficient maximization of I_p. The limits can have conflicting requirements. For example, the Taylor limit increases with decreasing injector width w, but decreasing it without corresponding increases in its poloidal dimension will reduce A_{inj}, and with it the helicity balance limit. Extending the injector in the poloidal direction is also potentially problematic because it requires assumptions about plasma shaping to maintain coupling to the plasma edge. A smaller injector requires fewer assumptions about plasma geometry, but requires higher applied V_{inj} or lower R_{inj} to maintain helicity input rate.

Plasma-material interactions (PMI) also places constraints on the space in which LHI can operate. While scalings suggest I_p can be increased without bound through increases in I_{inj}

and V_{inj}, PMI processes and arcing can alter the current emission physics and effectively limit these parameters. In particular, above a certain surface electric field threshold, breakdown of the injector cathode occurs, and cathode spots replace the arc plasma as the electron source, sharply lowering V_{inj} and A_{inj}.

The injector impedance is one of the most important unknowns in the I_p limits above, and an understanding of it is required for a predictive model of LHI. The helicity balance limit, depends on relating V_{inj}, and the relaxation limit, depends on I_{inj}. What is not clear is how I_{inj} and V_{inj} are related. Power supplies can impose one of either I_{inj} or V_{inj}, but the physics governing the impedance will set the other quantity. While both limits can in principle be increased arbitrarily by maximizing I_{inj}, and V_{inj}, efficiently balancing these quantities with injector and plasma geometry is necessary to manage the expense of a power supply, which is expected to be largest expense of an LHI system. A predictive model of the impedance will allow an injector design to be built around a predetermined minimum necessary I_{inj}, and V_{inj}. It is the purpose of this work to develop such a predictive impedance model, as part of a broader investigation of the coupling between injector and target plasma.

Chapter 2

Theory

This chapter reviews the injector impedance physics. Plasma cathode electron sources are used for high current electron beam production and are so named because the electron source is not a material electrode surface but a separate plasma. They are known to possess electrostatic space charge double sheaths at the boundary between source plasma and the external plasma into which the beam is launched. Figure 2.1 illustrates the concept.

Limits to the beam density encountered in the sources used here alter the characteristic impedance to a form which is more complex than the simple Child Law behavior of sources described in the relevant literature. These limits to beam density and an impedance model based upon them is reviewed in this chapter.

Finally, the physics governing impedance in practice only applies up to a limit imposed by breakdown of the source. The breakdown process and steps taken to mitigate it is also reviewed.

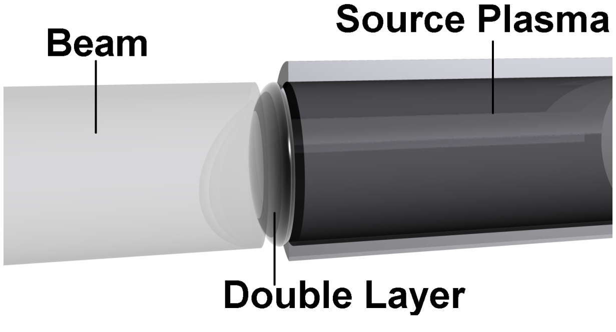

Figure 2.1: Plasma cathode electron source.

2.1 Sheath Impedance Model

C. D. Child [23], and Irving Langmuir [24] were the first researchers to describe space-charge limited currents for electron emission in vacuo from thermionic cathodes, and derive its current-voltage relation. Near the filament, boiled-off electrons are not compensated by corresponding ions, and a negative space charge exists in the emission region. This space charge cloud prevents arbitrary numbers of electrons from leaving the filament.

Irving Langmuir later applied the same concept to ions to describe the ion space-charge sheath that forms at plasma-material boundaries, and as a result it is sometimes called a Langmuir sheath. The form of the equations for ion and electron space charge-limited flow are identical, requiring merely a different substitution for mass, and the general equation has become known as the Child-Langmuir law, or the Three-Halves Power Law. It gives the maximum current density J of a single charged species which can traverse a 1-D (plane parallel) gap. Though real-life geometries can be more complicated, the 1-D case gives good estimates in most cases.

The basic picture underlying the 1-D, plane electrode Child-Langmuir law envisions uncompensated charges traveling in 1-D, as in a vacuum diode, whose mutual repulsion alters the imposed potential structure, impeding flow through the channel and preventing arbitrarily high densities in the region of charge flow. Called a virtual cathode, this potential structure turns back a number of charge carriers, and the gap transitions from a source-limited to a space-charge limited regime. In the case considered by Langmuir and Child, initial velocities of charge carriers into the gap from the cathode are zero, and the only velocities needing accounting for those due to acceleration within the layer. As the emissivity of the cathode increases, the collective charge of the electrons exerts increasing influence on the imposed initial (linear) potential structure in the gap. The space charge limited potential structure is the final self-consistent solution where the charge of the transiting electrons is fully accounted for and increases in charge carriers at the cathode do not result in increased current.

For a singly-charged species s in vacuum (with no other compensating charges) with mass m_s, with current density $J_s = n_s e v_s$ Poisson's equation becomes:

$$-\varepsilon_0 \frac{\mathrm{d}^2 V(x)}{\mathrm{d}x^2} = n_s(x)\, e \tag{2.1}$$

$$\frac{\mathrm{d}^2 V(x)}{\mathrm{d}x^2} = -\frac{1}{\varepsilon_0} \frac{J_s}{\sqrt{2eV(x)/m_s}} \tag{2.2}$$

This non-linear differential equation can be integrated in x across the potential step $V = 0$ to $V = V_0$ from $x = 0$ to $x = d$ to get:

$$V_0^{3/2} = d^2 \frac{9}{4} \frac{1}{\varepsilon_0} \frac{J_s}{\sqrt{2e/m_s}} \tag{2.3}$$

which is typically solved for J_s to obtain:

$$J_s = \frac{4}{9} \varepsilon_0 \sqrt{\frac{2e}{m_s}} \frac{V_0^{3/2}}{d^2} \tag{2.4}$$

This equation has very general applications in a wide variety of contexts. It applies in vacuum, in plasma, in insulating dielectrics, in solid state devices, and in astrophysical contexts. It applies across gaps of several cm found in typical vacuum diodes, and across sheath 'gaps' of some $\lambda_{De} \sim 10^{-5}$ m found in this work.

2.1.1 Plasma Double Layers

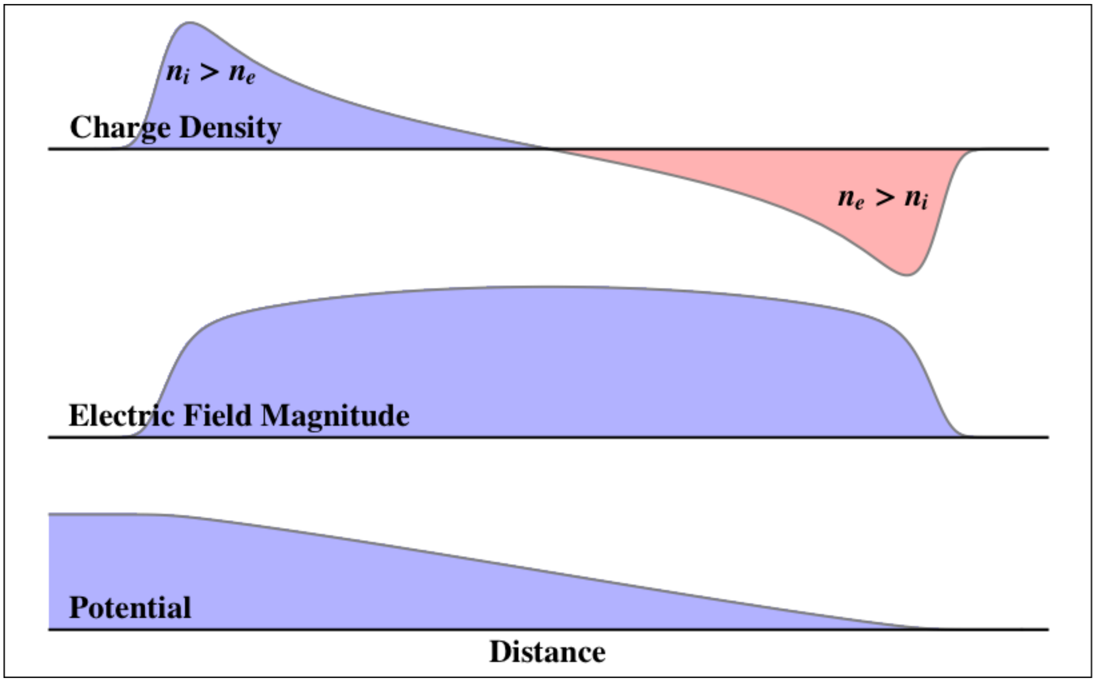

Figure 2.2: Illustrative schematic of charge, field and potential as a function of distance across a double layer.

A double layer (DL) is a space charge layer in plasma - a sheath - which can be thought of as an ion space-charge layer ’sandwiched’ against an electron space charge layer. It was also discovered by Irving Langmuir. [25]. Fig. 2.2 shows an illustrative diagram of charge density, electric field and potential for a double layer, which differs from a single layer in that the electric field is zero at both boundaries. Unlike the ion sheath, familiar from most plasma-surface interfaces, double layers rely on bipolar flow of electrons and ions, and tend to occur within plasmas, where the counter-streaming particle species exist in equilibrium. The net current through a double layer is roughly twice the sum of the current through two single layer sheaths calculated according to formula Eq. 2.4, due to partial neutralization provided by the neighboring, oppositely-charged sheaths. [26]

Examples of double layers arise from a large group of effects. They are observed to often form at the interface between very different types of plasma, such as along strong density and field gradients. They tend to form in current-carrying systems, and when currents are field-aligned, as for example in the Earth's magnetosphere, where so-called Birkeland currents of accelerated particles flow along the lines of the Earth's magnetic field. Double layers are important in basic plasma physics research [27], and in astrophysical plasmas [28].

Double layers are also widely observed in plasma-filled particle beam devices [29, 30]. These devices create an internal plasma separate from that in an external injection region. A space charge layer forms between the two plasmas, over which the applied potential then falls. The voltage drop over the layer is used as the electron or ion beam's accelerating potential. The double layer functions as a load within the circuit, efficiently transferring energy from the voltage imposed along the current stream into directed kinetic energy of the charge-carriers. The load is not dissipative, in contrast with ohmic resistance, which converts energy from the circuit into thermal energy. [28] The setup is depicted conceptually in Fig. 2.3, which shows a plasma-cathode electron beam device of the type used in this work. A strong density gradient exists in the double layer-containing region, where it exists as a boundary layer between the two plasmas.

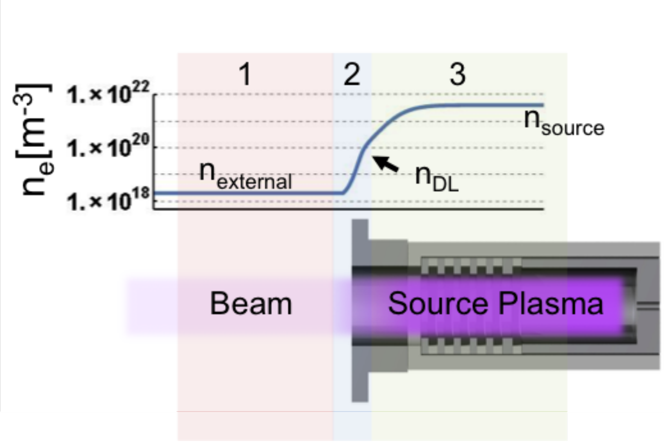

Figure 2.3: Plasma-cathode electron beam device with representative density profile for various numbered regions: 1: external beam-plasma region 2: double layer acceleration region, and 3: source plasma region.

Irving Langmuir was the first to describe double layers in experiments with highly emissive cathodes [25], in which he derived a simple analytic solution for the double layer current.

Only the charge of the two passing species is considered, with distance across the layer denoted as x, $n_s\left(x\right)e = J_s/v_s\left(x\right)$. This simplification is convenient because it allows one to neglect details of velocity distributions of particles on either side of the double layer, but is not accurate at the boundaries $x = \{0, d\}$ since there, prior to acceleration, particles have $v_s\left(x\right) = 0$, J_s finite, and $n_s\left(x\right)$ infinite.

For all points x in the layer, Poisson's equation gives:

$$-\varepsilon_0 \frac{d^2 V\left(x\right)}{d^2 x} = n_i\left(x\right)e - n_e\left(x\right)e \tag{2.5}$$

$$-\varepsilon_0 \frac{d^2 V\left(x\right)}{d^2 x} = \frac{J_i}{\sqrt{\frac{2e\left(V_{DL}-V(x)\right)}{m_i}}} - \frac{J_e}{\sqrt{\frac{2eV(x)}{m_e}}} \tag{2.6}$$

Integration of the above equation [28] from $x = 0$ to $x = d$ and $V = 0$ to $V = V_{DL}$ gives Langmuir's formula for current density through a strong double layer as a function of double layer potential V_{DL}:

$$J = J_e + J_i = \frac{4}{9}\left(1 + \sqrt{\frac{m_e}{m_i}}\right) C_0 \varepsilon_0 \sqrt{\frac{2e}{m_e}} \frac{V_{DL}^{3/2}}{d^2} \tag{2.7}$$

With integration constant $C_0 \approx 1.86$, and the thickness d some number of Debye lengths, $d = \chi\lambda_{De}$. Since the number of Debye lengths χ is uncertain, and this uncertain quantity is squared, the formula is more useful for testing parametric dependences than for obtaining exact, absolute numbers.

2.1.2 Double Layer Sheath Expansion

Double layers are categorized according to strength, eV_{DL}/kT_e, with the voltage drop over the layer, V_{DL}, compared to the electron temperature T_e of the ambient plasma. Weak double layers have $eV_{DL} \sim kT_e$, while strong double layers have $eV_{DL} \gg kT_e$. Simulations of strong double layers have found that sheath width, χ, increases approximately as $V_{DL}^{1/2}$. See Fig. 2.4, from data in [2] and reproduced in [27]. This graph shows the behavior of normalized sheath width χ, found in simulation, depicting its growth as a function of eV_{DL}/kT_e. The $\chi \sim \sqrt{eV_{DL}/kT_e}$ trend for this particular simulation is indicated with a dashed line. These results are not atypical - simulations broadly find[31] that thickness of strong double layers scales as

$$d^2 = \frac{eV_{DL}}{T_e}\frac{\lambda^2_{De,DL}}{\alpha} \tag{2.8}$$

where α is a constant of order 0.1 and temperature and Debye length refers to conditions on the upstream, high-electron density side (electron source). When this scaling is inserted into Eq. 2.7 and geometric constants are eliminated, the expected scaling at high voltage is altered to

$$I_{inj} = (\alpha n_{DL})\, e\sqrt{\frac{2e}{m_e}} V_{inj}^{1/2} A_{inj} \propto n_{DL} V_{inj}^{1/2} \tag{2.9}$$

It is useful to introduce a quantity n_b which scales as the beam density, calculated as the charge carrier density of a monoenergetic beam with drift velocity given by $v_e = \sqrt{\frac{2eV_{inj}}{m_e}}$ with uniform current profile exiting a certain cross-sectional area A_{inj}:

$$n_b = \frac{I_{inj}}{e\sqrt{\frac{2eV_{inj}}{m_e}} A_{inj}} \tag{2.10}$$

Eq. 2.9 can readily be simplified by inserting n_b, indicating that during sheath expansion, beam density is fixed so that $n_b = \alpha n_{DL}$.

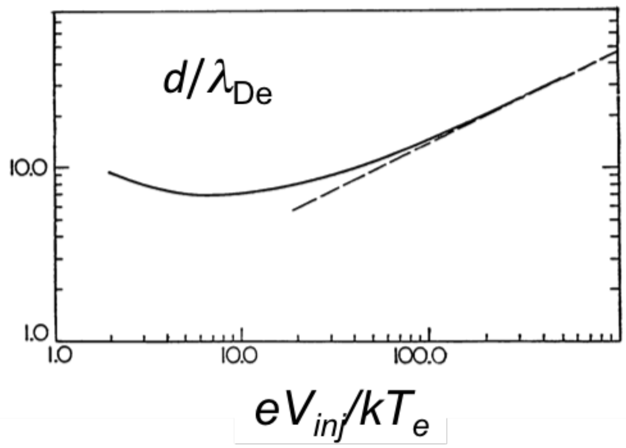

Figure 2.4: From [2], double layer thickness d in units of λ_{De} vs applied voltage.

2.1.3 Beam Charge Neutralization

In addition to this density limit, there is a second density limit imposed by the background plasma density into which the beam must propagate. In general, charged particle beams require a sufficient number of particles of the opposite sign to neutralize beam charge and enable stable propagation into the target region, which in this case is the tokamak edge plasma. The criterion for minimum tolerable neutralization fraction for an electron beam to propagate stably despite its space charge can be obtained by equating the self-pinch force and Coulomb repulsion felt by a test electron at the beam envelope r_{beam}. This gives, in terms of the Lorentz factor γ and the associated densities

$$-F_{Lorentz} = F_{Coulomb} \tag{2.11}$$

$$ev\frac{\mu_0 I}{2\pi r_{beam}} = e\frac{2e\left(n_e - n_i\right)\pi r_{beam}^2}{4\pi\varepsilon_0 r_{beam}} \tag{2.12}$$

$$\frac{v^2}{c^2}n_e = \left(n_e - n_i\right) \tag{2.13}$$

$$\frac{n_i}{n_e} \geq \frac{1}{\gamma^2} \approx 1 \tag{2.14}$$

for the case of a non-relativistic 1kV beam. Thus, non-relativistic propagation requires essentially total quasineutrality. At low energy, additional applied field does little to change this result. If this condition is violated in an unmagnetized beam, space charging will induce radial expansion, or 'beam blowup.' In the presence of a strong guide magnetic field, 1-D behavior is enforced, and charging along the drift space turns electrons back, creating a virtual cathode, and preventing propagation.

When the beam density n_b approaches the density of the background drift space, here assumed to be the tokamak edge plasma density, n_{edge}, (see Fig. 1.8 on page 13) quasineutrality in the magnetized edge region (the beam drift space) limits n_b to equal n_{edge}. Increases in I_{inj} only come with increases in the beam drift velocity v, giving:

$$I_{inj} = n_{edge}evA_{inj} \propto n_{edge}V^{1/2} \tag{2.15}$$

Use of Eq. 2.10 indicates that for this limit, n_b is constrained to $n_b = n_{edge}$.

2.1.4 Impedance Model from Space-Charge Effects

The forgoing limits to propagation from sheath expansion Eq. 2.9 and beam neutralization Eq. 2.15 exist simultaneously in practice, and therefore one expects the most restrictive of the two limits to apply. The limit encountered in practice will simply be the lower of the two for a given source and target configuration. This is reflected in the expression for beam density:

$$n_b = \min\left[n_{edge}, \alpha n_{DL}\right] \tag{2.16}$$

As mentioned, n_{DL} is the plasma density in the double layer's upstream (high density) side. Because the double layer in a plasma cathode electron source is created in residual source plasma, (see Fig. 2.3), it is expected to be proportional to the density of the source. For this work, a plasma arc was used as the source plasma. Therefore, it is expected that $n_{DL} \propto n_{arc}$. Eq. 2.16 becomes

$$n_b = \min\left[n_{edge}, \beta n_{arc}\right] \tag{2.17}$$

with the corresponding I-V relation then simply,

$$I_{inj} = \min\left[n_{edge}, \beta n_{arc}\right] e\sqrt{2e/m_e} V_{inj}^{1/2} \tag{2.18}$$

This equation has the fortunate property that the single unknown term $\min\left[n_{edge}, \beta n_{arc}\right]$ is proportional to the easily-measurable power supply quantity $I_{inj}/\sqrt{V_{inj}} \propto n_b = \min\left[n_{edge}, \beta n_{arc}\right]$. The parametric plot of quantity n_b as it moves between regimes limited by each density is expected to have the structure depicted in Fig. 2.5.

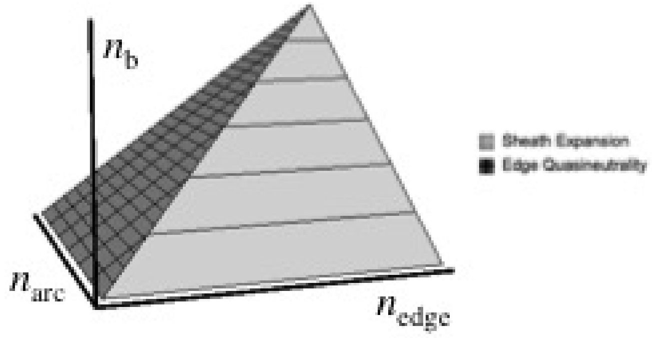

Figure 2.5: Phase space plot of impedance figure of merit n_b. Contours represent expected dependences for constant n_{arc}

2.2 Cathode Spots and Sheath Breakdown

While the intended source of electrons from plasma cathode electron injectors such as in Fig. 2.3 is from an internal source plasma, breakdown can induce electron emission from the electrodes. Plasma-cathode electron devices launch electrons by applying a potential (the injection voltage) between a source and external plasma, and in practice they must do this by means of biased material electrodes. The double layer described above accelerates particles at the applied injection voltage because the injection cathode potential and internal source plasma potential are similar. However, because of this, when the injection cathode contacts the external plasma, the applied injection voltage also falls across its sheath. Figure 2.6 shows this geometry, including the two plasma regions (external, internal), the injection cathode, and the electric field in the sheath between injection cathode and external plasma.

When the electric field in the sheath between injection cathode and external plasma reaches magnitudes in the range $E_{cathode,br} \sim 10^5$ V/cm, depending on surface conditions, sheath breakdown via cathode spots can occur [32, 33, 34, 8, 35, 36]. Plasma conditions at the injection cathode set local Debye length, which is the scale length for the sheath over which the applied injection voltage falls - $E_{cathode} \sim V_{inj}/\lambda_{De}$. For example, if the external plasma density is order $n_e \sim 10^{18}\,\mathrm{m}^{-3}$ and $T_e \sim 10\,\mathrm{eV}$, then sheath width can be expected to be $\sim 100\,\mu\mathrm{m}$, and maximum allowable voltages before breakdown are thus order $V_{br} \sim 1000\,\mathrm{V}$.

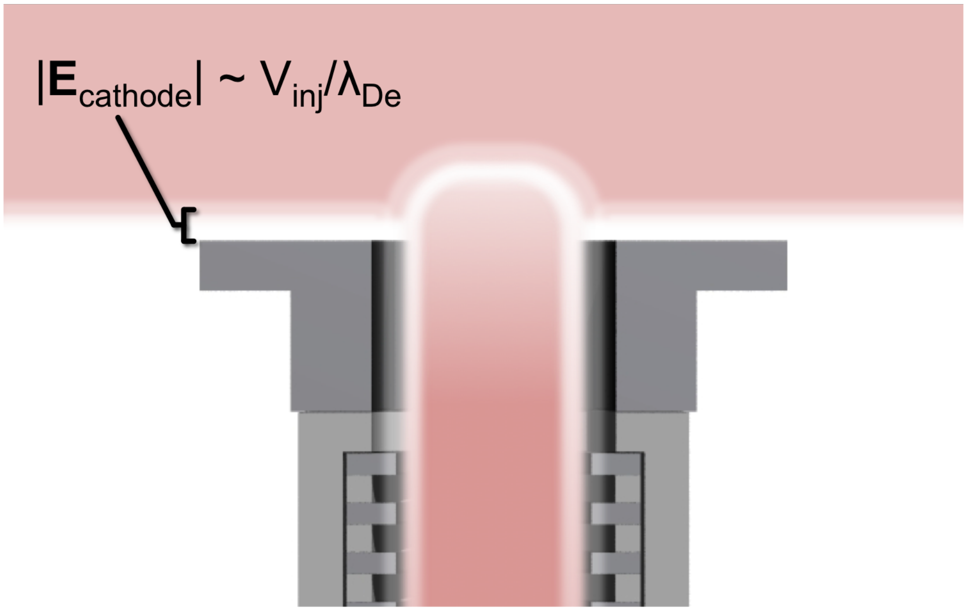

Figure 2.6: Illustration of electrically-stressed material electrode surface.

Cathode spot emission is a mode of cathode attachment of arc discharges which occurs on cold material conductors, prior to a bulk thermionic mode, and when pure field emission is not possible. It is a universal effect in pulsed power devices, as it is the breakdown mechanism on metal electrodes that sets their nominal (high-vacuum) upper-limiting electric field tolerance of $E_{br} \approx 10^7$ V/cm [36, p34]. Reduced breakdown voltage in the presence of plasma is generally assumed to be a result of charging/evaporation of surface films and inclusions by ion flux. [36, 34]

Breakdown via cathode spots sets the most stringent upper limit to V_{inj} during LHI. Cathode spots are self-sustaining, and after breakdown they will replace whatever fraction of the current is necessary to lower the sheath voltage at the injector to their burning voltage of ~ 10 V. This form of electron emission is detrimental to LHI because in addition to significantly reducing V_{inj}, they migrate to insulator surfaces where they cause corrosion and release significant impurities, and can ignite secondary discharge and arcing that causes damage to injector hardware. They emit electrode material as vapor/particle spray, and reduce effective injection area A_{inj}. Fig. 2.7 shows an example of cathode spots induced on a molybdenum electrode.

2.2.1 Cathode Spot Properties

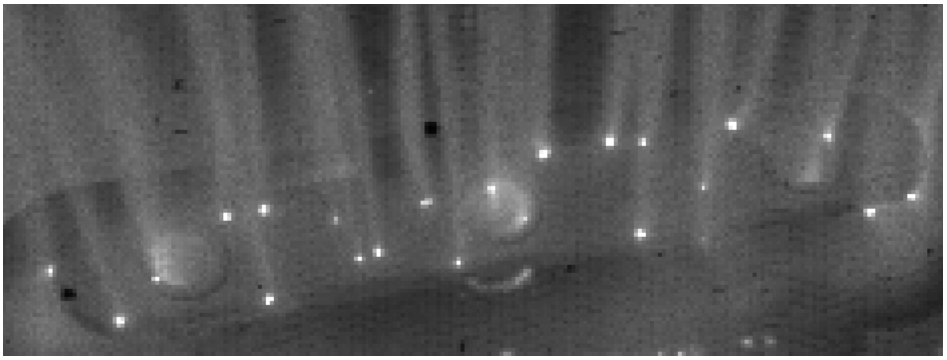

Figure 2.7: Cathode spots on a Pegasus injector.

Cathode spots are also called 'cold cathode emission'[37], 'arc spots',[35] 'explosive electron emission', [38] 'cathode flares', [39] and a variety of other names, and have been studied since the invention of the voltaic pile, remaining a topic of study today [40, 41, 42]. They occur at high-enough power to be independent of surrounding experimental conditions, and their properties depend primarily on cathode material. The initial breakdown event is thought to be triggered by joule heating via field emission from sharp surface projections ('whiskers') which exist, together with adsorbed impurities, in quantity on unconditioned surfaces. [43]

They are dense plasma centers appearing on the cathode of high-current discharges enabling essentially unlimited electron emission. Because of their small size, high energy densities, and mobile nature ($v_{spot} \sim 0.1 - 100\,\mathrm{m/s}$), some of their most basic properties, such as their size, are still uncertain, though current densities are estimated to be $\sim 10^8\,\mathrm{A/cm}^2$, and power densities $\sim 10^{13}$ W/m^3. Reported plasma densities range from $\sim 10^{26}$ m^{-3} to solid material densities of $\sim 10^{28}$ m^{-3} [44, 40]. Electron emission is believed to be accomplished through a combination of local thermionic and field ('thermo-field') emission. Typical voltage drops across cathode spots depend very weakly on current, and depend slightly on cathode material and surface condition, but in general fall within the interval $10 - 30$ volts. For both molybdenum and carbon for example, the value is approximately 30 V. [45]

For a given cathode surface material and impurity condition, cathode spots are known to emit current from a minimum stable current ($\sim 0.1 - 1\,\mathrm{A}$) up to a maximum current (∼100s of A) depending on cathode material. For Molybdenum this value is approximately 300 A. Current increases are effected by the eruption of new cathode spots.[40]

Examination of surfaces afterward reveals that a single moving spot is in fact a sequence of explosive events, (see Fig. 2.8) and that motion is accomplished by the sequential explosion of new protuberances near previous events. Typical crater sizes are $\sim 10\,\mu$m, and are larger for higher cathode temperatures and cleaner surfaces.[46] Reported electron temperatures T_e are in the range of a few eV [40]. Cathode spots are understood to produce plasma with high enough pressure as to render electrode processes largely independent of ambient plasma conditions, however external gas conditions influence spots indirectly, via adsorbed surface layers at the cathode and weakly through effects on the downstream plasma.[46] In many situations, cathode spots on well-conditioned surfaces can be regarded as having properties that are consistent across experiments.

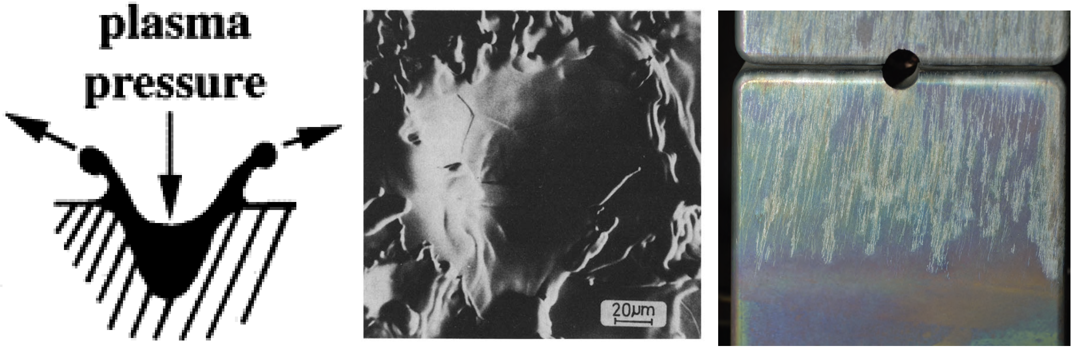

Figure 2.8: At left, a depiction of cathode spot erosion of a cathode surface, from [3]. Middle, from [4], a cathode spot crater in an arc track on a tungsten cathode. Right, from [5, 6, 7], cathode spot tracks on the upper divertor of ASDEX-U.

Cathode spots are known to erode cathode material from clean, conditioned surfaces in vacuum at a rate proportional to current. [3] Material erosion takes several forms, including vapor spray directed normal to the surface, and liquid and solid macroparticle droplets emitted at low angles to the surface. These droplets of bulk material can reach 0.1 mm, and tend to be larger for higher-temperature cathodes [47]. Erosion rates are given in kg/C. For Mo, for example, the rate is 0.5×10^{-7} kg/C, and for carbon, it is 0.2×10^{-7} kg/C [48, 49].

Cathode spots are divided into two types,[50] corresponding to different conditions of the cathode surface and different induced phenomenology. Type 1 spots occur on surfaces covered by oxide layers or adsorbed vapor. They move more quickly and produce relatively little surface ablation. Type 2 spots occur on clean metal surfaces, they require higher breakdown voltages to be initiated, are slower moving, and ablate more cathode material. Cathode spots' tendency to clean electrode surfaces under vacuum results in an eventual transition with use from Type 1 spot phenomenology to Type 2. Experiments show that this transition occurs after $\sim 10^2\,\mathrm{C/cm^2}$ of arcing in high vacuum. [46]

2.2.2 Unipolar Arcs

Cathode spots occur in fusion devices on plasma-facing conductors as the cathode emission regime of unipolar arcs [8, 51, 52, 53, 54, 34], where the tokamak plasma functions as the anode, and the applied voltage and return current are sustained by the plasma ion sheath. An example showing damage from spot tracks after unipolar arcing in ASDEX-U is shown in Fig. 2.8. Cathode spots are in this case a component of a larger circuit that includes inflowing electrons from the plasma onto the neighboring area of the spot. Hot electrons escape the plasma through the sheath, and return to the plasma via the spot. Because the sheath drop is reduced by the spot to its characteristic voltage drop, $\sim 30\,\mathrm{V}$, more electrons from the plasma can arrive at the neighboring surface once the spot is established, so the effect is self-sustaining. Because cathode spots possess a minimum sustaining current ($\gtrsim 1\,\mathrm{A}$), tiled inner walls used in tokamaks discourage unipolar arcing by presenting an area that is normally too small to draw an inflowing electron current above this threshold. [43]

The presence of unipolar arcs on limiters and divertors and their appearance during deconfining instabilities has been linked to the presence of open field lines, and their reduced ability to confine electrons. For open field lines, parallel electron diffusion to the wall occurs more quickly than for ions, and electrons are confined electrostatically with a positive plasma potential, as for a typical unmagnetized plasma. Large enough positive plasma potentials induce sheath breakdown and arc development. [43] Even after a tokamak's conditioning sequence, while stable quiescent plasmas can exist without arcing, periods of plasma growth, quench and disruptions can elicit unipolar arcing. Periods of vigorous MHD activity, and fast-electrons are also correlated with unipolar arcing. [8]

Unipolar arcs are observed on floating injector structures during LHI in Pegasus as well, where they can produce a more extensive breakdown, particularly if they interact with insulators.

2.2.3 Spot Motion

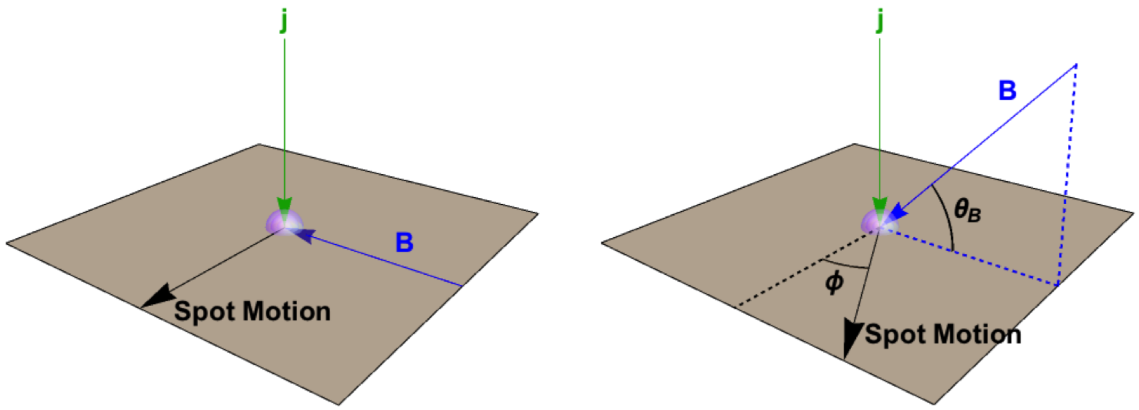

Figure 2.9: Spot motion for the case of magnetic field parallel to the cathode surface ($-\mathbf{j}\times\mathbf{B}$ only, left) and magnetic field at a general angle to the cathode surface ($-\mathbf{j}\times\mathbf{B}$ and acute angle rule, right).

A long-standing observation about cathode spots, first described by Johannes Stark in 1903, is their counter-intuitive motion across the cathode. The apparent motion occurs as a discrete series of new events on the cathode surface. In the absence of a magnetic field, new spots are created randomly, and the overall motion is similarly random. However, in magnetic fields parallel to the plane of the cathode, spots are observed to move in the $-\mathbf{j}\times\mathbf{B}$ direction, where spot current $\mathbf{j}$ is a normal pointing into the surface, and $\mathbf{B}$ is the external field. When the field possesses a general angle θ_B with respect to the cathode, retrograde motion is subject to a correction called the acute angle rule, which describes an additional drift at an angle ϕ, the 'Robson angle,' away from purely $-\mathbf{j} \times \mathbf{B}$ direction, toward the acute angle between the field and its projection onto the cathode surface [41]. The relevant geometry is illustrated in Fig. 2.9.

Like many other properties of cathode spots, there is no consensus on the cause of this motion, and many models exist for explaining its origins [55]. Moreover, while the $-\mathbf{j} \times \mathbf{B}$ tendency is a well-established experimental result, less data for the exact value of the Robson angle is available, and no experimental consensus for its exact measured value exists, particularly since it appears to also depend on surface conditions [56, 57]. Earlier investigations of cathode spot motion in the presence of an oblique magnetic field [58, 59, 56] approximated the Robson angle with a simple linear model $\phi \approx \varrho\theta_B$, with empirical constant $\frac{1}{2} \leq \varrho \leq 1$, and θ_B the angle between $\mathbf{B}$ and the cathode surface, but this model did not capture the saturation of ϕ observed at higher θ_B.

More recently, the Robson angle ϕ for acute angle motion has been approximated in [60] as

$$\phi \approx \arctan\left[\frac{R}{R+r}\sin\left(\theta_B\right)\right] \tag{2.19}$$

where the quantity R is the effective radius of a circulating return current of electrons from the plasma back to the cathode surface outside of the spot and r is the spot emission radius. These are depicted in Fig. 2.10 (a), where the arrows indicate electron flow. This conceptual framework, attributing the new spot creation during retrograde motion to bombardment by electron return current, is ultimately derived from observations of these currents in numerical simulations of spots in an external field [61].

According to the simplified model, the circulating return currents are regarded as many current loops surrounding the spot, each with some magnetic moment μ. In the absence of an external field, μ points in the azimuthal direction, and loops are equally distributed about the spot. When an external field is applied, they experience a torque $\tau = \mu \times \mathbf{B}$. This torque on the streamlines works to align them with the background magnetic field.

For the case of a purely retrograde motion in a magnetic field parallel to the cathode plane, $\tau = \mu \times \mathbf{B}$ is normal to the cathode plane, and stream lines are rotated azimuthally around the spot to 'bunch up' at the $-\mathbf{j}\times\mathbf{B}$ side where they are in alignment with applied $\mathbf{B}$, causing preferential bombardment in this direction. This preferential bombardment establishes the more probable location for a new spot and the observed global tendency. This is depicted in Fig. 2.10 (b), where unperturbed circulating electron currents prior to field application are depicted in black for comparison, and gray dashed lines indicate stream lines after being 'torqued' toward $-\mathbf{j} \times \mathbf{B}$ by the external field.

Figure 2.10 (c) shows how this model also leads to acute angle motion. When the field is at a general angle with respect to the cathode surface, the magnetic moment of the streamline 'loop' is assumed to additionally tilt the streamline so the moment aligns with the applied field. The azimuthal zone of 'bunching' leading to a preferentially bombarded region in direction $-\mathbf{j} \times \mathbf{B}$ is now is now additionally shifted $\approx R\sin(\theta_B)$ toward the acute angle of the field line at a radial distance $R + r$ from the center of the spot, prescribing the tangent of the acute angle deflection, and leading to the predicted angle of motion away from purely $-\mathbf{j} \times \mathbf{B}$ of $\phi \approx \arctan\left[\frac{R}{R+r}\sin(\theta_B)\right]$. Note that the elevation of the loop over the cathode surface affects both of these numbers, which should be considered idealized and approximate.

Good agreement with experimental data has been found with this model for small spots with $R \gg r$ and large spots with $R = r$. [62] The constants R and r will be absorbed hereafter in this work into a single constant $\varrho = R/(r + R)$ where $\frac{1}{2} \leq \varrho \leq 1$.

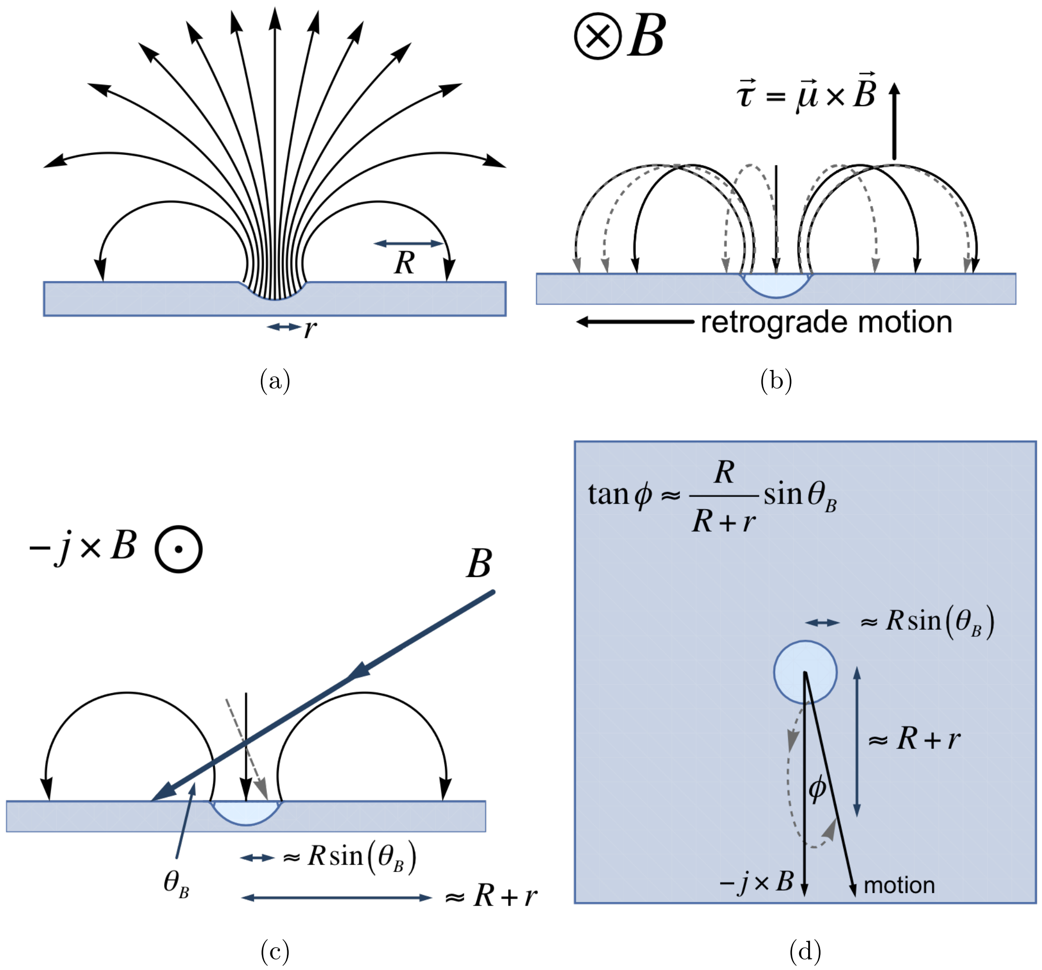

(a) (b)

(c) (d)

Figure 2.10: Electron streamlines from a cathode spot for various field configurations. a.) Streamlines emanating from spot without field. Spot radius r and circulating current radius R are indicated. b.) Purely retrograde motion. Only circulating currents are illustrated. For reference, unperturbed lines are shown in black. A torque vector which rotates stream lines is indicated. c.) Acute angle motion. Perturbed stream line in the direction of motion is shown as gray dashed line. d.) Top view of c.)

Finally, a tendency to drift in the direction of large external field gradients has been observed. All three of these rules are sometimes generalized as the so-called maximum principle, so-named because the cathode spot ultimately drifts in the direction of the total field gradient, where total field is taken as the sum of an external macroscopic field and the perturbing microscopic field of the cathode spot itself. [63]

2.2.4 Cathode Design Concept

Cathode spot emission is periodically induced by operation at high voltage. While spots cannot always be prevented, on the basis of the rules governing their motion, geometric design features can be added that prevent them from triggering more severe arcing or causing damage to injector structures. These design features impart motion that guides spots away from insulators that structurally support the cathode and insulate feedthroughs supplying current. The design also prevents cathode spot motion toward regions that can have line-of-sight to the anode, which can trigger more severe arcing.

A cathode design for use in a tokamak during LHI has been optimized with respect to the rules governing spot motion. A promising candidate geometry for confining cathode spots radially, which is consistent with the imposed magnetic field in tokamaks is the conical frustum. [64, 65] This geometry consists of a conical section in a coaxial background field (the toroidal field) to achieve radial confinement of spots. Radial confinement prevents migration of spots outward to insulator materials at the outer edge. A coaxial cross-section of the basic setup is pictured in Fig. 2.11. The acute angle between the coaxial field and the conical surface induces inward radial drift, while $-\mathbf{j} \times \mathbf{B}$ is in the azimuthal direction around the cathode. Thus at low-current density, introducing an arbitrary conical pitch angle is sufficient to achieve inward radial motion with the conical frustum.

However in LHI, the azimuthal stream self-field is large enough to significantly alter the total field. This new azimuthal $\mathbf{B}_\theta$ component, when crossed with $\mathbf{j_z}$, introduces a new outward radial drift, so that only a limited range of angles manifests net inward radial motion. Thus the precise form of the acute angle rule becomes important, as an optimization of the pitch angle for maximal inward radial flow in the operating conditions is required to retain inward motion.

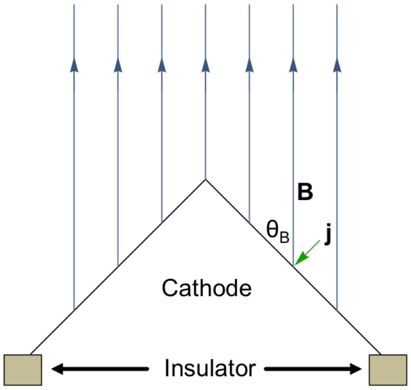

Figure 2.11: The conical cathode in a coaxial magnetic field **B**, and corresponding an acute angle θ_B. Cathode spot current **j** is indicated.

In order to design a cathode for use in a tokamak magnetic field, a choice of a model for acute angle motion was necessary. The model described earlier with

$$\phi = \arctan\left[\varrho \sin\left[\theta_B\right]\right] \tag{2.20}$$

was used, though both this form and the simple linear model from above generally agree with experiment at small ϕ with $\frac{1}{2} \leq \varrho \leq 1$. Because Eq. 2.20 captures non-linear $\phi < \varrho\theta$ behavior observed at large ϕ, it was used as a worst case design-point, however the final design has $\theta_B \sim 30$ degree, where nonlinearity is small and the models agree well.

For design purposes, the heuristic rules for motion must be reduced to a more useful form, which combines the two rules into a single flow field equation $\overrightarrow{r}'[\overrightarrow{r}]$, in terms of independent functions of cathode surface location $\overrightarrow{r}$, normalized total magnetic field $\widehat{b}$, and outward cathode surface unit normal $\hat{n}$:

$$\overrightarrow{r}' = \varrho\left(\hat{b} - \hat{n}\left(\hat{n}\cdot\hat{b}\right)\right)\hat{n}\cdot\hat{b} + \hat{n}\times\hat{b} \tag{2.21}$$

where $\overrightarrow{r}'[\overrightarrow{r}]$ is not a velocity, but a flow vector of arbitrary norm.

This can be seen to be equal to the heuristics given above by noting first that $\hat{n}\times\hat{b}$ is the $-\mathbf{j}\times\mathbf{B}$ direction, and $\hat{b} - \hat{n}\left(\hat{n}\cdot\hat{b}\right)$ is a projection of $\hat{b}$ into the cathode plane, which is perpendicular to $-\mathbf{j}\times\mathbf{B}$. These directions are parallel to the legs of the triangle in Fig.

2.10 (d). Thus if the ratio of the magnitudes of these two components is also $\frac{R}{R+r}\sin\theta_B$, a similar triangle is created with the same predicted motion direction. Using for the moment an angle θ_A between vectors $\hat{n}$ and $\hat{b}$:

$$\left\|\varrho\left(\hat{b}-\hat{n}\left(\hat{n}\cdot\hat{b}\right)\right)\hat{n}\cdot\hat{b}\right\| = \varrho\left\|\hat{b}-\hat{n}\left(\cos\theta_A\right)\right\|\cos\theta_A \tag{2.22}$$

$$\left\|\varrho\left(\hat{b}-\hat{n}\left(\hat{n}\cdot\hat{b}\right)\right)\hat{n}\cdot\hat{b}\right\| = \varrho\left(\sin\theta_A\right)\cos\theta_A \tag{2.23}$$

and

$$\left\|\hat{n}\times\hat{b}\right\| = \sin\theta_A \tag{2.24}$$

The ratio between the components is $\varrho\cos\theta_A$. The transformation back to θ_B is $\theta_A = \frac{\pi}{2}\pm\theta_B$ depending on whether $\hat{b}$ points into (+) or out of (-) the surface. Inserting this θ_A into $\varrho\cos\theta_A$ gives $\mp\varrho\sin\theta_B$, as expected, since $\varrho = R/(r+R)$. The alternating sign is a result of the acute angle remaining in the same direction when the magnetic field polarity (and $-\mathbf{j}\times\mathbf{B}$), change sign. Thus Eq. 2.21 gives the combined motion of a cathode spot that includes both retrograde and acute angle motion.

Using Eq. 2.21, a cathode surface may now be solved for, given a specific background field structure. In the case of LHI in Pegasus, the requirement is to prevent spots from traveling radially outward to damage insulators. The conical frustum geometry is a good candidate, since like the injectors it is cylindrically symmetric, and relies on a strong background field coaxial with the cathode, which already exists at the injector due to the toroidal field. Further, there is negligible field in the conical frustum's radial direction.

To obtain an optimal cathode shape, the radial motion predicted by Eq. 2.21 is differentiated with respect to available experimental knobs, which is here the conical pitch angle profile $\psi\left(\overrightarrow{r}\right)$ only, since background field is not flexible. First, normalizing Eq. 2.21 to get $\hat{r}'$ and dotting the result with an r-z surface tangent $\hat{t_r}$ gives the non-azimuthal component of motion. In cylindrical coordinates:

$$\hat{t_r} \cdot \hat{r}' = \{\cos\psi\left(r\right), 0, -\sin\psi\left(r\right)\} \cdot \hat{r}' \tag{2.25}$$

Assuming that the magnetic field has no component in the cathode's radial direction, i.e. $\hat{b} = \|b_\theta\|\,\hat{\theta} + \|b_z\|\,\hat{z}$, (Note b_θ and b_z are direction cosines of a normalized vector, and are not themselves normalized. They are also taken to be functions of radial position on the cathode, $\overrightarrow{r}$), Eq. 2.25 becomes:

$$\hat{t_r} \cdot \hat{r}' = -\frac{2b_\theta + \varrho b_z^2 \sin(2\psi(r))}{2\sqrt{-\left(b_z^2\cos^2(\psi(r)) - 1\right)\left(\varrho^2 b_z^2 \cos^2(\psi(r)) + 1\right)}} \tag{2.26}$$

This is the equation describing the non-azimuthal (r-z) component of motion of a cathode spot in the (normalized) field $\hat{b} = \|b_\theta\|\,\hat{\theta} + \|b_z\|\,\hat{z}$ on a cylindrically-symmetric cathode with a pitch angle $\psi\left(\overrightarrow{r}\right)$. Setting this expression to zero gives the threshold where radial motion is precisely zero, and motion is entirely azimuthal, i.e. rotation about the conical cathode without movement 'uphill' or 'downhill.'

Setting the derivative of radial motion equation, Eq. 2.26, with respect to conical pitch angle $\psi\left(r\right)$ to zero gives extremal (i.e. maximal and minimal) r,z motion as a function of cathode pitch angle $\psi\left(r\right)$: (Note that $\psi\left(r\right)$, like $\hat{b}$, is still allowed to change with radius.)

$$\partial_\psi\left(\hat{t_r} \cdot \hat{r}'\right) = 0 \tag{2.27}$$

For the case of a cathode spot in (normalized) field $\hat{b} = \|b_\theta\|\,\hat{\theta} + \|b_z\|\,\hat{z}$ on a cylindrically-symmetric cathode with a pitch angle $\psi\left(\overrightarrow{r}\right)$ described by equation Eq. 2.26, Eq. 2.27 becomes:

$$-\frac{b_z^2\left(\varrho b_\theta^2\cos^4(\psi)\left(\varrho^2 b_z^2 + 1\right) + b_\theta\sin(\psi)\cos(\psi)\left(\varrho^2 b_\theta^2 - \varrho^2 b_z^2\cos(2\psi) - 1\right) - \varrho\sin^4(\psi)\right)}{\left(\left(1 - b_z^2\cos^2(\psi)\right)\left(\varrho^2 b_z^2\cos^2(\psi) + 1\right)\right)^{3/2}} = 0 \tag{2.28}$$

This equation can be solved for $\psi\left(r\right)$. Its real roots $\psi^{+/-}\left(\overrightarrow{r}\right)$ give the pitch angle $\psi\left(r\right)$ profiles that maximize inward $\psi^{-}\left(r\right)$ and outward $\psi^{+}\left(r\right)$ motion:

$$\psi^{+}\left(\overrightarrow{r}\right) = \arctan\left[b_\theta\varrho\right] \tag{2.29}$$

$$\psi^{-}\left(\overrightarrow{r}\right) = \arctan\left[\frac{-b_\theta}{\sqrt{1-b_z^2}}\sqrt{\frac{1}{3\varrho^2}\left(Q^{1/3} - b_\theta^2\left(1+\varrho^2\right)\left(-6\varrho^2 + b_\theta^2\left(5\varrho^2-1\right)\right)Q^{-1/3} + b_\theta^2\left(1-2\varrho^2\right)\right)}\right] \tag{2.30}$$

$$Q = 2b_\theta^2\left(3\sqrt{3}b_z^2\varrho^3\sqrt{\left(1+\varrho^2\right)^3\left(4b_\theta^2 + \varrho^2\left(27 - 18b_\theta^2 - 5b_\theta^4 + 27b_z^4\varrho\right)\right)} + T\right) \tag{2.31}$$

$$T = \left(1+\varrho^2\right)^2\left(2b_\theta^4 + 2b_\theta^2\left(9-8b_\theta^2\right)\varrho^2 + 27b_z^4\varrho^4\right) \tag{2.32}$$

For special case $\varrho = 1$ consistent with observations in this work, $\psi^{-}\left(\overrightarrow{r}\right)$ reduces to:

$$\psi^{-}\left(\overrightarrow{r}\right) = \arctan\left[\frac{-b_\theta}{\sqrt{1-b_z^2}}\sqrt{\frac{1}{3}\left(-b_\theta^2 + Q_{\varrho=1}^{1/3} + 4b_\theta^2\left(3-2b_\theta^2\right)Q_{\varrho=1}^{-1/3}\right)}\right] \tag{2.33}$$

$$Q_{\varrho=1} = 2b_\theta^2\left(27 + 3\sqrt{3}b_z^2\sqrt{4+12b_z^2+11b_z^4} - 36b_\theta^2 + 13b_\theta^4\right) \tag{2.34}$$

for θ and z direction cosines of field unit vector $\hat{b} = \|b_\theta\|\,\hat{\theta} + \|b_z\|\,\hat{z}$. For nominal operating conditions in Pegasus, this results in gradual profiles in the 50° range with respect to the base plane of the conical frustum. For ease of construction this was simplified to a flat 55°, which represents a reasonable approximation to this curve for many plausible operating scenarios.

Indeed, a simple expression can be obtained for a constant pitch angle $\psi\left(\overrightarrow{r}\right) = \psi_0$, in a field $\overrightarrow{B}_{tot} = \frac{\mu_0 I_{TF}}{2\pi R_{inj}}\hat{z} + \frac{\mu_0 I_{inj}}{2\pi r}\hat{\theta}$ by plugging the corresponding normalized values for b_z and b_θ into Eq. 2.26 and setting this expression for non-azimuthal motion to zero, then solving for I_{inj}. This gives the maximum I_{inj} before outward radial motion at radius r_{max}, and clearly illustrates the relationship of field, conical frustum radius, injector location R_{inj}. After algebraic simplification, this reduces to:

$$I_{inj,max} = I_{TF}\frac{r_{max}}{R_{inj}}\sqrt{\frac{\sqrt{1+\varrho^2\sin^2\left(2\phi_0\right)}-1}{2}} \tag{2.35}$$

representing the maximum injected current that retains inward motion out to r_{max}. For typical conditions in Pegasus $I_{TF} = 288$ kA, $r_{max} = 1.6$ cm, $\psi_0 = 55°$, $R_{inj} = 0.7$ m, this value is between 1.5kA for $\varrho = \frac{1}{2}$ and 2.8kA for $\varrho = 1$. The geometric factor is most favorable at $\psi_0 = 45°$.

An injection scenario is indicated in Fig. 2.12 for $I_{inj} = 2$ kA, $R_{inj} = 0.7$ m, $B_{TF} = 0.08$ T, $\varrho = 1$. Expected cathode spot motion as a function of cathode pitch angle ψ and cathode radius r is shown. Eq. 2.26 is set to zero and plotted, providing the boundary between regions of inward (green) and outward (white) radial spot motion. Equation 2.33, indicating the optimal (most inward motion, or least outward motion) is also shown. A dashed line indicates the 55° profile that has been implemented. Vertical bars indicate inner and outer radii (0.8cm, 1.6cm) of the injectors used in Pegasus. No zone of inward motion exists at negative pitch angles.

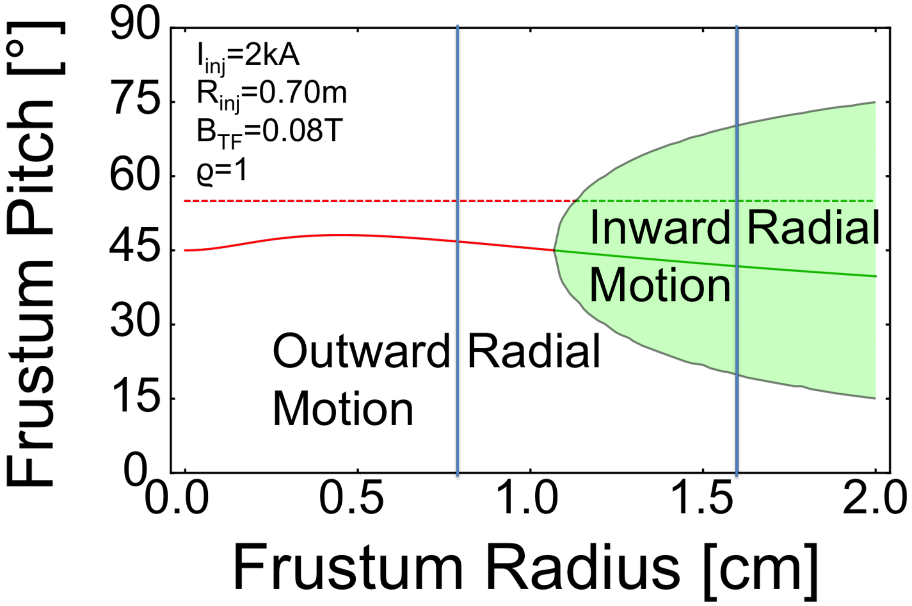

Figure 2.12: Radial spot motion regime vs conical frustum pitch angle and radial position on frustum for example operating scenario indicated in upper left. Green region indicates inward motion, uncolored region indicates outward radial motion. Vertical bars at 0.8cm and 1.6cm indicate minimum and maximum radii of most injector designs in Pegasus. Dashed line at 55° indicates machined part. Solid line indicates extremal profile.

Chapter 3

The Pegasus Experiment

3.1 Experiment Overview

The Pegasus Toroidal Experiment [11] is a university-scale spherical tokamak at UW Madison. There are several ongoing experimental research programs at Pegasus, including H-mode physics at low aspect ratio and non-solenoidal startup. Non-solenoidal LHI startup has been the principle thrust [66, 67, 68, 69, 70, 20], and has also supported Pegasus' achievement of high normalized current discharges [66], another research focus. Since non-solenoidal startup research is the aim of this particular work, discussions herein concentrate on the experimental capabilities at Pegasus that support this goal.

A CAD drawing of Pegasus is depicted in Fig. 3.1. Typical plasma parameters achieved in Pegasus are indicated in Table 3.1. Typical full-sized plasmas have major radius $R = 0.40$ m, minor radius $a = 0.35$ m, and aspect ratios $A \geq 1.1$. Very low aspect ratios are achieved due to the 5.5 cm radius centerstack, whose ohmic solenoid was constructed for Pegasus at the National High Magnetic Fields Laboratory [71]. Maximum toroidal field (TF) rod current is 288kA, providing 0.15T of field at the magnetic axis R_0, and present ohmic (OH) solenoid currents are 24kA, providing ~ 40 mV s of induction. There are 12 individual poloidal field (PF) coil packs, indicated in 3.1, which have been used in various grouped modules to give flexible control of poloidal fields.

Power is delivered to the coils with solid state hardware, and has been subject to significant technical development at Pegasus. Programmed coil currents are implemented with real-time feedback control via pulse-width-modulation (PWM) controller boards, and H-bridge configuration switching power supplies. The switches can be deployed in parallel to

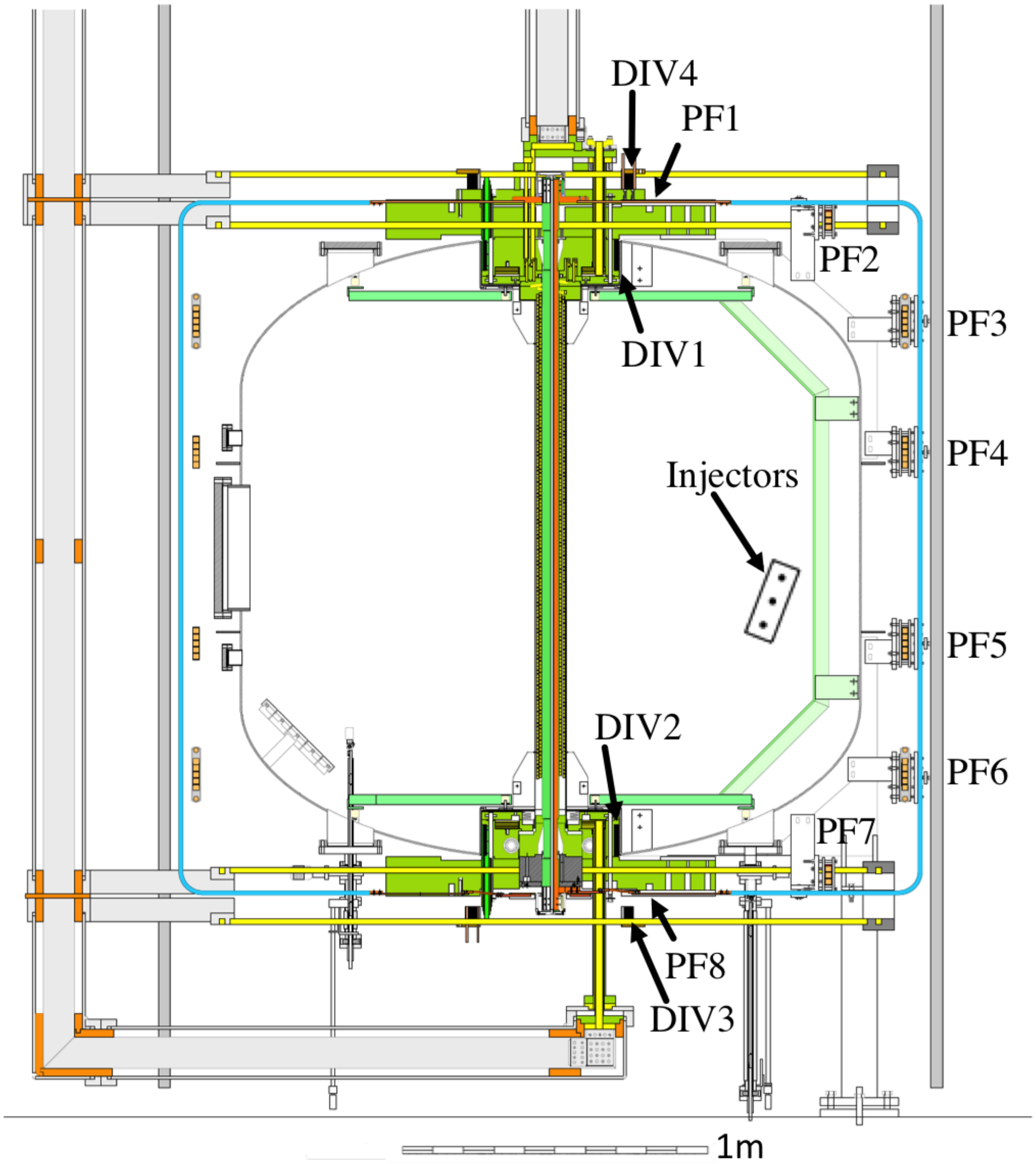

Figure 3.1: The Pegasus ST.

deliver coil currents of order 10 kA, including for example 24 kA regularly delivered to the TF coil set. The PF and TF coils are powered with 900 V banks controlled with IGBT (Insulated Gate Bipolar Transistor) switches, and the OH and current injection circuits are powered with 2700 V capacitor banks, controlled with IGCT (Integrated Gate-Commutated Thyristor) switches. The OH and midplane PF coils are controlled with parallel, 4 quadrant H-bridges, allowing currents of either polarity.

3.2 Plasma Cathode Electron Injectors

3.2.1 Background

Current injection for LHI experiments in Pegasus relies on specially-developed gas-injected arc-plasma cathode electron guns [70, 20, 67, 72]. These injectors, shown in Fig. 3.2, are adapted from previous designs employed at Madison Symmetric Torus [73, 74, 75], which were in turn based on an implementation at the Budker Institute of Nuclear Physics [76, 77, 78], where they were used as the plasma generator in high-perveance hydrogen ion sources. This design continues to be used at the Budker Institute as the emissive plasma source within the e-beam heating device at the GOL-3 multi-mirror facility [79], and for a number of other electron and ion beam applications developed there [80].

Table 3.1: Pegasus' Machine Parameters

Parameter	To Date
A	1.15 - 1.3
R(m)	0.2 - 0.45
$\mathrm{I_p}$(MA)	$\leq$ 0.22
$\mathrm{I_N}$(MA/m-T)	6 - 14
$\mathrm{l_i}$	0.2 - 0.5
κ	1.4 - 3.0
τ_{shot}(s)	$\leq$ 0.025
β_T(%)	$\leq$ 25

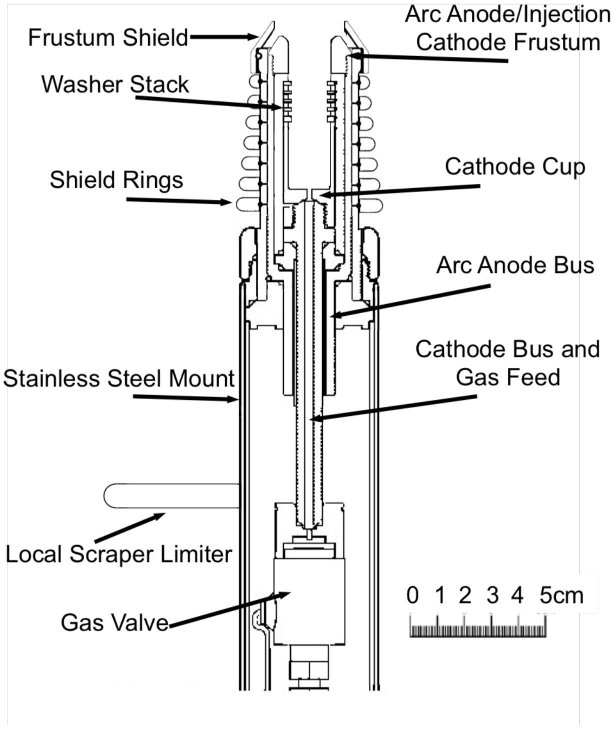

Figure 3.2: Schematic cross-section of the injector.

Figure 3.3 depicts the injector implementation conceptually. Injection is accomplished using a two-stage circuit topology, with the arc anode and injection cathode joined as a single electrode. The injection stage is comprised of the tokamak vacuum vessel as the anode, and the arc's anode as bias cathode. The arc stage generates a dense plasma cathode from which the injection circuit extracts an electron beam. The drift space of this beam is along the magnetic field lines of tokamak edge region.

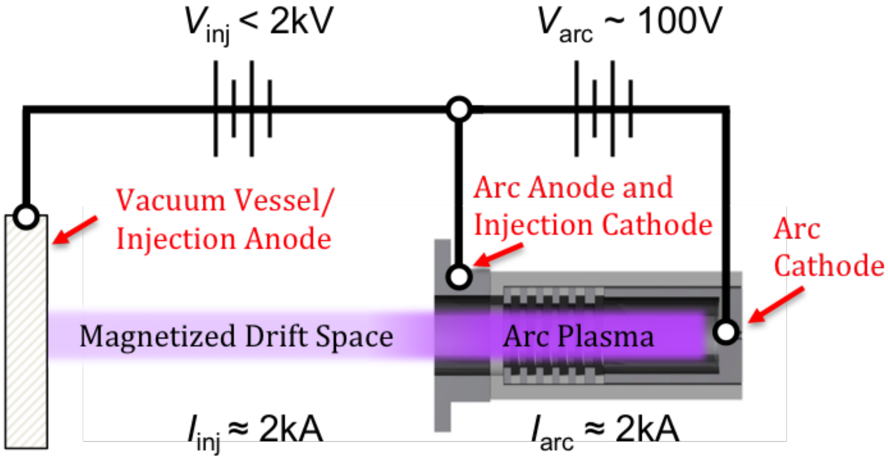

Figure 3.3: Diagram of injector circuit.

The electron-emitting discharge is a $> 1\,\mathrm{kA/cm^2}$ washer stack-stabilized, (also referred to as 'constricted' [29] or 'cascaded' [81]), low-to-medium pressure arc [82]. Each of the six washers has an inner radius of 0.64 cm, is constructed of molybdenum, and alternates with larger inner radii boron nitride spacer washers. The washer stack inhibits transition of the discharge to a vacuum arc, a transition which limits pulse length in diodes which do not include this feature. [29, 83]. The arc's anode is a 0.80 cm inner radius molybdenum annulus, and its cathode is a 0.80 cm inner radius, 2.26 cm deep molybdenum hollow cathode [84, 85] cup with gas injection. Recent improvements to the designs at Pegasus replace the solenoid valve used in the 3-injector array with a PV-10 piezo valve to provide better compatibility with the injectors' high-field environment.

The injectors used for this work are unique amongst electron beam devices in a number of important respects. They are not "grid-stabilized." Many devices use biased grid meshes and foils [86] to separate stages and establish the potential between stages. At least three stages are typical - a source, where particles originate, the acceleration gap where potential is applied, and the drift space where accelerated particles travel. However in the injectors used here, the emission surface between the arc discharge source and the acceleration gap is the open, or "foilless," [87] $2\,\mathrm{cm}^2$ aperture of the arc's hollow anode. There is also no anode foil, and no acceleration grids. This lifts energy deposition constraints imposed by these structures, and allows for significantly longer pulse-lengths than is typical for most electron sources, as well as higher current densities [29]. A potential is applied between the discharge anode and the remote vacuum vessel wall, resulting in an "acceleration gap" which is self-organized at the injector, and a beam whose drift space is within the magnetized interior of the toroidal vessel. The accelerating potentials are $\lesssim 2$ kV, limited by sheath breakdown via cathode spots on the arc anode electrode.

High current devices which operate in vacuum are limited in pulse length by "gap closure," where residual plasma expands into the acceleration gap, effectively shorting it out. However the injector used here is designed to operate immersed in plasma. This has two important effects. First, pulse length is not limited by gap closure or breakdown issues of architectures which rely on maintenance of vacuum because the acceleration gap is already "closed." The other important effect is due to the low impedance resulting from gap "closure." Use of the Child-Langmuir law to infer gap width from I-V characteristics indicates the gap is of order ~ 10 μm, which is several tens of λ_{De} in the arc discharge's residual plasma. Values of beam perveance, (i.e. $I/V^{3/2}$) for Pegasus injectors are $\sim 10^6$ larger than most other devices due to the comparatively very thin acceleration gap. This enables large beam intensities $J \sim 1$ kA/cm^2 at low voltages, ~ 100 V. Beam intensity is typically measured in units of Alfven currents I_A, or the current where beam magnetic energy per length normalized to kinetic energy per length exceeds unity [87]. Beams in this limit are referred to as 'plasma-like' beams [88] or 'hot' beams because their transverse kinetic energy is comparable to their streaming energy [89]. They are also magnetic self-interacting and often kink-unstable [90]. Injected current in Pegasus is typically several Alfven currents.

The specific point in parameter space occupied by the sources in Pegasus - low (< 1 kV) voltage, moderate ($\sim 1 - 10$ kA) current, extremely long (~ 10 ms) pulse length - is unusual, particularly for its long pulse duration. Most electron beams discussed in the beam literature operate for significantly shorter periods, due to the power deposition and vacuum limitations mentioned above. While literature examining similar "foilless," [91, 92, 93, 94] "pinched," [95, 96, 97, 98, 99, 100] "parapotential diodes," [101, 95, 102, 103, 100, 104] "plasma diodes," [105, 106, 107, 108, 109, 29] or "low energy high current electron beams (LEHCEBs)"

[110, 111, 112] exists and describes relevant physics, only a few examples are close matches to the present implementation [113, 74, 73, 75, 114, 115]. Beams with somewhat higher voltages ($\sim$ 10 kV) and currents ($\sim$ 10 kA) and much smaller pulse lengths ($\lesssim$ 1 us) are used in materials treatment applications [112]. Washer-stack arc guns with similar parameters are used without the addition of an injection circuit counterpart [115, 116]. Similar electron beams (low voltage, high plasma density, space charge-neutralized) exist as charge neutralizers/ionizers in electron beam ion traps/sources (EBIT/EBIS) devices, but at lower currents [117]. Intense beams exist in radiography source driver diodes, but at much higher voltages and currents, and much shorter pulse lengths [118].

3.2.2 Implementation on Pegasus

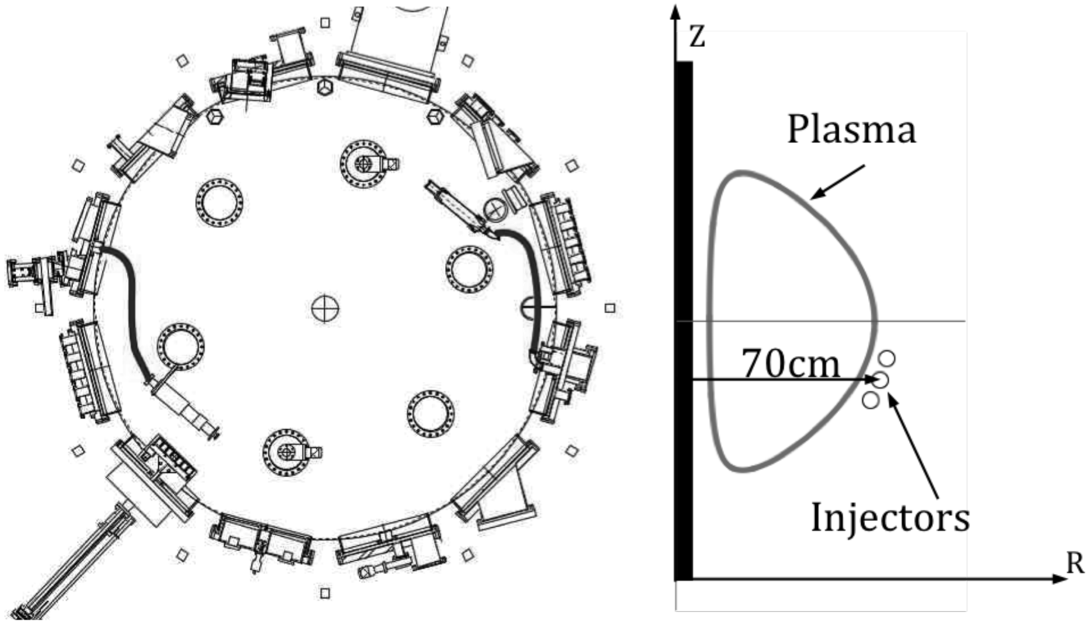

(a)

(b)

Figure 3.4: a.) Top down view of injector assembly locations. b.) Poloidal cross-section view of injectors

In Pegasus, three injectors are situated at the same toroidal location, on the tokamak's outboard side, at Z = { -13, -20, -27} cm with respect to midplane, and at a major radii R

= {67, 70, 73} cm. Another injector has more recently been installed at the diametrically opposite location, at R,Z = {70,-20} cm. See Fig. 3.4, which shows a top view of the injector arrays and their vacuum feedthroughs, as well as a toroidal section of the 3 injector array. The typical operating point of the arc is 2 kA, which burns in a cylindrical volume of radius 0.8 cm and length 5.6 cm, for periods of order $\sim 10\,\mathrm{ms}$. Typical example I_{arc}, V_{arc} traces are shown in Fig. 3.5. The operating point of the injection circuit is typically 1.5kA-2kA for a similar period. Examples traces are shown in Fig. 3.6.

A zoomed detail of the injection cathode is shown in Fig. 3.7. It has a radiused conical frustum shape for high-V_{inj} robustness to PMI effects discussed in the Theory and Results sections. A cathode shield and shield rings around the outer BN housing have been added for the same reason. Maximum injected currents of 5.6 kA, extracted from arc discharges with currents of 4 kA, have been obtained without significant material damage, parasitic arcing or other deleterious effects.

In typical operations, the injectors are immersed in the 0.08 T edge toroidal field, and at $I_{inj} = 1500$ A, the self-field of the beam is approximately half of this value. Thus, electrons are magnetized, ($\rho_e = 0.1$ mm at 10 eV) and working gas D^+ ions partially magnetized ($r_L^{D+} = 0.5$ cm, $\mathrm{r}_{\mathrm{injector}} = 0.8$ cm). Since characteristic lengths in the injector are of order $L \sim 1$ cm, and since impurity ion temperatures have been measured in similar devices [73, 115] to be $T_i \sim 10\,\mathrm{eV}$, they are expected to have low charge states, with $r_L^i > \mathrm{r}_{\mathrm{injector}}$, and to be unmagnetized within the arc channel. The arc is discharged for around 1 ms prior to the application of bias to the injection circuit in order to create a plasma-filled channel for extracted current to follow.

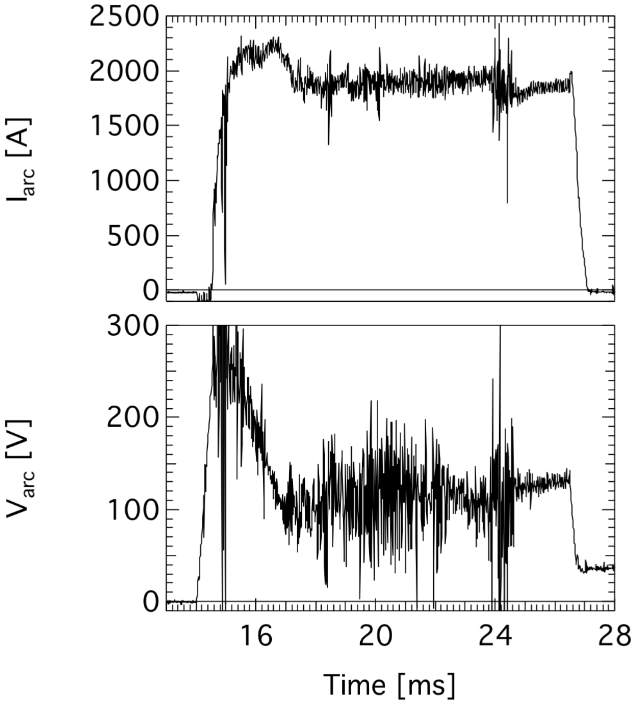

Figure 3.5: Example I_{arc}, V_{arc}

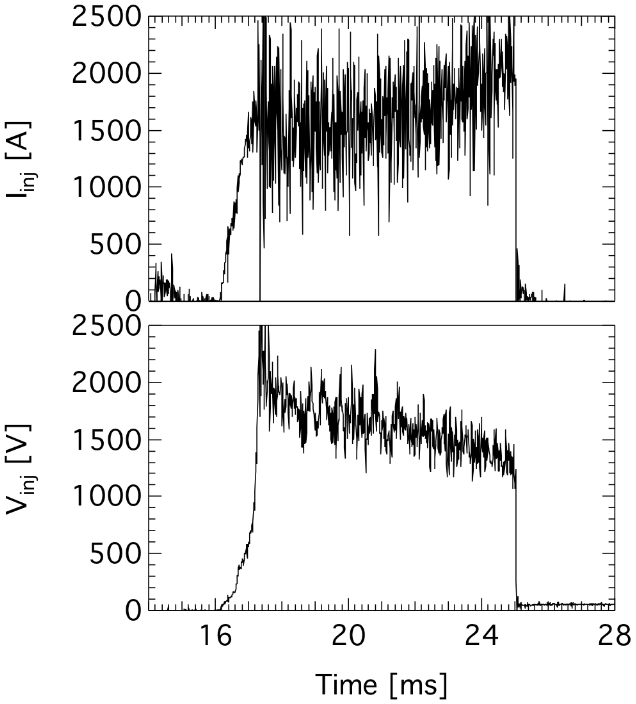

Figure 3.6: Example I_{inj}, V_{inj}

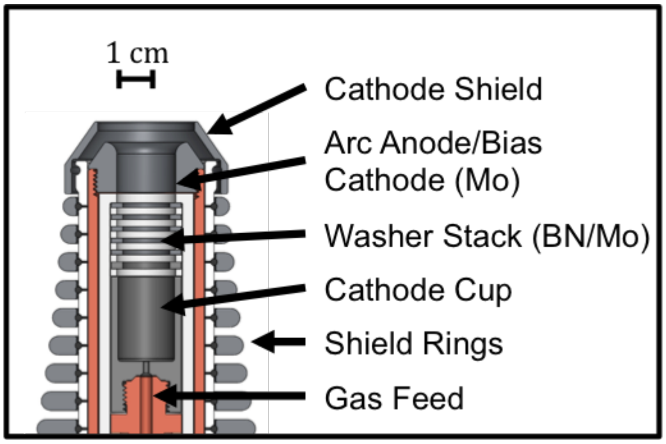

Figure 3.7: Schematic cross-section of internal injector components.

3.2.3 Injector Fueling Rate Calibration

Local fueling at the injector is accomplished with solenoid or PV-10 valves mounted behind the injector cathode cup. Calibration of the valves using a fast ion gauge was required to know the injectors' gas throughput and relate it to impedance. The fueling rate can be manipulated with the pressure behind the valve, or with voltage applied to the PV-10. Scans of pressure for the solenoid, and voltage for the PV-10, in vacuo were done to find the particle flux through the arc channel. An example calibration is shown in Fig. 3.8. Figure 3.8 (a) shows flow rate as a function of time measured with the fast ion gauge, obtained from the derivative of its measured signal $P\,(t)$. Figure 3.8 (b) shows flow rate at 27ms as a function of PV-10 voltage.

Flow rate, $\mathrm{d}N/\mathrm{d}t$, is calculated from the fast ion gauge signal $P(t)$ using the ideal gas law, $PV = NkT$, where P is pressure, V is volume, N is particle number, k is Boltzmann's constant, and T is temperature. Differentiating this law and applying it to the vacuum vessel where $V = 5300$ L, $T = 300$ K, the conversion is:

$$\frac{\mathrm{d}N}{\mathrm{d}t} = \frac{\mathrm{d}P}{\mathrm{d}t}\frac{V}{kT} \tag{3.1}$$

$$\frac{\mathrm{d}N}{\mathrm{d}t}\left[\frac{1}{\mathrm{s}}\right] = \frac{\mathrm{d}p_{tank}}{\mathrm{d}t}\left[\frac{\text{Torr -L}}{\mathrm{s}}\right]\frac{133\ \text{Pa}}{\text{Torr}}\frac{1\ \text{m}^3}{1000\ \text{L}}\frac{1}{k_B 300\ \text{K}}\frac{2\ \text{D}^+}{\text{D}_2} = \frac{\mathrm{d}p_{tank}}{\mathrm{d}t}\left[\frac{\text{Torr -L}}{\mathrm{s}}\right]6.5\times 10^{19}$$

where an additional factor of two in included since the fast ion gauge measures D_2 pressures and the key flow rate is that of D^+. Multiplying this result by the elementary charge casts this flow rate in terms of amperes, giving

$$I_{gas}\,[\mathrm{A}] = 11\frac{\mathrm{d}p_{tank}}{\mathrm{d}t}\left[\frac{\mathrm{Torr\ \text{-}L}}{\mathrm{s}}\right]$$

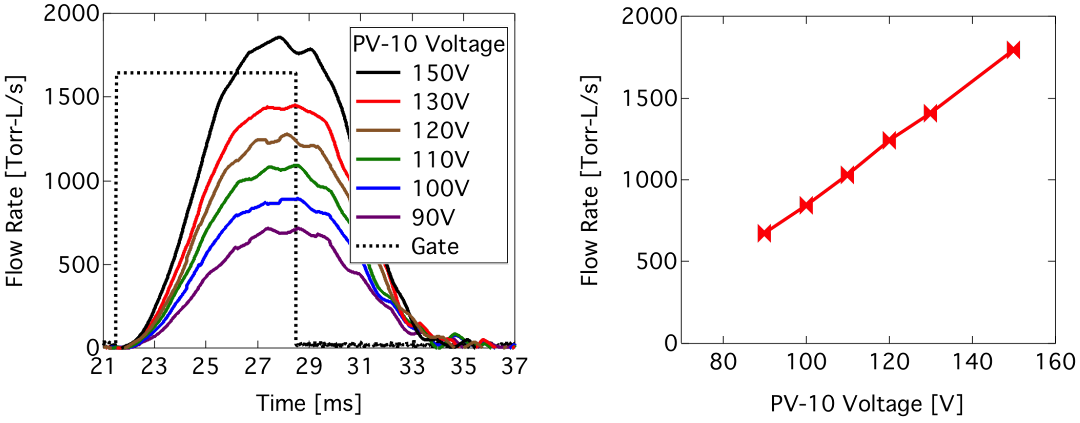

(a) (b)

Figure 3.8: PV-10 gas calibration. a.) Flow rate measured with a fast ion gauge as a function of time for a scan of applied voltage to the valve. Associated gate is shown as dashed line. b.) Flow rate at 27 ms as a function of applied voltage.

Fueling rate is very important to arc discharge parameters. In this work, fueling rate will be shown to control arc density, with subsequent effects on the injector impedance. Previous workers have found that injector fueling affects the maximum achievable arc current, with both linear and quadratic empirical relationships asserted [74, 119]. Impact of the fueling rate on arc properties and confinement will be discussed further in the next section.

3.2.4 Arc Physics

The physics of hollow cathode arcs and high-current arcs is poorly understood, though some literature exists to offer guidance as to what to expect of the physics of the arc plasma.

The hollow cathode arc is operated in a diffuse, low-to-medium (1-10s of Torr) pressure arc mode where it is reasonable to expect T_i approaching T_e [85, 84, 82, 120]. The arc is operated at a current density near to the onset of a so-called 'active anode arc' mode where significant anode erosion begins to occur via anode spots [82, 47, 120]. Empirically in Pegasus, which routinely runs at $I_{arc} = 2$ kA and $J_{arc} = 1$ kA/cm^2, significant anode erosion has been observed after operation at current densities $\gtrsim 2$ kA/cm^2. Very minor anode erosion is observed to occur at 1 kA/cm^2. At the anode in this regime of low-to-medium pressure (1-10 Torr), diffuse anode attachment, and high current densities (>1 kA/cm^2), it is likely that neutrals are fully-ionized in a region very close to the anode, and current is transferred to the anode by diffusion, with the anode potential drop actually repelling electrons. [82]

Because of the increased size of the arc cathode, current to the cathode is likely comprised primarily of ion current, fostering glow-type attachment to the cathode, resulting in improved cathode lifetime over previous designs. Unlike previous designs with significantly smaller cathode electrodes [73, 74, 75], post-mortem inspections of Pegasus models reveal little evidence of surface melt or 'slagging,' and are robust to thousands of pulses. While this type of attachment is atypical for discharges with ~ 1 kA/cm^2 current densities, it is not unexpected for the injector geometry in Pegasus, since ion saturation current to the 14 cm^2 surface area of the arc cathode for a 10^{21} m^{-3} plasma at $T_e \sim 10$ eV [73, 74, 75] is 5 kA - approximately the arc current. For smaller cathodes, not heated sufficiently to support thermionic emission, and configured to operate in a field emission regime, the only other mode of cathode attachment supporting similar current densities is cathode spots, an erosive attachment regime.

The typical picture invoked for the relation of the arc discharge to the injection circuit is one of electron current supporting I_{arc}, which is diverted to support I_{inj}. This picture is generally true for sources with much lower density [29]. However, large ion currents expected in the source used here are very likely to significantly impact its operation. Discharges in the pressure range observed in the injector can possess electric fields at the anode that repel electrons and draw ions [82]. Even if this is the case, the discrepancy in ion current drawn by the cathode vs. the anode is large enough to support I_{arc} through ion current alone. The surface area of the cathode is $14\,\mathrm{cm}^2$, and the surface area of the anode is $\sim 5\,\mathrm{cm}^2$ for most injector designs studied here. At $T_e = 10$ eV and a uniform $n_e = 10^{21}$ m^{-3}, the excess ion saturation current drawn to the cathode is thus $I_{ion} \approx 0.6 n_{arc} e v_{Bohm} \left(A_{cathode} - A_{anode}\right) = 2.5\,\mathrm{kA} \sim I_{arc}$ in the arc circuit bias direction. Density gradients in the arc plasma will contribute further to this discrepancy, and if the applied voltage of $V_{arc} \sim 130\,\mathrm{V}$ is concentrated at the cathode, secondary emission $\delta_{se}^{Mo} \approx 1$, will double available electron currents from the cathode. These effects in principle enable $I_{inj} > I_{arc}$, since the two currents are not directly coupled to each other - extracted electron current is derived from ionization and secondary electrons, which can be drawn out of the injector at a rate on the order of ion currents, and should therefore depend on arc density. The specifics of this process will depend on the specifics of ion and electron currents drawn by the anode.

The arc plasma is expected to be collisional. The collision frequency according to the Lorentz collision model is

$$\nu_{ei}\left(v\right) = \frac{5 \times 10^{-11} n_e Z_i}{T_e\left[\mathrm{eV}\right]^{3/2}} \frac{\ln \Lambda}{17} \approx 2 \times 10^9\ \mathrm{s}^{-1} \tag{3.2}$$

and the electron collision length is

$$\lambda_e \equiv \frac{v_e}{\nu_{ei}} = 1.2 \times 10^{16} \frac{T_e\left[\mathrm{eV}\right]^2}{n_e Z_i} \left(\frac{17}{\ln \Lambda}\right) \tag{3.3}$$

which at $T_e = 10$ eV and $n_e = 10^{21}$ m^{-3}, $\lambda_e = 1$ mm and $\lambda_i = \lambda_e \sqrt{\frac{m_e}{m_i}} = 20$ μm. Both of these quantities are smaller than the 1 cm radius of the arc channel.

The arc is expected to be fully ionized, and is likely opaque even to fast-moving ($\sim 3-4$ eV) Frank-Condon neutrals. The ionization mean free path of thermal D_2 is expected to be, using $< \sigma v_e >$ for a Maxwellian plasma at ~ 10 eV from [121, 122, pg. 27] and $n_e = 10^{21}$ m^{-3}:

$$\lambda_{iz,D_2} = \frac{v_{D_2}}{n_e < \sigma v_e >} \lesssim \frac{1 \times 10^3\ \mathrm{m/s}}{10^{21}\ \mathrm{m}^{-3} \cdot 5 \times 10^{-15} \mathrm{m}^3/\mathrm{s}} = 0.2\ \mathrm{mm} \tag{3.4}$$

and ionization mean free path of Frank-Condon neutrals within the arc is:

$$\lambda_{iz,F-C} = \frac{v_{n,F-C}}{n_e < \sigma v_e >} \lesssim \frac{2 \times 10^4\ \mathrm{m/s}}{10^{21}\ \mathrm{m}^{-3} \cdot 5 \times 10^{-15} \mathrm{m}^3/\mathrm{s}} = 4\ \mathrm{mm} \tag{3.5}$$

which is significantly smaller than the axial 5.5 cm length of the injector, suggesting gas injected into the cathode cup is ionized at least once, and the only surface from which gas can conceivably escape is that of the arc hollow anode.

Figure 3.8 shows that the typical D^+ flow rate $\frac{\mathrm{d}N}{\mathrm{d}t}$ or I_{gas} is $10^{22}\,\mathrm{s}^{-1}$ or ~ 10 kA, and a typical flux density is $10^{26}\,\mathrm{s}^{-1}\mathrm{cm}^{-2}$ (through $2\,\mathrm{cm}^2$). At this flux density, even if D^+ outflow from the arc region corresponds to kinetic energies of 10eV through the $2\,\mathrm{cm}^2$ aperture, the resulting density in the arc region is $10^{22}\ \mathrm{m}^{-3}$. However, the large potential step at the injector aperture when the injection voltage is applied presumably eliminates this convective loss term, particularly since the calculations above indicate all injected neutrals are ionized. This raises the question of how particle balance in the arc during injection works.

One possibility is deposition within the plasma-facing materials in the arc chamber. If one assumes a single D^+ particle deposited at each lattice site of the $\sim 10^{28}\ \mathrm{m}^{-3}$ electrode material over $\sim 10\,\mathrm{cm}^2$ of exposed internal electrode area, approximately 1 μm of depth is needed to deposit 10 ms of injected gas.

Another possible source of particle losses is resonant charge exchange in the arc anode region. Arcs in the medium and low pressure regimes (order 10 Torr) possess significant ion inflow to the anode, and commonly have a negative potential drop at the anode [82]. Because the charge exchange cross-section is quite large in this energy range, $\sigma_{cx} = 3 \times 10^{-19}\ \mathrm{m}^2$. Assuming the process occurs due to ions impinging on stationary neutrals, a charge exchange rate coefficient at 10 eV can be obtained: $v_i \sigma_{cx} = 1 \times 10^{-14}\ \mathrm{m}^3\mathrm{s}^{-1}$. This is comparable to the ionization rate coefficient of $< v_i \sigma_{cx} >= 5 \times 10^{-15}\ \mathrm{m}^3/\mathrm{s}$. This indicates a good fraction of the ions emerging from the anode can be expected to undergo charge exchange instead of ionization. After charge exchange, many fast neutrals can exit the arc chamber without, of course, being affected by the potential drop:

$$\lambda_{iz,D,cx} = \frac{v_{D,cx}}{n_e < \sigma v_e >} \lesssim \frac{3 \times 10^4\ \mathrm{m/s}}{10^{21}\ \mathrm{m}^{-3} \cdot 5 \times 10^{-15}\ \mathrm{m}^3/\mathrm{s}} = 6\ \mathrm{mm} \tag{3.6}$$

Moreover, it is likely that the density in the anode region is lower than the nominal figure $10^{21}\ \mathrm{m}^{-3}$ used here, which is based on coaxial line-of-sight measurements down the length of the injector that will be presented later. While the ratio of charge exchange to ionization does not depend on density, the distance fast neutrals subsequently travel without ionization increases with decreased density. Charge exchange is thus also possibly an important loss term maintaining overall particle balance in spite of the electrostatic confinement expected from a potential layer at the gun aperture.

3.2.5 Injector Power Supplies

Power delivery to the injector and arc circuits has been upgraded from a PFN-based configuration to one based on modular, solid-state, switching power supplies. A schematic is shown in Fig. 3.9. Preprogrammed currents are implemented with real-time feedback control via pulse-width-modulation (PWM) controller boards, regulating switching bridges at several kHz. Bridges can be deployed in parallel to deliver up to 14kA to the injection circuit.

Arc circuits for the injector array are regulated by parallel H-bridges comprised of insulated gate bipolar transistor (IGBT) switches. PWM feedback control off of the combined arc current is used to regulate the switches, though each arcs has been wired 1-to-1 with an H-bridge. This allows a single PWM to control several arc circuits. H-bridges assigned to the arc distribute current from a 450V, 420mF capacitor bank. Each arc circuit is wired in series with a ballast resistor and inductor to enforce current sharing between arcs when configured in parallel. A capacitor is installed in parallel with each arc to smooth/shunt switching transients, and to reduce electrostatic noise. A sparker circuit has been installed to initiate arc breakdown in conditions of reduced gas injection. Current is measured with a shunt resistance measured through an isolation amplifier, and with a Rogowski coil. Arc voltage is measured with a voltage divider measured through an isolation amplifier.

The injection circuit is driven using three parallel, single-quad bridges with integrated gate-commutated thyristor (IGCT) switches regulating current from a 2.7kV, 70mF capacitor bank. Each injector is driven in series with an inductor and ballast resistor. These components allow tuning for differences in impedance that can exist between the injectors, ensuring current-sharing during the discharge, and preventing surge currents to an injector that suffers arcing. A SCR crowbar has been added to terminate the injection period prior to the end of the arc phase, to prevent currents from being extracted after the arc plasma has been extinguished. As with the arc circuit, current is measured with a Rogowski coil and a shunt resistance behind an isolation amplifier, and voltage is also measured with a voltage divider/isolation amplifier.

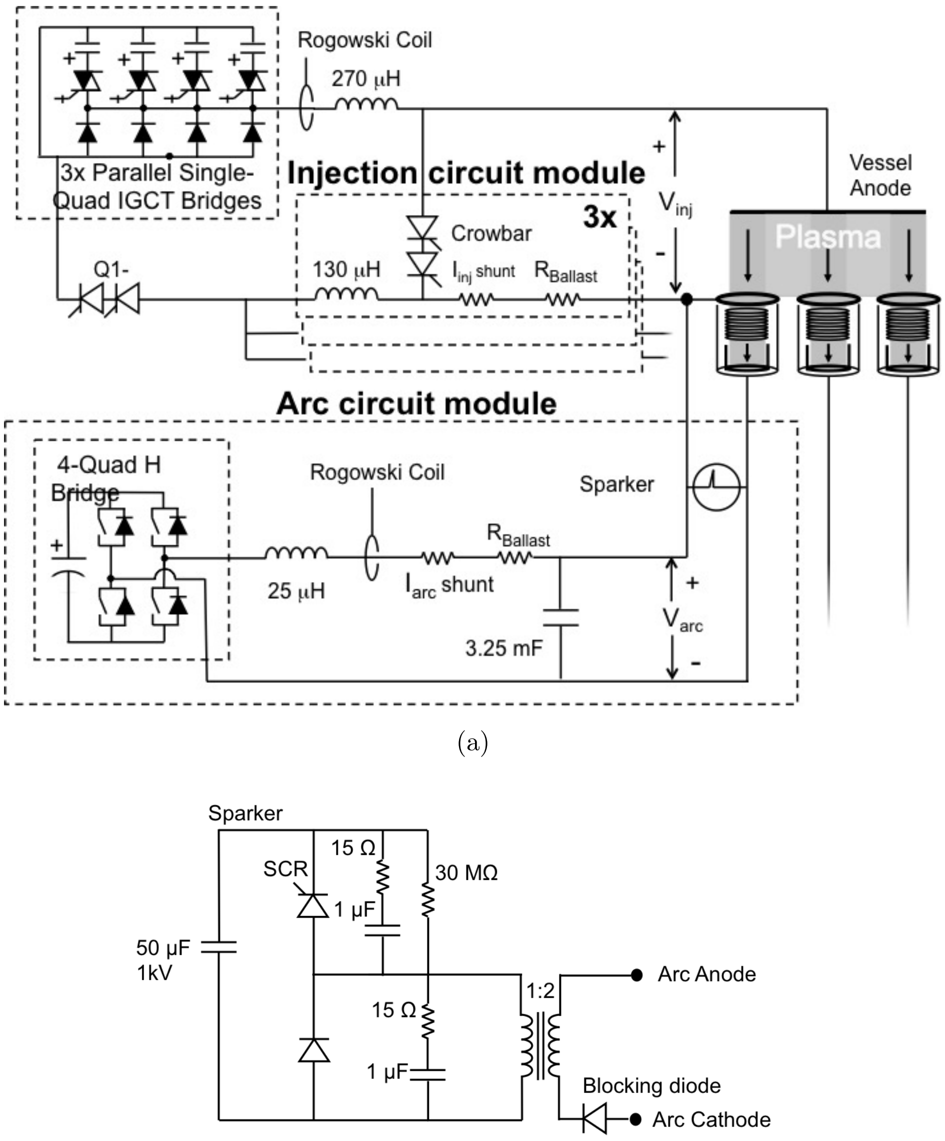

(a)

(b)

Figure 3.9: a.) Power supplies for arc and injection circuits. b.) Detail of sparker configuration.

3.3 Poloidal Probe Array

A subset of the poloidal magnetic probe arrays available on Pegasus was used for inferring the existence of coherent streams launched by the injector. These diagnostics along with other magnetic probes are documented in detail in [123]. The locations of the probes used in this work are reproduced in Table 3.2. The toroidal location of all outboard $\dot{B}_z$ probes was behind the half-pipe limiter (the locations are depicted in Fig. 3.10) at nominal toroidal angle of 357 degrees toroidally with respect to the customary coordinates system used in Pegasus that defines the limiter at 0 degrees. The apertures of the 3-injector set are 50 degrees 'downstream' of the PDX midplane probe array, and the aperture of injector 4 is located 230 degrees in this direction from the limiter. Figure 3.10 depicts this geometry.

Magnetic probe signals are often integrated to obtain B_z. However, because the presumed signal source is the injected current, this was not done for the model described later in Chapter 5. Because the injected current is relatively small in comparison to the plasma current I_p, its B_z is also correspondingly small. However, the raw signal $\dot{B}_z$ for rapid motion can dominated by the oscillatory stream. Therefore integrating the data filters out the signal of interest. Furthermore, integration introduces integrator drift and essentially adds additional error to the signal. The model used for comparison with the data was therefore developed to deal strictly with $\dot{B}_z$. Signals were bandpass filtered in a 20kHz window around the signal frequency of interest.

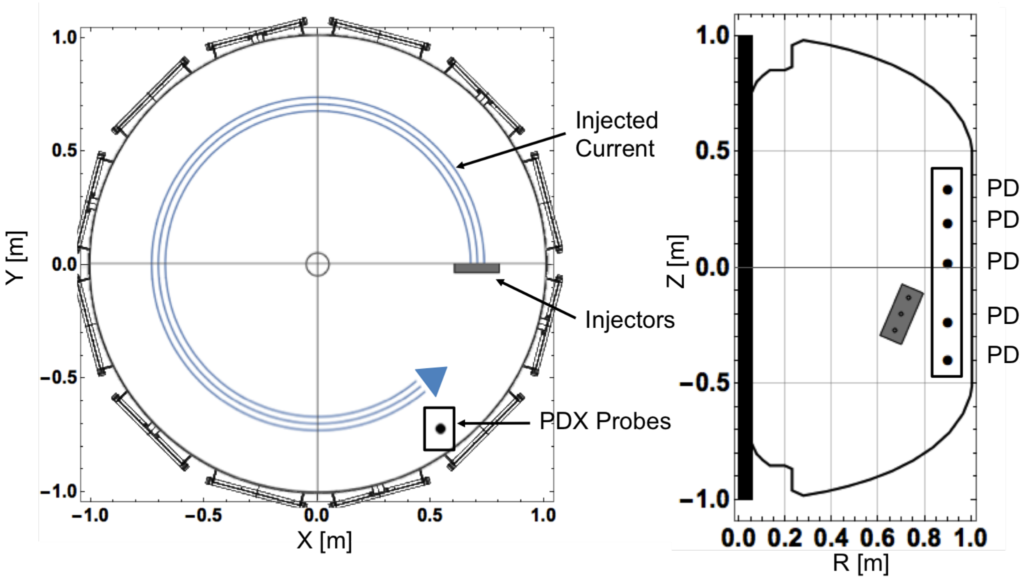

Figure 3.10: Outboard midplane region $\dot{B}_z$ probes. Blue boxes indicate locations. Precise locations are in Table 3.2.

Table 3.2: Outboard $\dot{B}_z$ probe array locations

Probe Symbol	R,Z [m]
PDX05	$\{0.902, 0.339\}$
PDX06	$\{0.902, 0.193\}$
PDX07	$\{0.902, 0.0221\}$
PDX08	$\{0.902, -0.233\}$
PDX09	$\{0.902, -0.394\}$

3.4 Fast Cameras

For fast imaging of plasma dynamics, Pegasus relies on a Vision Research Phantom v12.0 camera. This high-definition camera uses a 1280 x 800 CMOS sensor with a bit depth of 12 bits. Frame rates and resolutions are 6.242 kfps at the full 1280 x 800 resolution, up to 1 Mfps at resolution of 128 x 8. Fast cameras provide a crucial visual overview of plasma dynamics. Cameras have been used to roughly identify the point when relaxation occurs, as well as to identify unintended, deleterious plasma-materials interactions.

3.5 SPRED Spectrometer

An uncalibrated VUV spectrometer, [124] used in this work for obtaining radiation in the 10-110 nm window, was used to measure relative intensities of impurity lines. Because it is uncalibrated, it functioned as a qualitative impurity diagnostic, with a temporal resolution of 200μs.

3.6 Spectroscopic Balmer Line Broadening Measurements

Collisional, or Stark broadening, which occurs due to the electric fields of nearby perturbing ions, is strong for hydrogen species due to their characteristic linear Stark shifts. For a hydrogen atom in the presence of ions, the Stark effect symmetrically perturbs degenerate energy levels as $\Delta\nu \propto E$. The resulting emission line shape is a Lorentzian with a full width half max (FWHM) that scales with density as $n_e^{2/3}$, and thus can be used as a density diagnostic.

The optical train used for data taking is shown in Fig. 3.11 (a). It shows the line of sight in vacuum, the right angle prism used at the port 6 window to couple the line of sight to the fiber optic, and the spectrometer. Figure 3.11 (b) is a photo taken after alignment of the fiber, using a laser at the spectrometer to confirm that the internal arc region was within the fiber's field of view.

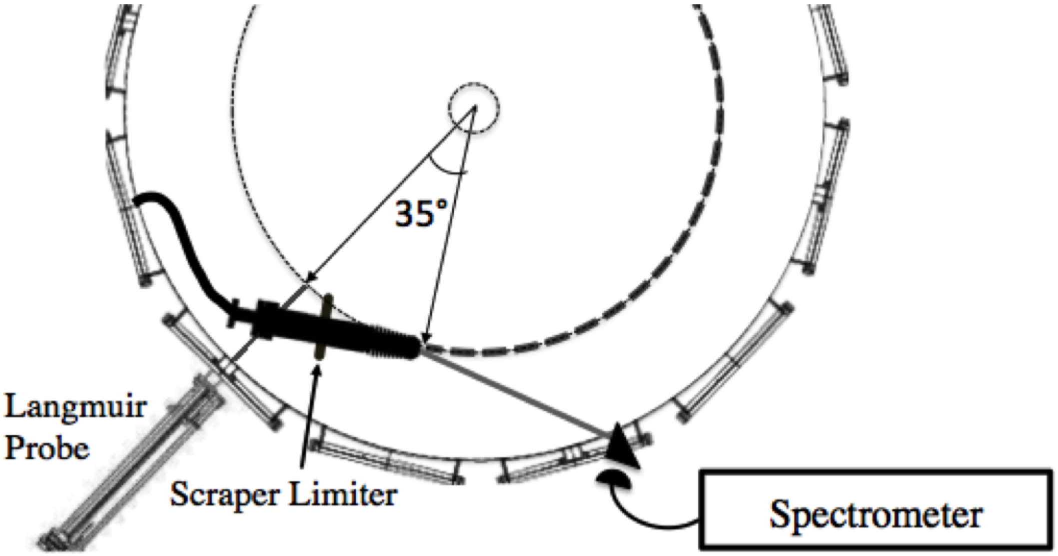

(a)

(b)

Figure 3.11: a.) Spectroscopic signal train and Langmuir probe position b.) Injector arc channel illuminated with calibration laser.

Collisional broadening measurements of Balmer lines were used to determine injector arc plasma density n_{arc} in the injector. Spectra were obtained with a specially-installed view into the injector through a port window. The measurements were recorded using a 1m Czerny-Turner polychromator and intensified high-speed CMOS detector.

Higher order Balmer series lines (δ, γ) than H-β were chosen because the Stark effect and associated broadening is larger for higher-order lines. The usual trade-off for higher-order Balmer series lines is lower signal, however the arc discharge was very bright, and signal intensity was not a problem. An example H-δ line profile for $n_{arc} = 8.6 \times 10^{21}$ m^{-3} is shown in Fig. 3.12.

The formula used for calculating density from H-δ line broadening was [125]

$$\lambda_{FWHM}^{H-\delta}[\text{nm}] = 0.092 \left(n_{arc} \left[10^{20}\ \text{m}^{-3}\right]\right)^{2/3} \tag{3.7}$$

and for H-γ [126]:

$$\lambda_{FWHM}^{H-\gamma}[\text{nm}] = 0.060 \left(n_{arc} \left[10^{20}\ \text{m}^{-3}\right]\right)^{2/3} \tag{3.8}$$

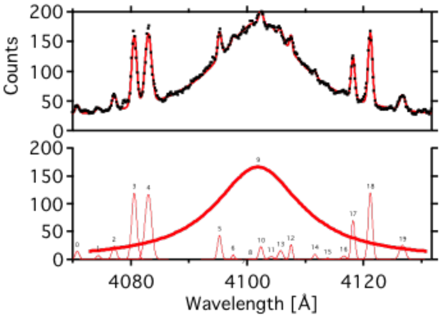

Figure 3.12: Representative H-δ line broadening measurement. Top: Data, Lorentzian fit to H-δ line, and Maxwellian fit to impurity lines. Bottom: Fits only, Lorentzian in bold.

3.7 Triple Langmuir Probe

A triple Langmuir probe was used for the n_{edge} measurement in this work, in ohmic discharges where current from injector 4 was drawn into the edge of a pre-formed plasma driven with the ohmic solenoid. It was inserted to the R, Z (0.7m, -0.20m) location of injector 4, upstream 35 degrees toroidally, and thus behind the scraper limiter mounted to the injector assembly. This placement was chosen so that measured edge conditions were as similar as possible to that of the injected stream.

Placement of the probe upstream of the injected current, and behind the injector's scraper limiter was a precautionary measure intended to ensure that the injected beam did not interact with the probe. Historically, probe electronics have been damaged by common mode voltages of order V_{inj} when the probe is used during LHI startup. In addition to potential hardware damage, beam impact could produce inaccurate measurements, since probe theory assumes maxwellian particle distributions. For this reason the Langmuir probe measurements during injection were taken exclusively in the edge of these established ohmic discharges ($I_p \sim 50 - 80\,\mathrm{kA}$), which supplied sufficient vertical field to direct any beaming particles along a field line not connected to the probe tips. Figure 3.13 shows a fast camera image taken with a fisheye lens during injection into an ohmic discharge, which showing this injected stream, and Fig. 3.11 shows a schematic illustrating the relative locations of the probe and injector 4. Representative triple Langmuir probe n_{edge}, T_e, V_{float} traces during injection are shown in 3.14, where the period during injection, 26ms - 28ms, is highlighted.

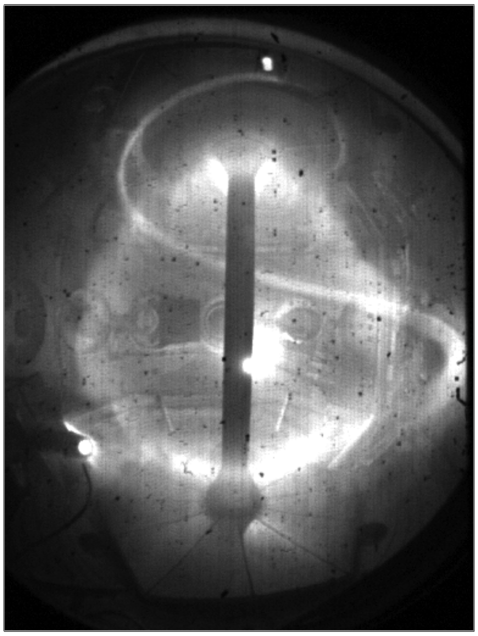

Figure 3.13: Fast camera frame taken with 'fisheye' lens during injection into edge plasma of ohmic-driven discharge, showing injected stream.

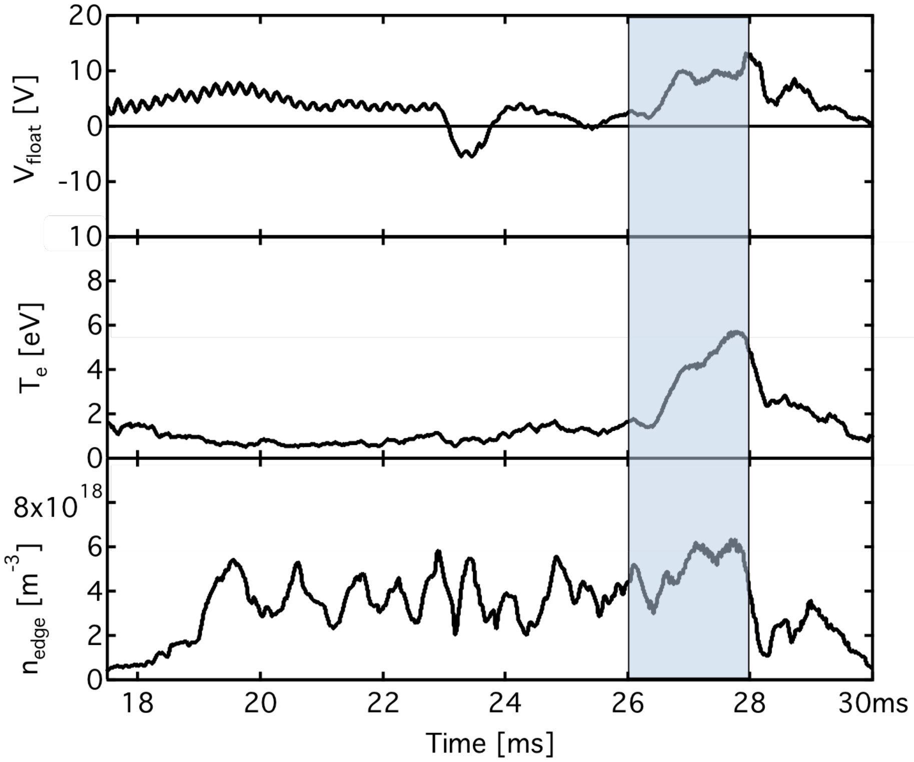

Figure 3.14: Example Langmuir Probe n_{edge}, T_e, V_{float} measurement during injection into an ohmic target discharge.

Chapter 4

Results

This chapter contains results of research into the physics setting the injector impedance. Section 1 describes cathode spot breakdown of the injector cathode. This breakdown is the practical limit to obtaining high values of V_{inj}. Typical phenomenology is described, followed by the results from an injector design to mitigate resulting damage by directing spot motion away from insulators. An initial analysis of breakdown on rings and a conical frustum shield, the newest additions to the injector which have significantly increased achievable V_{inj}, is presented in the Appendix.

Section 2 describes experimental tests of the impedance model introduced in Section 2.1, which sets V_{inj} up to the breakdown limit. The measured relationship between the injector arc fueling rate and the impedance figure of merit $I_{inj}/\sqrt{V_{inj}}$, associated with uniform profile beam density $n_b \equiv I_{inj}/\left(e\sqrt{2eV_{inj}/m_e}A_{inj}\right)$, is described. Then, results from an experiment involving injection into a set of ohmic discharges are presented, in which n_b, n_{arc} and n_{edge} were measured simultaneously during scans of n_{arc} and n_{edge}.

The impedance model pertains to the physics relating injector impedance to remote and local plasma densities. Section 3 discusses experimental control points for programming the injector impedance using this model. Data is shown elucidating the impact on the injector impedance of I_{arc}, fueling rate, injector arc anode length, and background magnetic field.

4.1 Injector Breakdown

4.1.1 Cathode Spots During LHI Discharges

Cathode spot breakdown on the injector can be triggered by very high V_{inj}. When this occurs, it reduces V_{inj} and the effective area of injection, A_{inj}. Both of these effects reduce helicity input, with the expected negative consequences for the discharge. The typical loss of voltage resulting from cathode spots is shown in Fig. 4.1, which contains voltage traces during two identically-programmed discharges, one of which is affected by cathode spots. It is typical for the occurrence of cathode spots to negatively impact the total achieved LHI plasma current, as shown in Fig. 4.2, which depicts the I_p traces for the discharges corresponding to the voltage traces in Fig. 4.1.

Cathode spots are known to cause erosion of adjacent materials, releasing impurities into the discharge. A representative SPRED spectrum showing this production is shown in Fig. 4.3, where two otherwise identical discharges are compared. The proliferation of lines corresponds to nitrogen from the boron nitride insulator, and the apparent continuum at high frequencies is likely due to very densely-packed nitrogen lines.

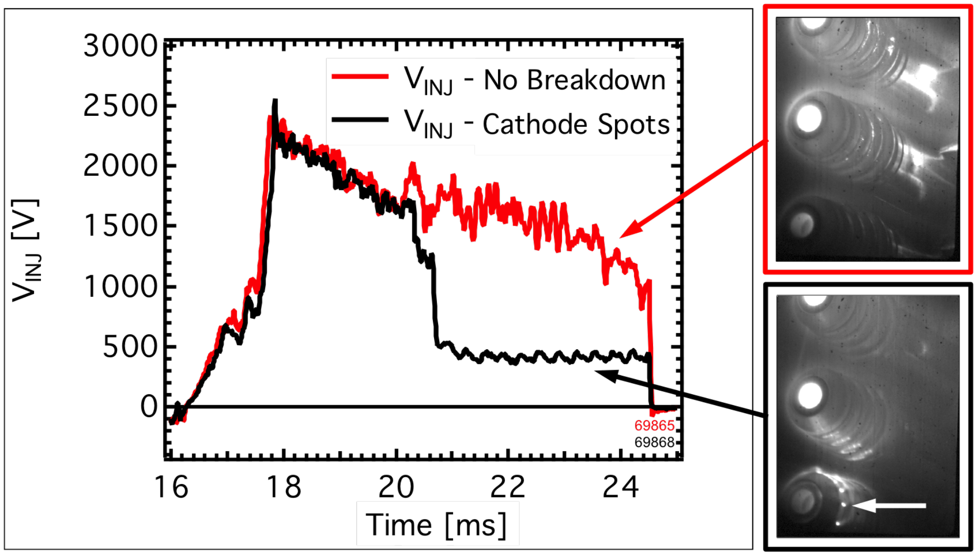

Figure 4.1: Left: Two voltage traces of similar discharges showing cathode spot-induced voltage loss. Right: Corresponding fast camera images for the two voltage traces at left. Top is case without breakdown, bottom image taken from after breakdown on bottom injector. Cathode spots on the bottom injector are indicated with an arrow.

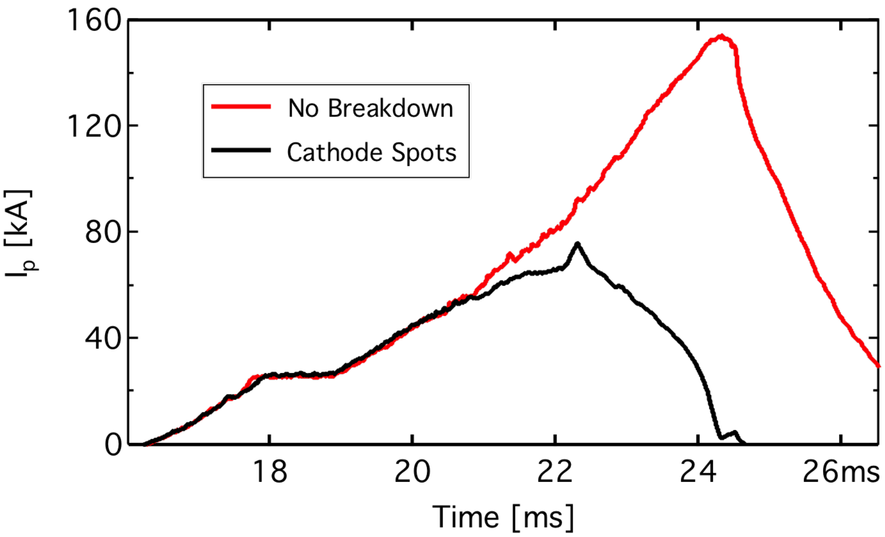

Figure 4.2: Comparison of resulting plasma current I_p for the cases with and without injector breakdown via cathode spots shown in Fig. 4.1.

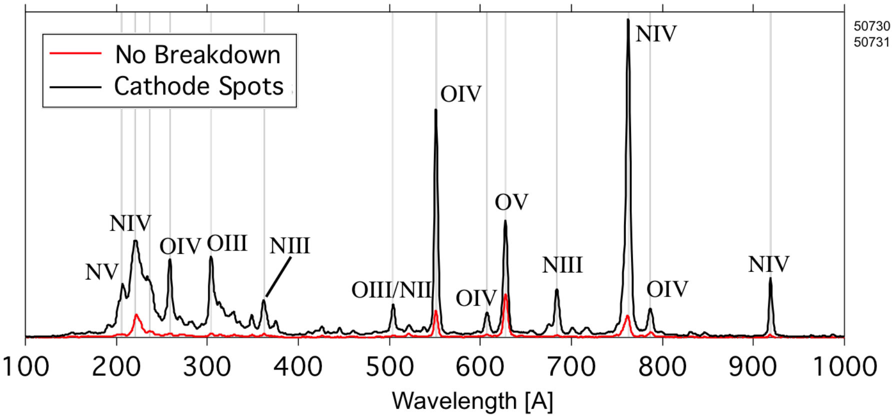

Figure 4.3: SPRED spectrum for two similar shots, one with cathode spots, and one without.

4.1.2 Cathode Spot Control

As a result of the work described in the theory section, the previous concave design of the injection cathode was updated to one with a convex geometry. The expectation from a convex geometry, which was machined with a conical pitch of 55° with respect to the base plane, is that cathode spots will move inward radially, away from sensitive insulating components. Typical fast camera images of the concave (-45°) design suffering spot-induced damage, together with a convex +55° design directing spots inward radially, are shown.

In the camera images of the concave design, shown in Fig. 4.4, cathode spots can be seen migrating to the insulator at the perimeter of the cathode, where they lock to it and interact with the insulator. An additional frame several milliseconds into this process is included at the end of the frame sequence, where ejecta can be seen being emitted.

Figure 4.5 shows the regions of inward motion expected from the sign of Eq. 2.26 on a cathode when $I_{inj} = 1500$ A, in a background toroidal field $B_z = 0.08$ T, for cases $\varrho = 1/2$ in Fig. 4.5(a) and $\varrho = 1$ in Fig. 4.5(b). Only the radial interval corresponding to actual constructed dimension is shown. Zones of inward motion are shaded. Regions of outward motion are unshaded. Constant 55 degree angle is shown as solid contour. Figure 4.5(a) shows that no inward radial motion is expected if $\varrho = 1/2$. Figure 4.5(b) shows that inward radial motion is expected for $\varrho = 1$ for most of the cathode's surface. The experimental conditions modeled here are the conditions for camera data shown in Fig. 4.6. Figure 4.6 shows that inward radial motion is obtained with the optimized cathode design, very similar to the predictions in Fig. 4.5(b), where $\varrho = 1$.

The design concept developed in the theory section has proven sufficient for spot control. While this addition does not prevent cathode spots from occurring, the injector can now be operated safely at its operating point ($\sim$ 1500 A) without cathode spots that do occur migrating to the insulator at its outer radius. This eliminates a major source of impurities, and over the longer term, damage to the injector. It also serves as a proof of principle, indicating that careful design might productively be undertaken, which for example shunts the cathode spots to a location that eliminates their field-line connection to the injector circuit might be worthwhile.

4.1.3 Insulator Discharge

When BN surfaces were exposed to the plasma during injection, an unwanted surface discharge was observed to develop on them. An example, paired with an in-vessel photo of the geometry for reference, is shown in Fig. 4.7. (The dark patches on the boron nitride visible in the photo in Fig. 4.7 (b) are due to titanium gettering used for improving vacuum base pressure.)

This surface discharge can develop into more serious arcing, causes outgassing and lowers voltage. Steel rings outside the injector were introduced to protect the insulating components from discharge. The segmentation into a stack of rings preserved the dielectric insulation along the length of the injector. Examples, both of a shot where surface discharge develops and a high-voltage shot after rings were installed without it, are shown in Fig. 4.7.

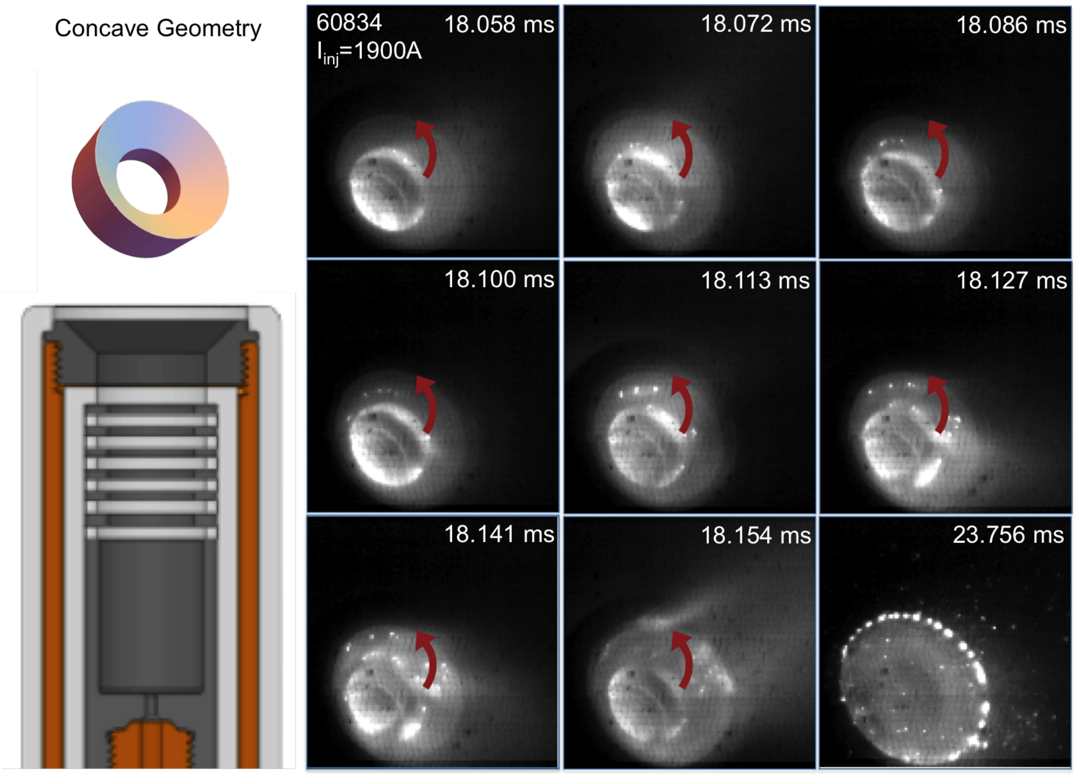

Figure 4.4: Left: Diagram of injector geometry (bottom) and indication of camera viewing angle (top). Right: Cathode spot motion on concave cathode over a sequence of fast camera frames. Red arrow illustrates spot motion direction. Last frame taken from several ms later, after spots have begun causing heating and ablation on boron nitride.

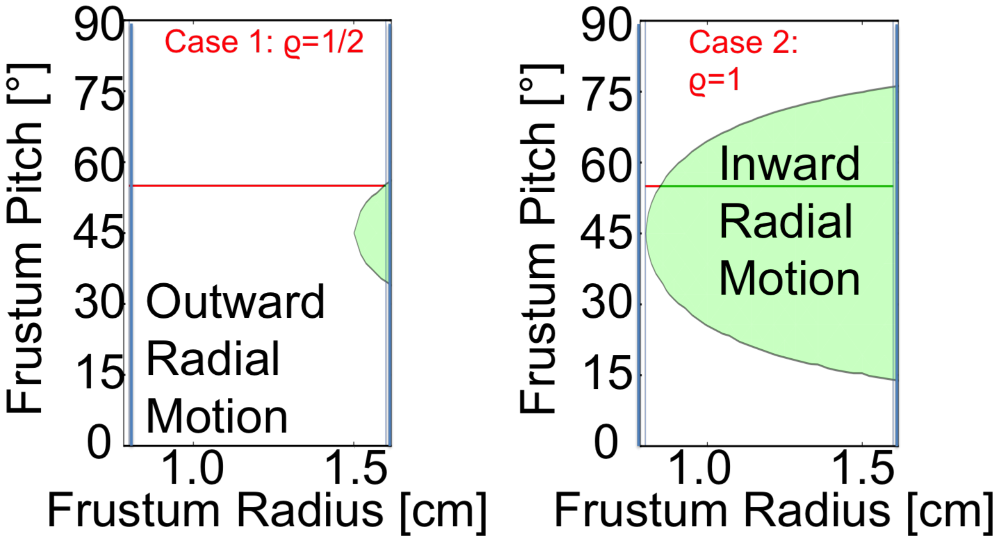

(a) (b)

Figure 4.5: The sign of Eq. 2.26 for $I_{inj} = 1500$ A, $B_z = 0.08$ T is plotted for cases $\varrho = 1/2$ (a) and $\varrho = 1$ (b). The radial interval corresponding to actual constructed dimension is shown. Zones of inward spot motion are shaded. The constant 55 degree angle construction is shown as solid contour.

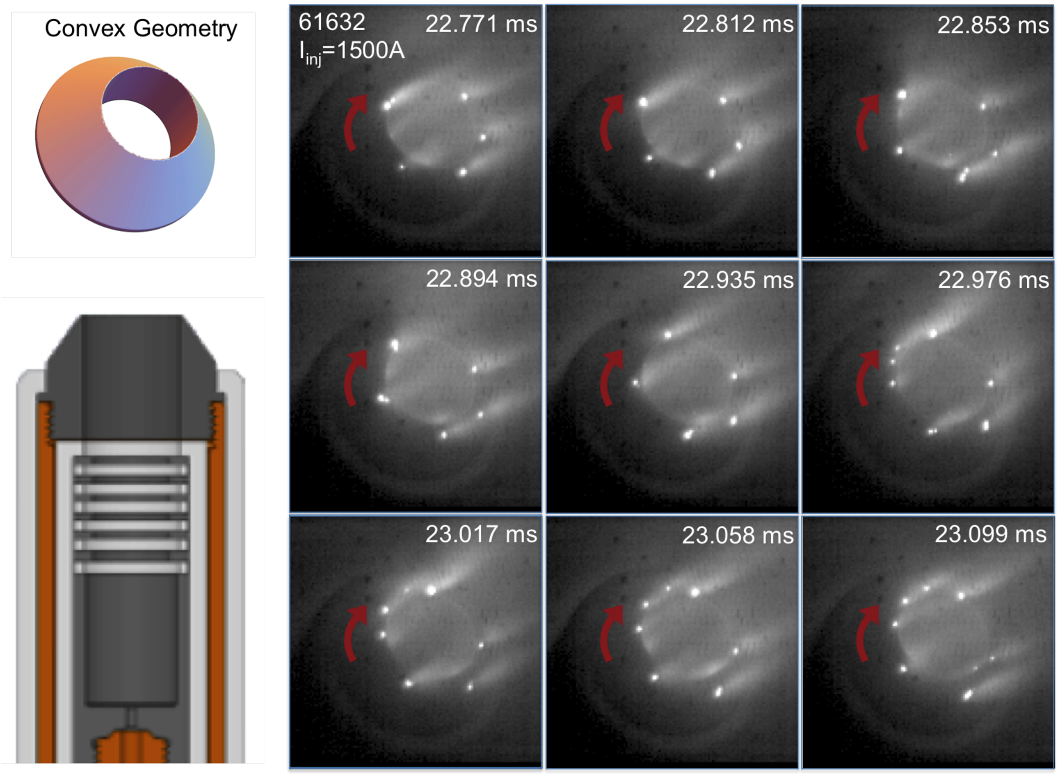

Figure 4.6: Left: Diagram of injector geometry (bottom) and indication of camera viewing angle (top). Right: Cathode spot motion on convex cathode over a sequence of fast camera frames. Red arrow illustrates spot motion direction.

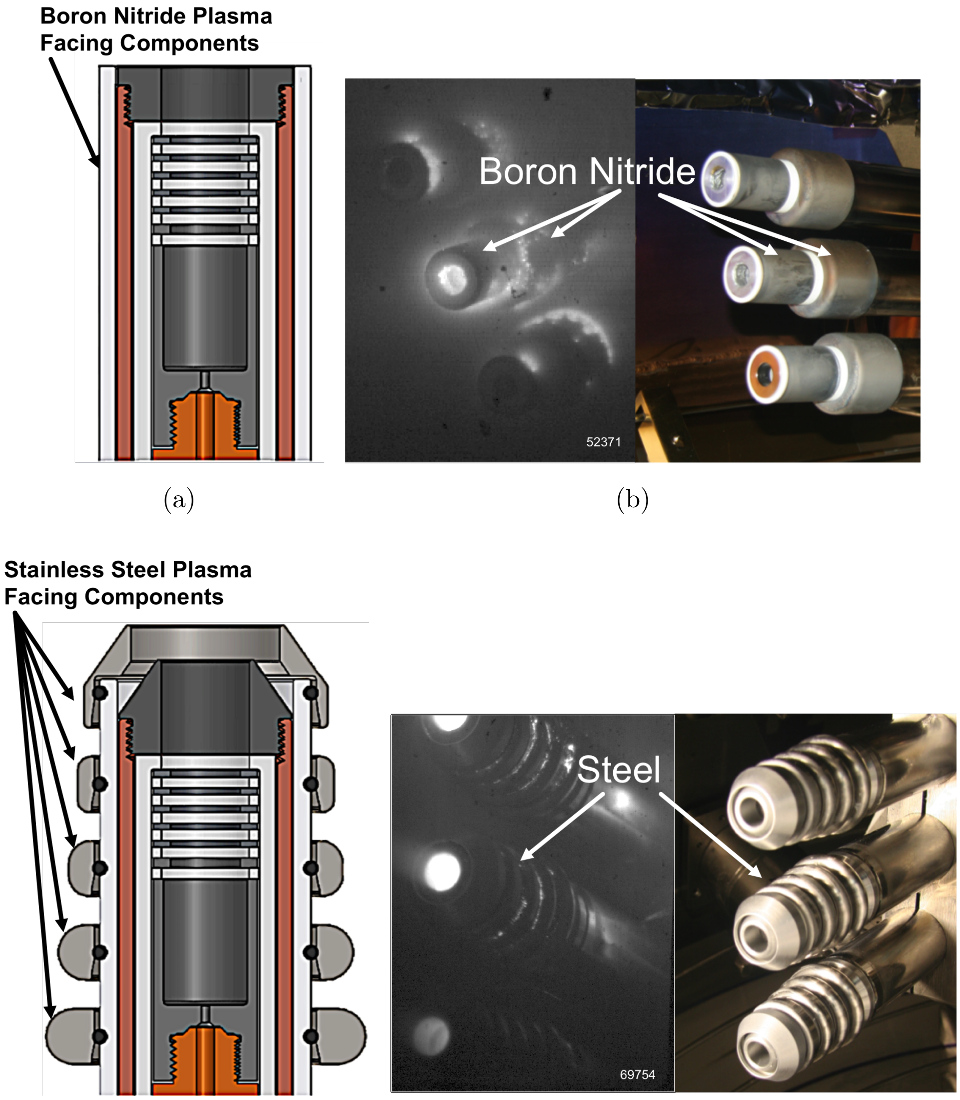

(a) (b)

(c) (d)

Figure 4.7: a.) Drawing of injector with boron nitride plasma-facing components. b.) Operation of this design with insulator surface discharge on boron nitride. c.) Drawing of injector design with ring shields installed. d.) Injection with shielded insulators installed where the discharge has been eliminated.

4.2 Injector Impedance Measurements

Experimental tests of the impedance model formulated in Eq. 2.18 have been conducted. First, the typical $I - V$ scalings obtained from current-voltage ramps during LHI startup are introduced. Then, density dependences of the $I - V$ relationship are investigated in detail via simultaneous measurements of n_b, n_{edge} and n_{arc} for scans of n_{edge} and n_{arc}. This was accomplished by using the injector in ohmically-driven background plasmas. Finally, scalings inferred from these scans are then further supported with time-resolved data from microwave interferometer measurements of during LHI.

4.2.1 Motivation

A scan of a single injector through $I - V$ space to its operating point during LHI is shown in Fig. 4.8. The left pane shows $I_p(t)$, $V_{inj}(t)$, and $I_{inj}(t)$. At right, $I_{inj}(t)$ vs. $V_{inj}(t)$ is plotted for a portion of this interval, where two power-law regimes are evident. The magnitude and scalings of the measured $I_{inj} - V_{inj}$ relation are consistent with that of a double layer, manifesting the widely-observed $I_{inj} \sim V_{inj}^{3/2}$ scaling. However, a transition to $I_{inj} \sim V_{inj}^{1/2}$ at higher current and voltage is also apparent.

The magnitudes of the measured $I - V$ relationships can be compared with expectations. For the portion of data in the $I_{inj} \sim V_{inj}^{3/2}$ regime, Eq. 2.7 can be solved for n_{DL} using estimates of temperature $T_e = 10\,\mathrm{eV}$ and sheath width $d = 10\lambda_{De}$ [27] to obtain an estimate of the density $n_{DL} \sim 10^{19} - 10^{20}\,\mathrm{m}^{-3}$, which falls within the expected range between $n_{edge} \sim 10^{18}\,\mathrm{m}^{-3}$ and $n_{arc} \sim 10^{21}\,\mathrm{m}^{-3}$ from measurements to be shown later in this section.

In the $I_{inj} \sim V_{inj}^{1/2}$ regime, estimating beam density in typical injection conditions: $I_{inj} = 2\,\mathrm{kA}$, $V_{inj} = 1\,\mathrm{kV}$, $A_{inj} = 2\,\mathrm{cm}^2$ leads to n_b of order:

$$n_b \sim \frac{I_{inj}}{ev_bA_{inj}} = \frac{I_{inj}}{e\sqrt{2eV_{inj}/m_e}A_{inj}} \sim 10^{18}\,\mathrm{m}^{-3} \tag{4.1}$$

which is of the same order of the measured n_{edge}, indicating that the beam density is in the range where edge quasineutrality is a relevant constraint. Using $I_{inj} = 2\,\mathrm{kA}$, $V_{inj} = 1\,\mathrm{kV}$ again in Eq. 2.9 for sheath expansion also implies n_{DL} is in the range $n_{DL} \sim 10^{20}\,\mathrm{m}^{-3}$, consistent with the previous estimate. Thus, the magnitude of the measured $I_{inj}(V_{inj})$ in both power law regimes is broadly consistent with expectations of Eq. 2.7 and Eq. 2.18 using measured densities, and with the expected ordering $n_b \sim n_{edge} \ll n_{DL} \ll n_{arc}$.

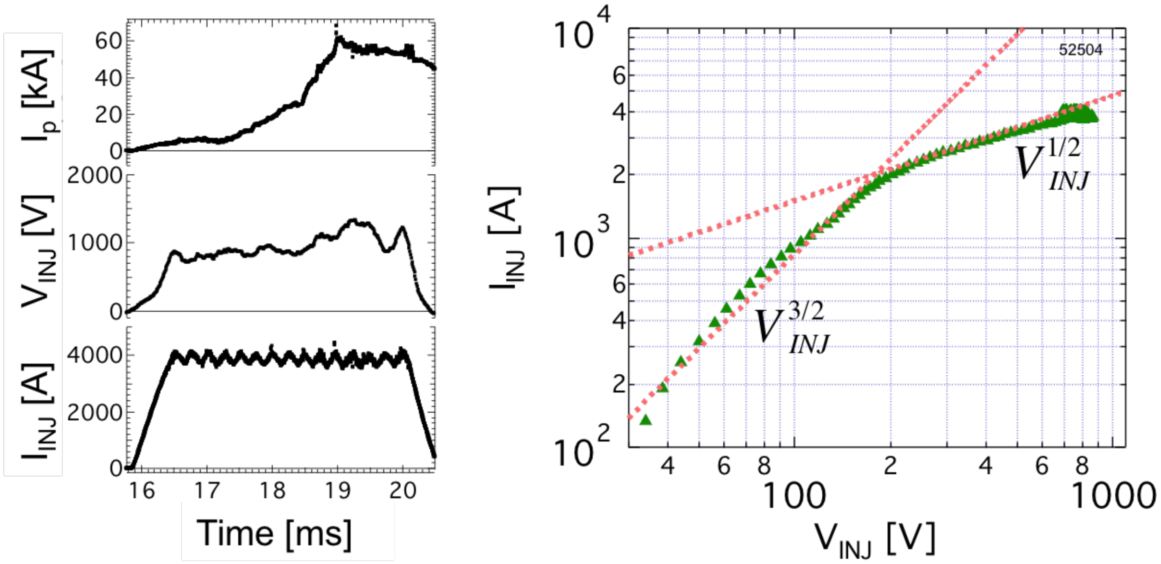

Figure 4.8: Injected current, voltage, and resultant plasma I_p using a single injector.

Current in the $I_{inj} \sim V_{inj}^{1/2}$ regime can be manipulated with gas fueling to the injector. Figure 4.9 shows I_{inj} vs V_{inj} for a series of single-injector LHI discharges, where the injector's fueling rate was scanned from 720 Torr-L/s to 2700 Torr-L/s. The graph clearly illustrates that in the $I_{inj} \sim V_{inj}^{1/2}$ regime, the parameter $I_{inj}/V_{inj}^{1/2}$ is an offset linear function of arc fueling. Because the injector fueling is initiated prior to breakdown and initiation of bias to the injector, the fueling scan in Fig. 4.9 constitutes a scan of both n_{edge} and n_{arc}. A scan with simultaneous measurement and control of n_{edge} and n_{arc} is thus required.

4.2.2 Injection into Ohmic Edge Plasma

This section describes an experimental test of the impedance model using ohmic discharges as a injection targets. They were produced prior to injection and served as background plasmas for injection. To understand what, if either, of n_{arc} or n_{edge} impacts the impedance variations seen above, simultaneous measurements of n_{arc}, n_{edge}, and n_b were made during scans of n_{arc} and n_{edgc}. The scans of n_{arc} and n_{edge} were done using a series of ohmic discharges as background plasma for injection.

Edge density n_{edge} was controlled with D_2 fueling from the 3-injector array and from edge PV-10 valves located on the inboard and outboard sides of the plasma. The Langmuir probe

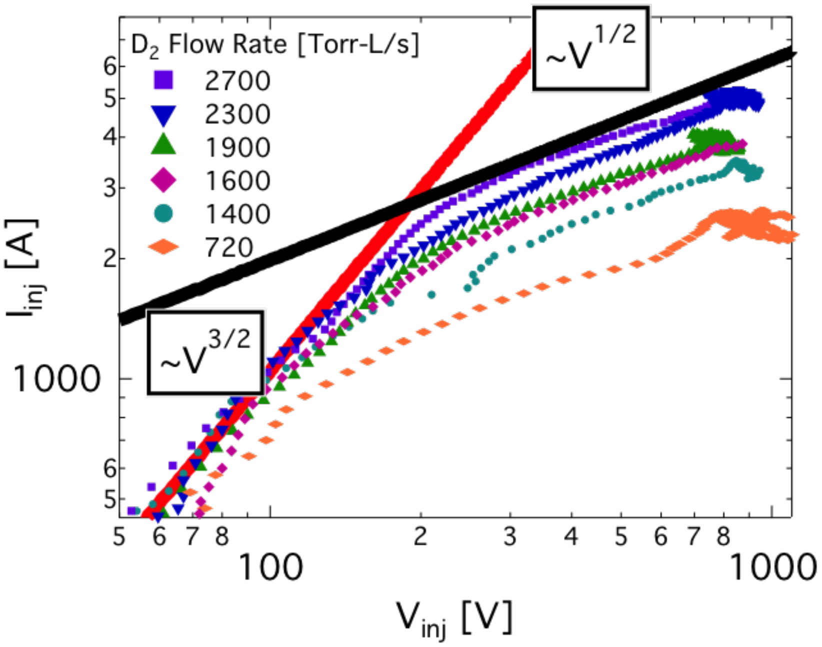

(a)

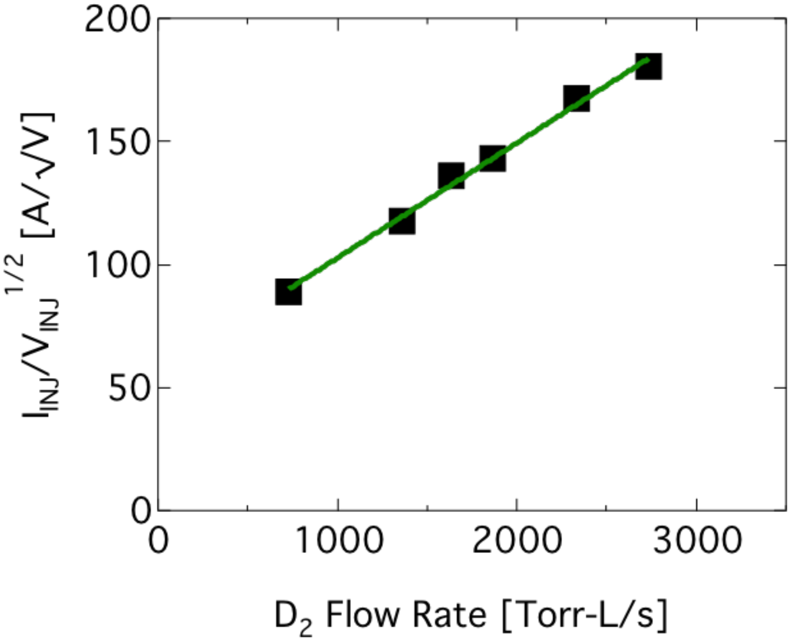

(b)

Figure 4.9: $I - V$ dependence on injector fueling rate. a.) $I_{inj}(t)$ vs $V_{inj}(t)$ for a scan in injector fueling rate. b.) $I_{inj}/V_{inj}^{1/2}$ as a function of fueling rate.

described in Chapter 3 was used to measure n_{edge}. Some care was taken with the setup of the n_{edge} measurement. While the intended measurement is the (order megawatt) beam's drift space density, this cannot be measured directly without compromising the probe. Even avoiding this beam can be difficult. The intense beam expected to be propagating in the edge of LHI discharges appears to be oscillating, and over the course of an LHI discharge, applied vertical fields are ramped from near zero to values consistent with radial stability of ~100kA LHI plasmas. Because of this, a beam strike to the probe can occur, damaging it and/or compromising the data obtained.

To avoid this, a series of ohmic discharges were created as targets for injection. The ohmic discharge served as a source of Maxwellian plasma, and a strong pre-existing vertical field could direct the beam along a field line away from the probe. While the probe was located at the same R, Z of the single injector used for this experiment, it was upstream of the injected beam, separated from it by a scraper limiter, as depicted in Fig. 3.11. The intention was to expose the Langmuir probe to conditions similar to that of the beam drift space, so that the relationship between the density there and at the probe (n_{edge}) was as close as possible without subjecting the probe to a beam strike. The potential disadvantage of this configuration is that the probe n_{edge} measurement is perhaps only indirectly related to the desired quantity: the density of the beam drift space.

The arc density n_{arc} was controlled with injector fueling and measured spectroscopically. Because $n_{arc} >> n_{edge}$, edge fueling can manipulate n_{edge} without affecting n_{arc}. However, arc fueling rate is of the same order as the edge fueling rate, and arc fueling must begin prior to striking the arc. Thus, arc fueling in practice affects both n_{arc} and n_{edge}. As a result the injector fueling scan of n_{arc} also changed n_{edge}, but edge fueling was used to scan n_{edge} at constant n_{arc}.

Fig. 4.10 shows sample data from the ohmic injection series. Plasma currents were generally in the range 50-100kA. At a relatively quiescent (MHD-free) and static I_p period of the discharge (26 ms), a single injector was biased for 2 ms. The injector arc was set to $I_{arc} = 3\,\text{kA}$ and injected current $I_{inj} = 3\,\text{kA}$. The injected current required approximately 1 ms to ramp to its set point, so data was taken between 27 ms and injector shutoff.

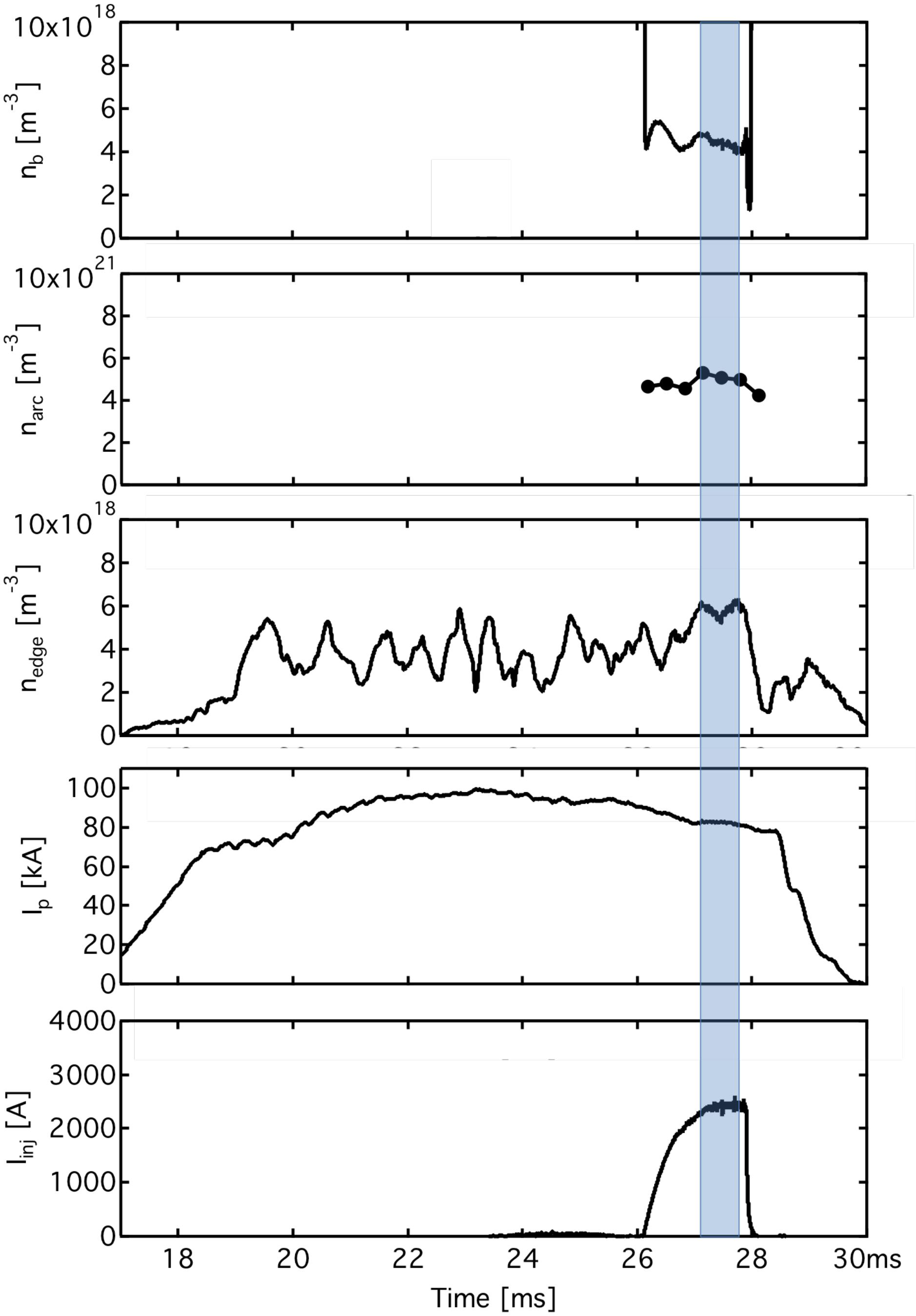

Figure 4.10: Sample data from current injection into an ohmic discharge. From top: Inferred beam density n_b; measured arc density n_{arc}; Langmuir probe edge density n_{edge}; ohmic target discharge current I_p; Injected current I_{inj}. Shaded region indicates time interval over which data was obtained.

For the first phase of this experiment, n_{arc} was scanned. The results of this scan are shown in Fig. 4.11. In Fig. 4.11 (a), it can be seen that both n_{arc} and n_b possess offset-linear dependences on arc fueling. Figure 4.11 (b) shows n_b vs n_{arc}, revealing that $n_b = \beta n_{arc}$ with $\beta = 1/850$ for this injector geometry. Langmuir probe measurements indicate densities less than the beam density n_b for higher arc densities, but the entire scan is consistent with Eq. 2.18 for the case of sheath expansion, where $n_{edge} > n_b$. Because Langmuir probe measurements are upstream from the injector and in the shadow of a local scraper limiter, it is quite likely that the measured n_{edge} is lower than the density in the beam drift region downstream from the injector cathode.

The expectations from this injector at this operating point can now be given

$$I_{inj} = \frac{n_{arc}}{850} e \sqrt{\frac{2eV_{inj}}{m_e}} A_{inj} \tag{4.2}$$

for the case of high tokamak edge density, where sheath expansion dominates the injector impedance.

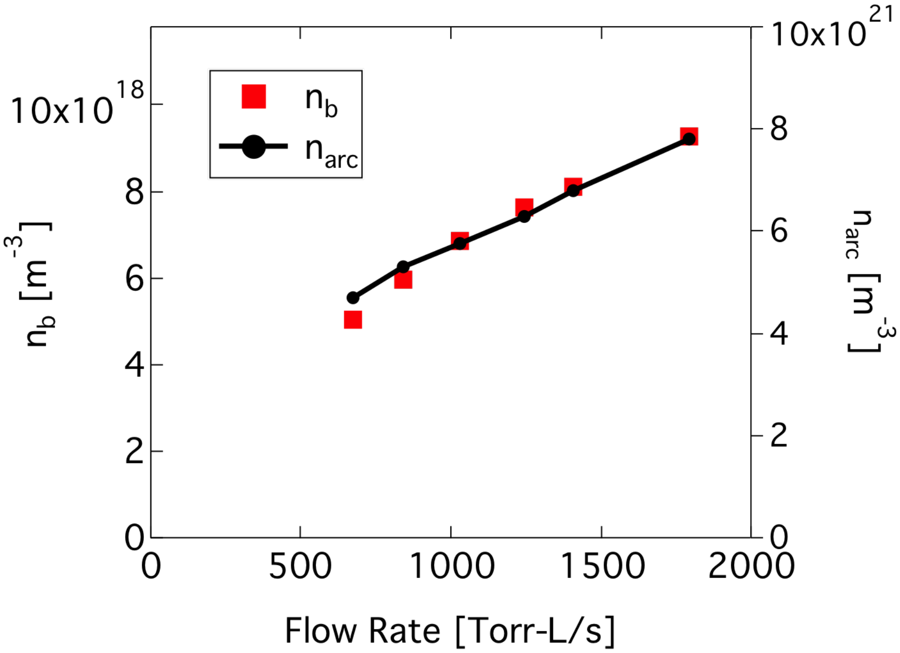

(a)

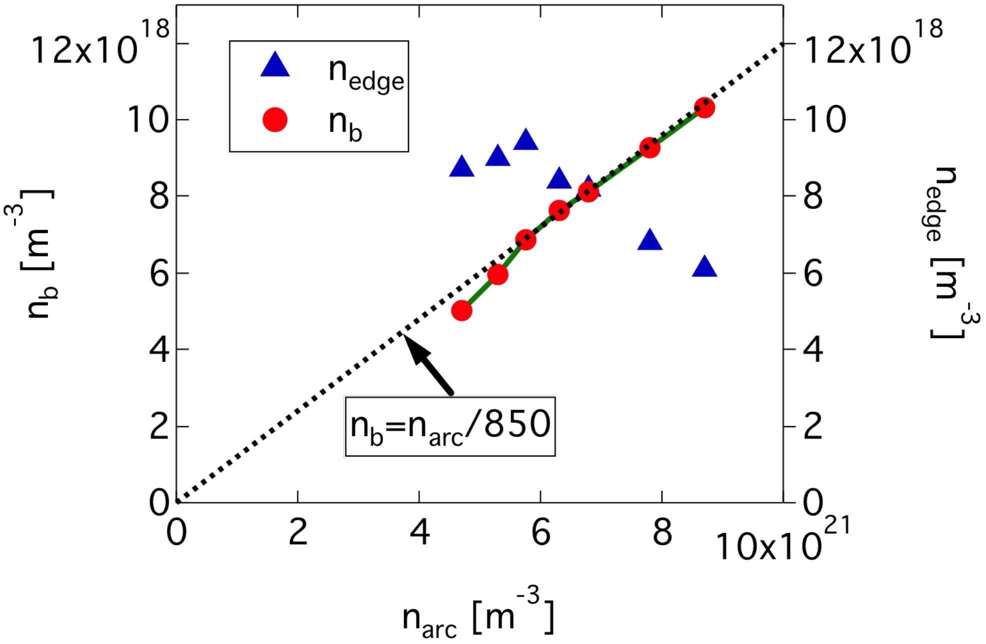

(b)

Figure 4.11: a.) n_{arc} and n_b vs flow rate. b.) n_{edge} and n_b plotted against n_{arc}, showing proportionality $\beta = 1/850$.

In the second phase of this experiment, n_b was obtained for a scan of n_{edge} over a number of ohmic discharges at constant n_{arc}. A plot of n_b vs. n_{edge} from this scan is shown in Fig. 4.12. It indicates an increasing n_b region at lowest n_{edge}, and a saturation at $n_b \approx 6.0 \times 10^{18}\,\mathrm{m}^{-3}$. From Eq. 2.18, two regions are expected: a linear region at low n_{edge} where quasineutrality enforces $n_{edge} = n_b$, and provided $n_{edge} > n_{arc}/850$, a saturation at $n_b = n_{arc}/850$, which for this case was measured to be $n_{arc} = 5.5 \times 10^{21}\,\mathrm{m}^{-3} \Rightarrow n_b \leq 6.5 \times 10^{18}\,\mathrm{m}^{-3}$. The data reflects this saturation. Points at very low n_{edge} would be highly informative, but are difficult to obtain with ohmic discharges without reaching the runaway electron regime.

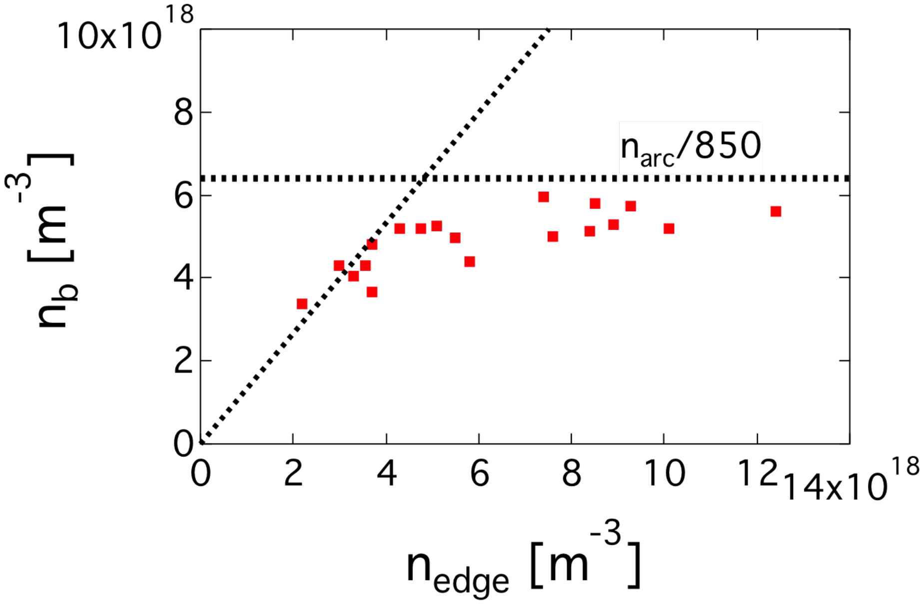

Figure 4.12: Scan of edge density and measured n_b. Expected saturation value of n_b at $n_{arc}/850$ is also depicted.

4.2.3 Microwave Interferometer Radial Chord Density Measurement

Measuring the n_{edge} dependence of Eq. 2.18 is made complex by the natural limits of ohmic discharges, which are in turn required for compatibility with Langmuir probe n_{edge} measurements. While experimental tests of quasineutrality in the beam drift space ideally require a density measurement in this region, other density diagnostics also suggest the reduction of n_b at low n_{edge}.

Indeed, results shown in Fig. 4.12 are supported by measurements of the line-averaged density $\bar{n}_e$ obtained with a radially viewing microwave interferometer. These rapidly-growing tokamak plasmas tend to have broad current and pressure profiles, and it is reasonable to take $n_{edge}(t) \propto \bar{n}_e(t)$. Figure 4.13 shows $n_b(t)$ vs $\bar{n}_e(t)$ for an example 3-injector LHI discharge. The data have been corrected for changing minor radius $a(t)$ using a code that estimates plasma major radial position and shape from flux loop data.

Two regimes are apparent in Fig. 4.13 - a linear regime at lower $\bar{n}_e$ early in the discharge, and at later times, the same saturation at $n_{arc}/850$ as was obtained in the arc scan above. In this case, the arc was measured for these conditions to be $n_{arc} \approx 3.0 \times 10^{21}\,\mathrm{m}^{-3}$, giving an expected saturation at $n_b = 3.0 \times 10^{21}\,\mathrm{m}^{-3}/850 = 3.5 \times 10^{18}\,\mathrm{m}^{-3}$, which is indicated with a horizontal bar in Fig. 4.13.

The line through the $n_b = n_{edge}$ data is not a prediction but a manual fit, since geometric factors related to the density profile of both the tokamak and the beaming particles are unknown. An arrow in both graphs indicates the point in the discharge when the edge quasineutrality limit transitions to the sheath expansion limit. Overall, the behavior observed is similar to that in Fig. 4.12, but the linear dependence on inferred n_{edge}, indicative of a space-charge neutralization limit to n_b is much more evident at lower $\bar{n}_e$.

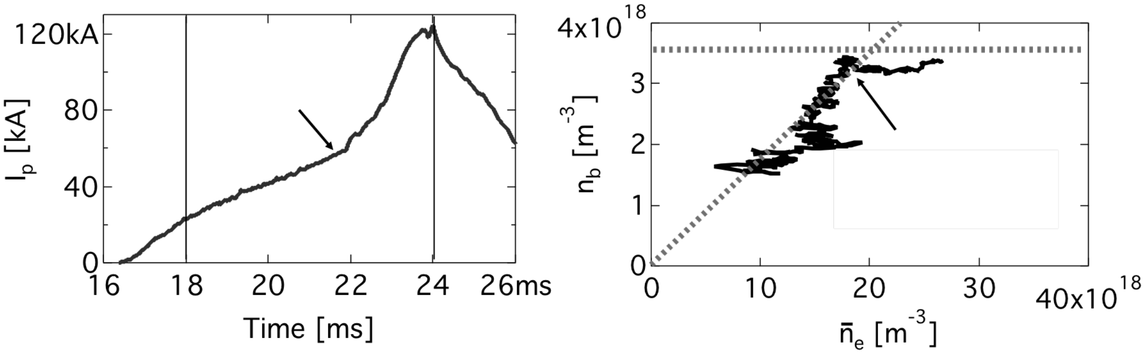

Figure 4.13: Left: $I_p\,(t)$ for discharge 72606. Vertical bars indicate extent of data plotted at right. Right: Density measured with microwave interferometer radial chord. Saturation due to arc density limit also plotted at $n_{arc}/850$. Arrows indicate transition from quasineutrality limit to sheath expansion limit.

4.3 Injector Impedance Control Points

Use of n_{arc} as a control point over injector impedance is desirable because it does not interfere with other discharge programming objectives, and is more straightforward to manipulate than n_{edge}. The impedance model ultimately invokes n_{DL} as its input, not the more easily measured n_{arc}. The conditions setting n_{arc}, and the conditions setting n_{DL}/n_{arc}, described by parameter β, must be understood to make practical use of the impedance model. Key results of these investigations are described in this section.

4.3.1 Dependence of n_{arc} on Fueling and Current

Measurements of n_{arc} were made for a scan of fueling rate and I_{arc} at $B_{TF} = 0.08\,\mathrm{T}$. The data is plotted in Fig. 4.14. Linear dependences of n_{arc} on fueling rate and arc current I_{arc} are found. Operation with and without injection current had no effect within the noise of the measurement. A simple empirical model for n_{arc} measured via pressure broadening of the H-δ and H-γ lines, with reasonable agreement with the experimental data is:

$$n_{arc}[10^{20}\mathrm{m}^{-3}] = I_{arc}\,[\mathrm{A}]\left(6.8\times10^{-3} + 1.5\times10^{-5}F\,[\mathrm{Torr-L/s}]\right) \tag{4.3}$$

where F is the D_2 fueling rate in Torr-L/s. Rendered in m^{-3} for density and 1/s for F, this relation is:

$$n_{arc}\left[\mathrm{m}^{-3}\right] = I_{arc}\left[\mathrm{A}\right]\left(6.8\times10^{17}+4.5\times10^{-5}F\left[\mathrm{s}^{-1}\right]\right) \tag{4.4}$$

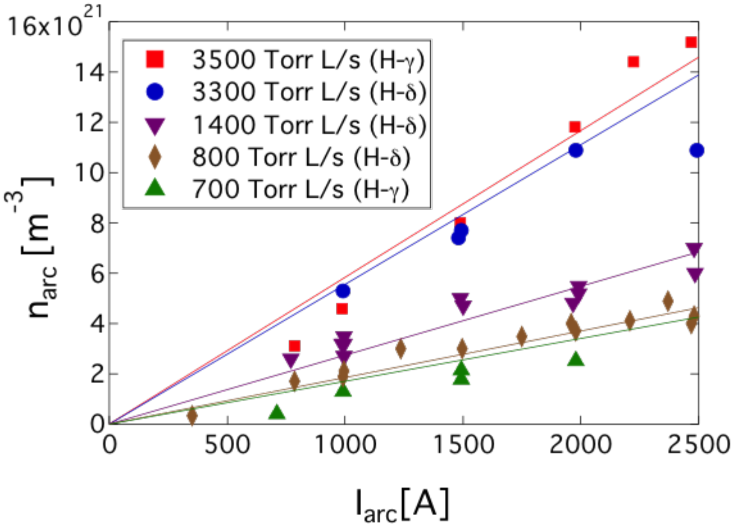

Figure 4.14: n_{arc} vs I_{arc} for various arc fueling rates. Solid lines indicate Eq. 4.4.

The fueling rates here are equivalent to several 10^{22}/s (for a plenum at room temperature $1000\ \mathrm{Torr-L/s} \approx 6.5\times10^{22}\ \mathrm{D^+s^{-1}}$). A typical confinement time using a fueling rate F is:

$$\frac{dN}{dt} = -\frac{N}{\tau_{ion}} + F \tag{4.5}$$

$$\frac{N}{\tau_{ion}} = F \tag{4.6}$$

Densities from Eq. 4.4 are order $\sim 10^{21}\ \mathrm{m}^{-3}$, and within the 10 cm^3 of the injector's arc channel there are order $N \sim 10^{16}$ particles

$$10^{16} = 10^{22}\ \mathrm{s}^{-1}\tau_{ion} \tag{4.7}$$

$$\tau_{ion} = 1\ \mu\mathrm{s} \tag{4.8}$$

which even with ions at $T_i = 10$ eV is only enough time for an ion to travel order cm. This suggests that ion recycling within the arc discharge is not high, and that ion confinement potentially determines n_{arc}, which is far in excess of that needed to sustain the arc current with electron thermal current, which even at T_e =10eV and several $\sim 10^{21}$ m^{-3} is $J_{e,th} \sim$ $100\,\mathrm{kA/cm^2}$.

4.3.2 n_b vs Magnetic Field Strength

The quantity n_b has been measured for a scan of background magnetic field and injector fueling rate. The results of this scan are shown in Fig. 4.15. The data shows n_b has a weak inverse dependence on background field over a factor of two scan in toroidal field. The toroidal field was scanned from 0.04-0.08 T at the injector, while the vertical field component was only 2-5mT. A factor of two change in background field produces a ≈20% change in n_b.

This data shows that impedance in the $I_{inj} \sim V_{inj}^{1/2}$ regime depends on magnetic field, and that higher magnetic field produces a higher impedance, or lower n_b for a given fueling rate. One explanation for this effect is that it results from changing arc properties. Arc ions are only partially magnetized: $r_{L,i} \sim r_{gun}$, and significant impact from field is expected - increasing toroidal field potentially improves confinement and increases temperature. If this results in increasing $T_{e,arc}/n_{arc}$, one would expect higher impedance at higher field. Another possibility related to confinement is that beaming cross-section, A_{inj} scales inversely with field strength. Further exploration of this effect, with n_{arc} measurements is required for a detailed understanding.

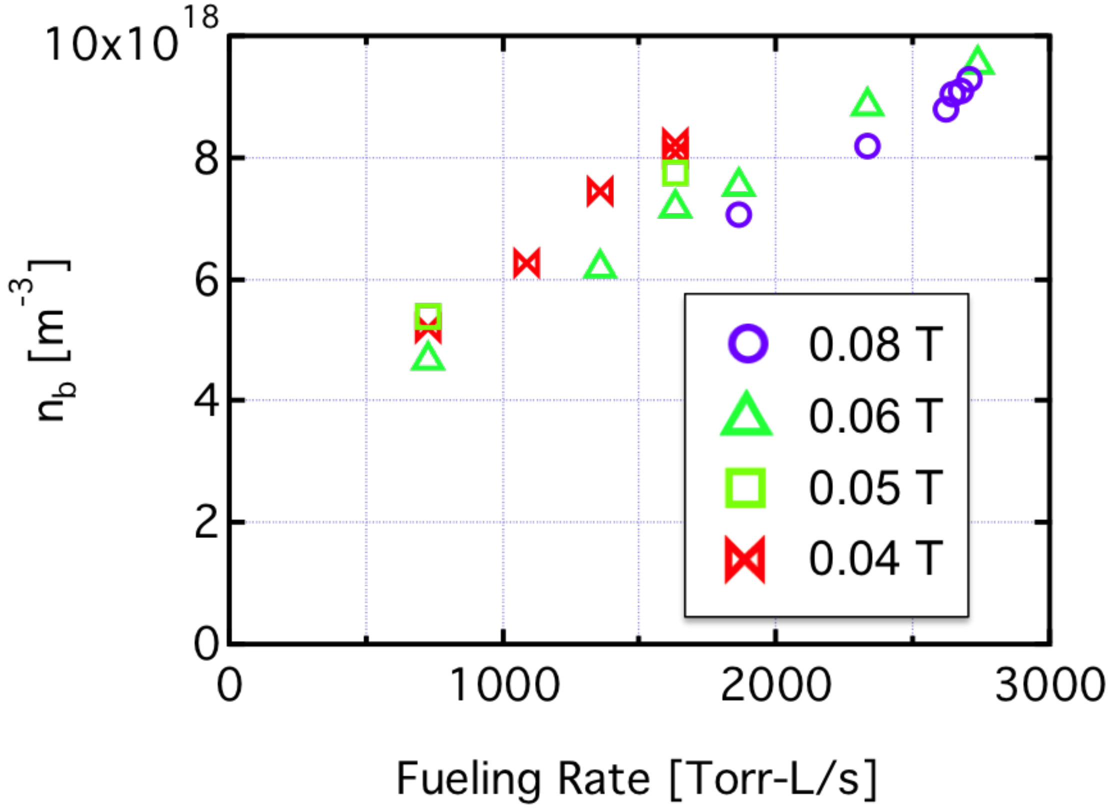

Figure 4.15: Quantity n_b as a function of injector D_2 fueling rate and and background magnetic field strength.

4.3.3 Maximum I_{inj} vs I_{arc}

Maximum achievable I_{inj} was obtained for a scan of injector fueling rate and background magnetic field. This was done via a series of discharges at each field value and fueling rate, where I_{inj} was progressively increased, until the $I_{inj} \sim V_{inj}^{1/2}$ regime was lost and electric breakdown via cathode spots occurred. Figure 4.16 shows a plot of the resulting maximum achievable I_{inj} as a function of injector fueling and background field. The values of I_{inj} plotted were all obtained for several milliseconds in a high-voltage $I_{inj} \sim V_{inj}^{1/2}$ regime without the appearance of cathode spots or other arcing processes. For this scan, I_{arc} remained at 4kA. Currents I_{inj} up to 5.7kA, were obtained. Maximum I_{inj} appears to follow an offset linear trend in fueling rate, similar to that observed for n_{arc}, seen in Fig. **??** on page ??, thought n_{arc} was not measured during this scan.

Previous studies of similar devices which were programmed to minimize injector fueling rate obtained data suggesting a limit $I_{inj} < I_{arc}$ [74, 73, 75]. However, the maximum obtainable injection current in the $I_{inj} \sim V_{inj}^{1/2}$ regime was found in this work not to be limited to I_{arc}, but rather appeared to depend on n_{arc}, which can be programmed via injector fueling rate.

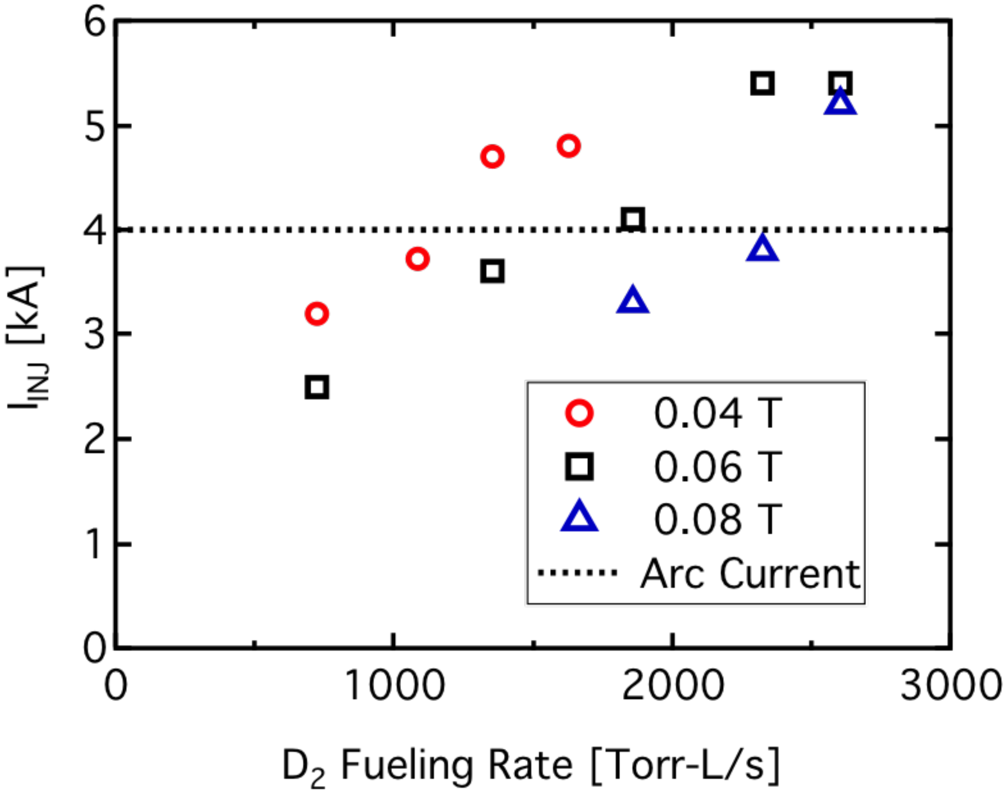

Figure 4.16: Maximum achievable I_{inj} as a function of background field and injector D_2 fueling rate. Dashed line indicates corresponding I_{arc}.

4.3.4 Dependence of Impedance on Arc Anode Length

As the anode of the arc discharge is increased in length, the expected double layer location is farther removed from the arc source plasma. This occurs because the double layer is expected to form at the injector aperture, where diffusion of dense ($\sim 10^{20}\,\mathrm{m}^{-3}$) plasma into the less-dense edge plasma region ($\sim 10^{18}\,\mathrm{m}^{-3}$) creates the space charge layer. Post-mortem examinations of the erosion of the arc discharge anode indicate that the vast majority of the arc anode erosion takes place at the rim close to the washer stack. It is reasonable to assume current preferentially returns to this region. Thus the length of the discharge anode fixes an effective distance between the source plasma and the double layer, in effect altering the n_{DL}/n_{arc} ratio described by β.

Impedance data is consistent with the arc residual plasma density dropping with distance away from the discharge region. As can be seen from Eq. 2.7 on page 20, perveance per area (i.e. $J/V^{3/2}$) is a quantity that is expected to scale with n_{DL}: $J/V^{3/2} \sim d^{-2} \sim \lambda_{De}^{-2} \sim n_{DL}$. Thus, current density at fixed voltage, $J_{inj}/V_{inj}^{3/2}$ is expected to drop with distance from the source.

Measurements in Pegasus taken in identical ramp-up scenarios show this expected increase in impedance, via reduced $J_{inj}/V_{inj}^{3/2}$, as discharge anode length is increased over several design iterations. For three different designs, a shot at full toroidal field, 2kA of arc current, and 460 Torr-L/s of fueling was taken. The resulting $J_{inj}/V_{inj}^{3/2}$ vs. discharge anode length is plotted in Fig. 4.17. The relationship obtained is a decaying exponential, with an e-folding length of 1.6cm. An exponential decline in plasma density with distance from the arc discharge has been measured for similar devices to those used in Pegasus [75], although this was done with a Langmuir probe outside the injector and found longer scale lengths.

This data suggests that discharge anode length is another potential knob for control over the impedance. Alternatively this effect could be viewed as a way to minimize gas flow without affecting the impedance (shorter anode, less gas). A similar scan for $I_{inj}/V_{inj}^{1/2}$ is not available because the emission mechanism for the two longer-length discharge anodes switched to cathode spots before manifesting a $I_{inj} \sim V_{inj}^{1/2}$ regime.

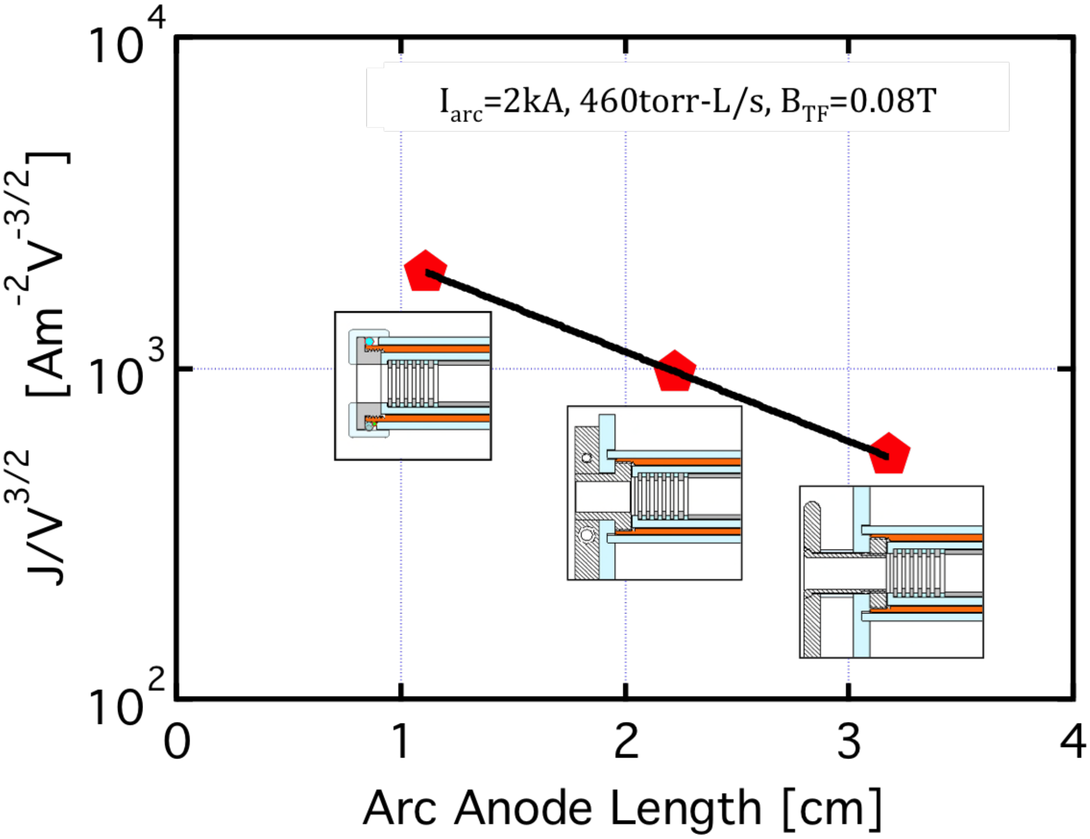

Figure 4.17: $J_{inj}/V_{inj}^{3/2}$ vs. discharge anode length. The corresponding injector design is inset below each point..

Chapter 5

Coherent Beam Magnetic Signature

This chapter addresses the assumption in the impedance model that, during the current growth phase in LHI, the injected current remains a coherent beam as it propagates through the tokamak edge. This assumption is supported by model results from NIMROD [15, 1], which are overviewed in the next section. Prior to the experimental work described in this chapter, there was no direct experimental evidence supporting this particular numerical finding. An analysis of outboard magnetic probe data is presented that shows it is consistent with an electron beam undergoing a small transverse (n, m)=(1, 1) oscillation in the tokamak edge region.

5.1 Motivation

The impedance model assumes a coherent electron stream is launched by the double layer sheath through the tokamak edge plasma, and that the beam density is well-described by $n_b = I_{inj}/\left(e\sqrt{2eV_{inj}/m_e}A_{inj}\right)$. The quantity n_b can be inferred from measured $I_{inj}/\sqrt{V_{inj}}$ when the cross-sectional area of the stream remains near the area of the injector aperture, A_{inj} (for this work, $2\,\mathrm{cm}^2$). Both the magnitude and scaling of impedance data support this assumption.

Modeling [15] of LHI during divertor injection with NIMROD, a 3-D resistive MHD code, also supports this assumption. This modeling has isolated a putative mechanism by which flux is transported from a remote injector at the tokamak edge to the interior confinement region. According to this model of current buildup in LHI, depicted in Fig. 5.1, adjacent passes of the injected current stream approach each other and reconnect to inject "pinched-off" rings of current into the core confinement region. The results are similar to that observed in RSX using current injection with washer-stack guns [127, 114] which found helical motion of streams, attributed there to a kink instability, which possessed a node at the injector and partial line tying at the other end.

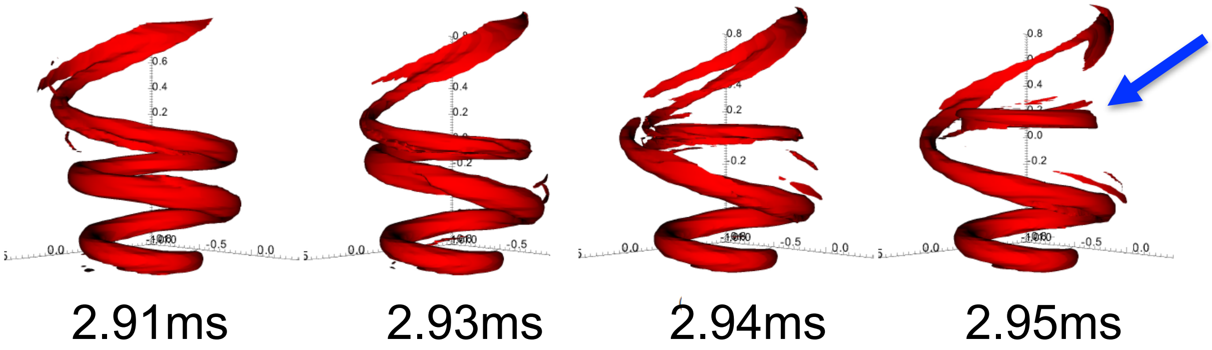

Figure 5.1: From [1], a current filament (red) reconnects to inject a ring (indicated with blue arrow) into the confinement region.

These simulation results possess key similarities to experiment. Among these are a prediction of intermittent n=1 magnetic activity, which is the experimentally observed toroidal mode number. Additionally, a radial scan with an inserted Hall effect magnetic probe has indicated an amplitude peak of magnetic fluctuations near the injector radius, furnishing evidence of radial localization, but providing no distinction between a coherent stream and confinement to a radially localized surface.

The impedance model and NIMROD results rely crucially on the existence of a coherent injected stream, but no direct evidence supporting it has yet been presented. The fast cameras show coherent streams prior to the development of the tokamak-like discharge, however these streams abruptly disappear after relaxation of the stream to a tokamak-like state (see Fig. 1.4 on page 5). Therefore, an analysis of the bursty magnetic signals characteristic of LHI has been done to determine if they are consistent with motion of coherent streams in the edge.

Figure 5.2 (a) shows a typical LHI discharge, with the plasma current plotted against the left axis, and $\dot{B}_z$ measured with an outboard midplane magnetic probe plotted against the right axis. As can be seen in Fig. 5.2 (a), magnetic signals in LHI during the higher-current growth phase possess an intermittent, bursty character. The bursts have an n=1 toroidal mode number. Bursts also time with oscillations of the plasma current. All of these features qualitatively suggest the current loop injection process found in the NIMROD simulations. Figure 5.2 (b) shows a zoom on a typical burst. Measured $\dot{B}_z$ signals are regularly 100s of T/s, have durations of $10^{-5} - 10^{-4}$ s. A more detailed model based on the NIMROD mechanism links the structure of these measured bursts to motion of a coherent current stream in a more quantitative way.

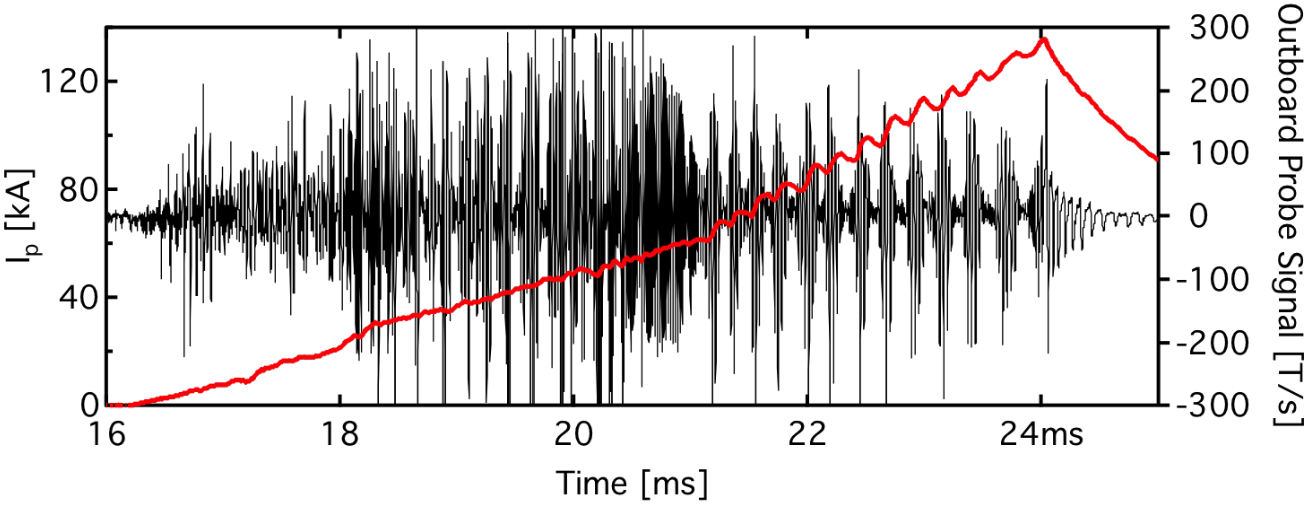

(a)

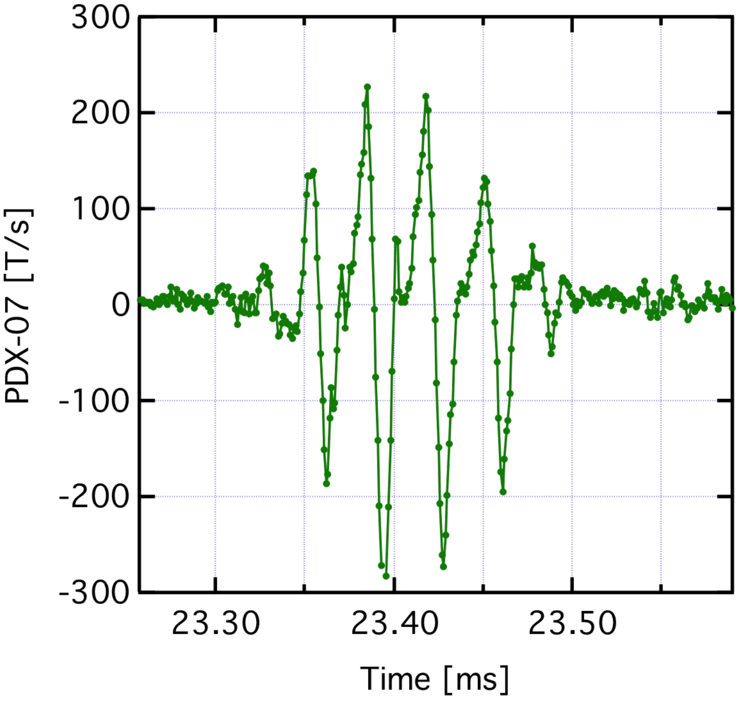

(b)

Figure 5.2: Bursty MHD characteristic of LHI, as measured on outboard probe array probe (See Fig. 5.5). a.) Plasma current I_p and $\dot{B}_z$ measured with an outboard midplane magnetic probe vs time for a typical LHI discharge.

5.2 Theory

An initial model for interpreting outboard $\dot{B}_z$ probe array data, based on (m=1) transverse stream motion in the edge is derived in this section. Its inputs are a relative phase $\Delta\varphi$ and an amplitude ratio T, obtained from Hilbert transforms, of the raw $\dot{B}_z$ (or raw voltage) signals from two probes. The model outputs are the R and Z positions of the stream. The model assumes a straight current line source magnetic field, so expressions remain simple enough to be inverted algebraically, i.e. to a form $f\left(\Delta\varphi, T\right) = R$, and $g\left(\Delta\varphi, T\right) = Z$. This assumption restricts probe pairs used in the model to those in the same poloidal plane. It was developed for use with the outboard poloidal "PDX" probe array in Pegasus, where this requirement is fulfilled.

The model deals entirely with $\dot{B}_z$ signals, (not B_z), which were not integrated for several reasons. This processing introduces drift errors, and prevents use of the full dynamic range of the probe due to occasional signal 'railing' events, when amplitudes exceed the dynamic range of the amplifier attached to the magnetic coil. While this event renders subsequent integrated data subject to an unknown offset, only the small portion of data during the 'rail' event is affected when raw data is used. Additionally, integration attenuates the hypothetical stream signal strength relative to other sources. The stream has a low field strength but presumably rapid (Alfvenic) velocity, making its expected $\dot{B}_z$ very large compared to applied fields, whereas its B_z compared to applied and tokamak plasma fields is small. While signals could then be further filtered, the raw data already possesses low signal to noise ratio. The disadvantage of this approach is that $\dot{B}_z$ is a less intuitive quantity.

5.2.1 Outboard Streams Model Derivation

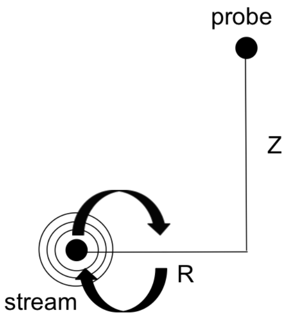

Figure 5.3: Current stream undergoing small rotations in the R-Z plane.

An infinite line current source is taken as an approximation for a high-aspect ratio helical pass. Beginning from the expression for **B** of an infinite line current a distance R_s, Z_s away from the measurement point:

$$\mathbf{B}_{line} = \frac{\mu_0 I_{inj}}{2\pi} \frac{\hat{\theta} \times \{R_s, 0, Z_s\}}{R_s^2 + Z_s^2} \tag{5.1}$$

Substituting $R_s = r - (R - r_0 \cos[2\pi f t])$, and $Z_s = z - (Z - r_0 \sin[2\pi f t])$ corresponding to a circular motion (see Fig. 5.3) in the R-Z plane, and taking the $\hat{z}$ component:

$$B_{z,line} = \frac{\mu_0 I_{inj} \left(-r_0 \sin(2\pi f t) - r + R\right)}{\left(r_0 \sin(2\pi f t) + r - R\right)^2 + \left(r_0 \cos(2\pi f t) + z - Z\right)^2} \tag{5.2}$$

where R is stream radius, Z is stream vertical position, r_0 is the radius of motion of the stream about R, Z, r, z is the location of the measurement point, and f is the frequency of rotation. Differentiating the resulting expression with respect to time gives $\dot{B}_z$ from the circular motion. Substitutions $\delta r = r_0 \sin(2\pi f t) + r - R$ and $\delta z = r_0 \cos(2\pi f t) + z - Z$ have been made for compactness:

$$\frac{\mathrm{d}B_z}{\mathrm{d}t} = -r_0 \mu_0 I_{inj} f \left(\frac{\cos(2\pi f t)}{\delta r^2 + \delta z^2} + \frac{2\delta r(-\delta r \cos(2\pi f t) + \delta z \sin(2\pi f t))}{\left(\delta r^2 + \delta z^2\right)^2} \right) \tag{5.3}$$

$$\frac{\mathrm{d}B_z}{\mathrm{d}t} = r_0 \mu_0 I_{inj} f \frac{\left(\delta\mathrm{r}^2 - \delta\mathrm{z}^2\right) \cos(2\pi f t) - 2\delta\mathrm{r}\delta\mathrm{z} \sin(2\pi f t)}{\left(\delta\mathrm{r}^2 + \delta\mathrm{z}^2\right)^2} \tag{5.4}$$

Using the Weierstrass substitutions $(x^2 - y^2) / (x^2 + y^2) = \cos(2\arctan(y/x))$ and $2xy/(x^2 + y^2) = \sin(2\arctan(y/x))$:

$$\frac{\mathrm{d}B_z}{\mathrm{d}t} = r_0\mu_0 I_{inj} f \frac{\cos(2\arctan(\delta z/\delta r))\cos(2\pi f t) - \sin(2\arctan(\delta z/\delta r))\sin(2\pi f t)}{\left(\delta \mathrm{r}^2 + \delta \mathrm{z}^2\right)} \tag{5.5}$$

Using the angle addition formula for cosine $\cos(\alpha+\beta) = \cos(\alpha)\cos(\beta) - \sin(\alpha)\sin(\beta)$:

$$\frac{\mathrm{d}B_z}{\mathrm{d}t} = r_0\mu_0 I_{inj} f \frac{\cos(2\pi f t + 2\arctan(\delta z/\delta r))}{\left(\delta \mathrm{r}^2 + \delta \mathrm{z}^2\right)} \tag{5.6}$$

Adopting the ordering $r_0 \ll z - Z$, $r_0 \ll r - R$ so $\delta r = r - R$ and $\delta z = z - Z$, flipping rotation direction away from the conventional CCW direction $t \to -t$, and using the even parity of cosine gives the more compact:

$$\frac{\mathrm{d}B_z}{\mathrm{d}t} = \frac{\mu_0 I_{inj} r_0 f \cos\left[2\pi f t - 2\arctan\left[\frac{z-Z}{r-R}\right]\right]}{(z-Z)^2 + (r-R)^2} \tag{5.7}$$

which is clearly a simple sine wave approximation of the $\dot{B}_z$ signal. Inferences about stream location are made with the phase and amplitude characteristics of this approximating sine wave.

For a hypothetical stream signal source in the vessel at 65cm, -10cm, a contour plot of spatial structure of $\dot{B}_z$ signal calculated using Eq. 5.7 is shown in Fig. 5.4. In this figure, locations of outboard probes in the $\dot{B}_z$ array are shown as black dots. The rectangular scraper limiter, with the three inset R,Z locations of the injectors, and the center stack are depicted (left edge of plot), as well as the outline of the vacuum vessel. The injector apertures' toroidal locations are 53 degrees (see Fig. 3.4) toroidally downstream from the half-pipe limiter, where the PDX probes are located - i.e., the first pass of a stream must travel 307 degrees toroidally before it passes in front of the probe array.

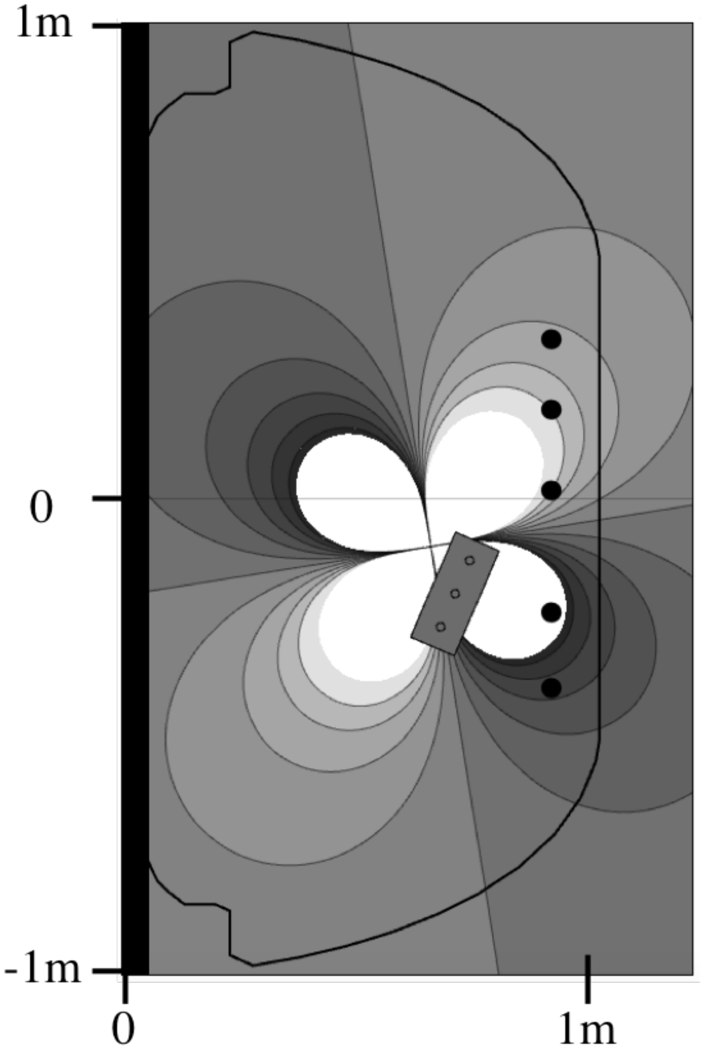

Figure 5.4: From Eq. 5.7, $\frac{\mathrm{d}B_z(r,z)}{\mathrm{d}t}$ for stream located at $R = 0.65\,\mathrm{m}$, $Z = -0.1\,\mathrm{m}$ plotted in the poloidal plane containing the outboard magnetics array. Black dots indicate locations of outboard probes. Outline of Pegasus vessel is included in figure. Centerstack radius is included as solid thick black line at left. Rectangular injector scraper limiter and injector apertures are also depicted.

5.2.2 Model Inversion

Stream R,Z in terms of data inputs

Equation 5.7 is simple enough that it can be inverted for probe pairs to obtain stream R, Z locations in terms of the relative amplitude and phase of two probe signals, without assuming a value for the unknown r_0. From Eq. 5.7, relative signal amplitude and phase measured at two arbitrarily placed probes is:

$$\Delta\varphi = \varphi_1 - \varphi_2 = 2\arctan\left[\frac{z_{p1} - Z}{r_{p1} - R}\right] - 2\arctan\left[\frac{z_{p2} - Z}{r_{p2} - R}\right] \tag{5.8}$$

$$T = \frac{\left\|\left(\frac{dB}{dt}\right)\right\|_1}{\left\|\left(\frac{dB}{dt}\right)\right\|_2} = \frac{\left(z_{p2} - Z\right)^2 + \left(r_{p2} - R\right)^2}{\left(z_{p1} - Z\right)^2 + \left(r_{p1} - R\right)^2} \tag{5.9}$$

which is a set of 2 equations in 2 unknowns - measured amplitude ratio and phase difference in terms of unknown R, Z stream location. All other remaining unknowns drop out.

Inverting these two equations algebraically to solve the forward problem of stream location R, Z in terms of the measured amplitude/phase comparison at two probes is possible. Taking the tangent of both sides of Eq. 5.8 and applying identity

$$\arctan\alpha \pm \arctan\beta = \arctan\left[\frac{\alpha \pm \beta}{1 \mp \alpha\beta}\right] \tag{5.10}$$

removes the trigonometric terms enclosing R and Z:

$$\tan\left[\frac{\Delta\varphi}{2}\right] = \frac{-\left(\frac{z_{p1}-Z}{r_{p1}-R}\right) + \left(\frac{z_{p2}-Z}{r_{p2}-R}\right)}{1 - \left(\frac{z_{p1}-Z}{r_{p1}-R}\right)\left(\frac{z_{p2}-Z}{r_{p2}-R}\right)} = \frac{R\left(z_{p1} - z_{p2}\right) + r_{p1}\left(z_{p2} - Z\right) - r_{p2}\left(z_{p1} - Z\right)}{\left(r_{p1} - R\right)\left(r_{p2} - R\right) + \left(z_{p1} - Z\right)\left(z_{p2} - Z\right)} \tag{5.11}$$

Equations 5.9 and 5.11 can then be solved for R and Z with a computer algebra package. Introducing $U = T + 1$, $S = T - 1$, $\mathit{\Delta} r = r_{p2} - r_{p1}$, $\mathit{\Delta} z = z_{p2} - z_{p1}$, $\mathit{\Sigma} r = r_{p1} + r_{p2}$, $\mathit{\Sigma} z = z_{p1} + z_{p2}$ for compactness, the following expressions are obtained for stream location R and Z, where both positive roots are selected for one solution and both negative roots for the other:

$$R = \frac{T^2 r_{\mathrm{p1}} - T\left(\cos(\Delta\varphi)\mathit{\Sigma} r + \sin(\Delta\varphi)\Delta \mathrm{z}\right) + r_{\mathrm{p2}} \pm \sqrt{T}\left(\Delta \mathrm{r} S \cos\left(\frac{\Delta\varphi}{2}\right) + \Delta \mathrm{z} U \sin\left(\frac{\Delta\varphi}{2}\right)\right)}{T^2 - 2T\cos(\Delta\varphi) + 1} \tag{5.12}$$

$$Z = \frac{T^2 z_{\mathrm{p1}} - T\left(\cos(\Delta\varphi)\mathit{\Sigma} z - \sin(\Delta\varphi)\Delta r\right) + z_{\mathrm{p2}} \pm \sqrt{T}\left(\Delta \mathrm{r} U \sin\left(\frac{\Delta\varphi}{2}\right) - \Delta \mathrm{z} S \cos\left(\frac{\Delta\varphi}{2}\right)\right)}{T^2 - 2T\cos(\Delta\varphi) + 1} \tag{5.13}$$

Either root can represent the physical solution. The other solution is one which locates the stream at an R, Z outboard of the probes. For the case in Pegasus where the probes in the array are at the same major radius, $\mathit{\Delta} r = 0$ and $r_{p1} = r_{p2} = r_p$ and the formulas reduce to:

$$\{R, Z\} = \left\{ r_{\mathrm{p}} \pm \frac{\sqrt{T}\Delta \mathrm{z} \sin\left(\frac{\Delta\varphi}{2}\right)}{T \pm 2\cos\left(\frac{\Delta\varphi}{2}\right)\sqrt{T} + 1}, \frac{z_{\mathrm{p2}} - T\cos(\Delta\varphi)\mathit{\Sigma} z + z_{\mathrm{p1}} T^2 \pm \sqrt{T} S \Delta \mathrm{z} \cos\left(\frac{\Delta\varphi}{2}\right)}{T^2 - 2\cos(\Delta\varphi) T + 1} \right\} \tag{5.14}$$

Obtaining model inputs from data

The phase difference $\Delta\varphi$ and amplitude ratio T can be obtained from data from pairs of probes $\frac{\mathrm{d}B_1[t]}{\mathrm{d}t} = b_1$, $\frac{\mathrm{d}B_2[t]}{\mathrm{d}t} = b_2$ (raw voltage signals can also be used since the calibration factors giving $V_{probe}(t) \rightarrow \dot{B}_z(t)$ drop out) and corresponding Hilbert transforms [128] $\hat{b}_1$, $\hat{b}_2$, using

$$\Delta\varphi = \arctan\left[\frac{\hat{b}_1 b_2 - b_1 \hat{b}_2}{b_1 b_2 + \hat{b}_1 \hat{b}_2}\right] \tag{5.15}$$

$$T = \frac{\sqrt{b_1^2 + \hat{b}_1^2}}{\sqrt{b_2^2 + \hat{b}_2^2}}$$

Uncertainty propagation

The uncertainty calculation has been used here as a device for plotting output. It has been used to indicate regions with a breadth $\pm\sigma$ around the estimated stream R, Z. The R, Z uncertainty resulting from the underlying uncertainty in the amplitude ratio and phase difference for uncorrelated σ_T, $\sigma_{\Delta\varphi}$ for the case in Pegasus where all probes have the same major radius (Eq. 5.14) is:

$$\sigma_R \approx \sqrt{\left(\frac{\Delta\mathrm{z}(T-1)\sin\left(\frac{\Delta\varphi}{2}\right)}{2\sqrt{T}\left(T\pm 2\sqrt{T}\cos\left(\frac{\Delta\varphi}{2}\right)+1\right)^2}\right)^2\sigma_T^2+\left(\frac{\pm\Delta\mathrm{z}\sqrt{T}(T+1)\cos\left(\frac{\Delta\varphi}{2}\right)+2\Delta\mathrm{z}T}{2\left(T\pm 2\sqrt{T}\cos\left(\frac{\Delta\varphi}{2}\right)+1\right)^2}\right)^2\sigma_{\Delta\varphi}^2} \tag{5.16}$$

or in terms of individual amplitudes A, and B where $T = A/B$ and individual phases $\Delta\varphi = \varphi 1 - \varphi 2$:

$$\sigma_R \approx \sqrt{\left(\frac{\Delta\mathrm{z}(T-1)\sin\left(\frac{\Delta\varphi}{2}\right)}{2\sqrt{T}\left(T\pm 2\sqrt{T}\cos\left(\frac{\Delta\varphi}{2}\right)+1\right)^2}\right)^2\left(T^2\left(\frac{\sigma_A^2}{A^2}+\frac{\sigma_B^2}{B^2}\right)\right)+\ldots}$$
$$\overline{\ldots\left(\frac{\pm\Delta\mathrm{z}\sqrt{T}(T+1)\cos\left(\frac{\Delta\varphi}{2}\right)+2\Delta\mathrm{z}T}{2\left(T\pm 2\sqrt{T}\cos\left(\frac{\Delta\varphi}{2}\right)+1\right)^2}\right)^2\left(\sigma_{\varphi 1}^2+\sigma_{\varphi 2}^2\right)} \tag{5.17}$$

and

$$\sigma_Z \approx \sqrt{\left(\frac{\Delta\mathrm{z}\left((T+1)\cos\left(\frac{\Delta\varphi}{2}\right)\pm 2\sqrt{T}\right)}{2\sqrt{T}\left(T\pm 2\sqrt{T}\cos\left(\frac{\Delta\varphi}{2}\right)+1\right)^2}\right)^2\sigma_T^2+\left(\frac{\Delta\mathrm{z}(T-1)\sqrt{T}\sin\left(\frac{\Delta\varphi}{2}\right)}{2\left(T\pm 2\sqrt{T}\cos\left(\frac{\Delta\varphi}{2}\right)+1\right)^2}\right)^2\sigma_{\Delta\varphi}^2} \tag{5.18}$$

or

$$\sigma_Z \approx \sqrt{\left(\frac{\Delta\mathrm{z}\left((T+1)\cos\left(\frac{\Delta\varphi}{2}\right)\pm 2\sqrt{T}\right)}{2\sqrt{T}\left(T\pm 2\sqrt{T}\cos\left(\frac{\Delta\varphi}{2}\right)+1\right)^2}\right)^2\left(T^2\left(\frac{\sigma_A^2}{A^2}+\frac{\sigma_B^2}{B^2}\right)\right)+\ldots}$$
$$\overline{\ldots\left(\frac{\Delta\mathrm{z}(T-1)\sqrt{T}\sin\left(\frac{\Delta\varphi}{2}\right)}{2\left(T\pm 2\sqrt{T}\cos\left(\frac{\Delta\varphi}{2}\right)+1\right)^2}\right)^2\left(\sigma_{\varphi 1}^2+\sigma_{\varphi 2}^2\right)} \tag{5.19}$$

5.3 Experimental Setup

Figure 5.5 depicts relative locations of the array in relation to the injection location, and likely radial location of injected streams. The outboard midplane probe array used to collect data for the model testing. More specifics about the probe array and their locations are given in Section 3.3 on page 56.

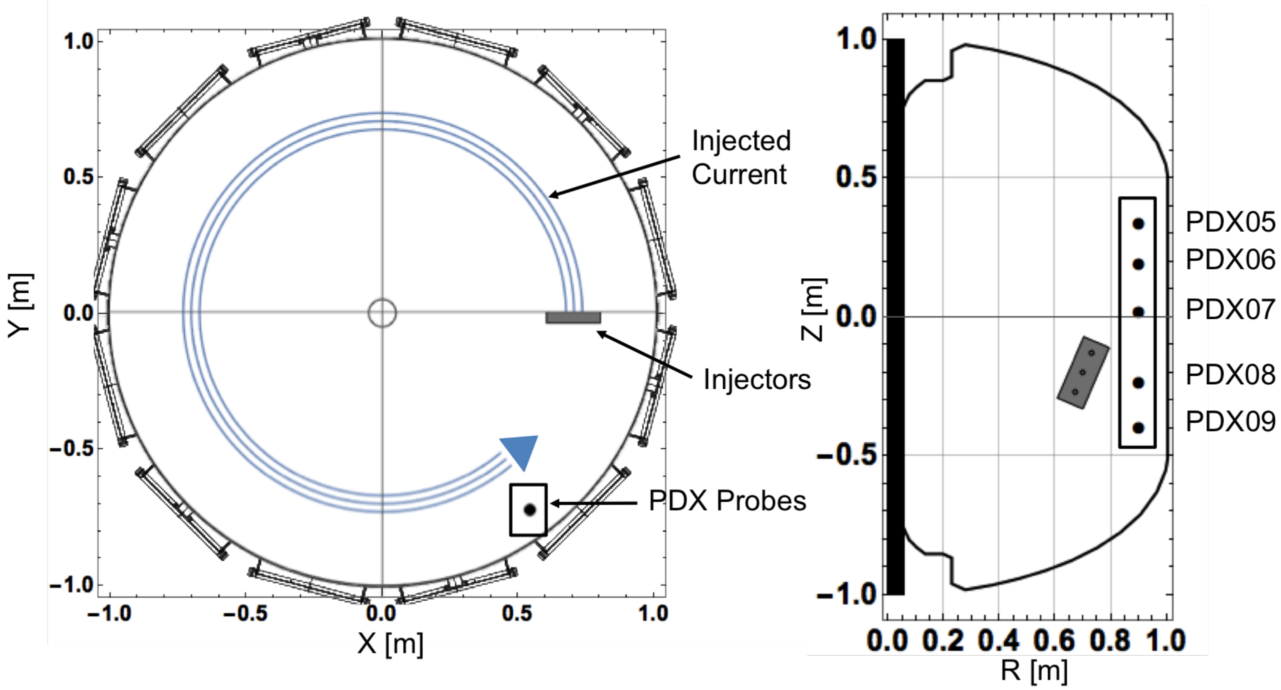

Figure 5.5: Left: Vessel top view, depicting boxed location of PDX probe array and injection location. Circular sectors showing potential stream locations are propagated from the injection location as a visual aid. Right: R, Z projection indicating locations of PDX probe array and injector R, Z . The injectors are separated 53 degrees toroidally from the probe array. Precise probe locations are listed in Table 3.2.

5.4 Model Comparison with Magnetic Data

5.4.1 Initial inverse fit

As a first step to determine if the model produces reasonable results, Eq. 5.7 was used to fit a small section of magnetic data. The probe signals were first band-pass filtered between

10 and 40kHz. The a simultaneous fit to 40μs of data from each of the probes in the array was done. The free parameters used to fit the data were the stream location R, Z and the stream oscillation amplitude r_0. The injected current I_{inj} and the oscillation frequency are both known. The resulting values giving the best fit to the data were $R = 0.58\,\mathrm{m}$, $Z = -0.08\,\mathrm{m}$ and motional amplitude $r_0 = 10\,\mathrm{cm}$.

The model output is shown in Fig. 5.6. The top left frame shows a point plot of the of the entire burst containing the signal data used for the fit, which comes from a 3-injector discharge (#70787). An entire burst is shown for context, and and the 40 μs window of data used for the fit is shaded. The remaining graphs show again the data within the 40 μs window as a point plot, together with the model predictions at that probe r, z for a stream with $R = 0.58$ m, $Z = -0.08$ m, $r_0 = 10$ cm. The closeness of the model fits to their respective measured data traces using a this fit of 3 (R, Z , r_0) scalar unknown parameters (the remaining model inputs I_{inj}, f were not unknowns) for all 5 probes indicates that the model is producing reasonable results.

5.4.2 Comparison with Data

Comparison to the magnetics data suggests a consistent stream R,Z location. Amplitude ratio and phase difference between outboard midplane probe pair signals during the current growth period of LHI discharges show a consistent relationship, with corresponding consistency in the predictions of the model developed here. Pictured in Fig. 5.7 is a sequence of calculated stream R-Z locations using Eq. 5.14 with uncertainties calculated with Eq. 5.17 and Eq. 5.19 using poloidal probe array data from shot 72045. A 10 T/s amplitude uncertainty in the probe signal is allowed for, as well as a 5% error in the phase identification. An elliptical region in R,Z results, with semi-major/minor axes determined by 1-sigma region in R-Z, i.e. $\pm 1\sigma_{R,Z}$ from above. The associated time is indicated in the lower left of each frame.

The output from each probe pair, in blue, is in general agreement across the probe array during the burst, and the mean location isolated by all probe pairs is indicated with a star. The R,Z predictions are consistent in time, consistent across all probe pairs, and consistent

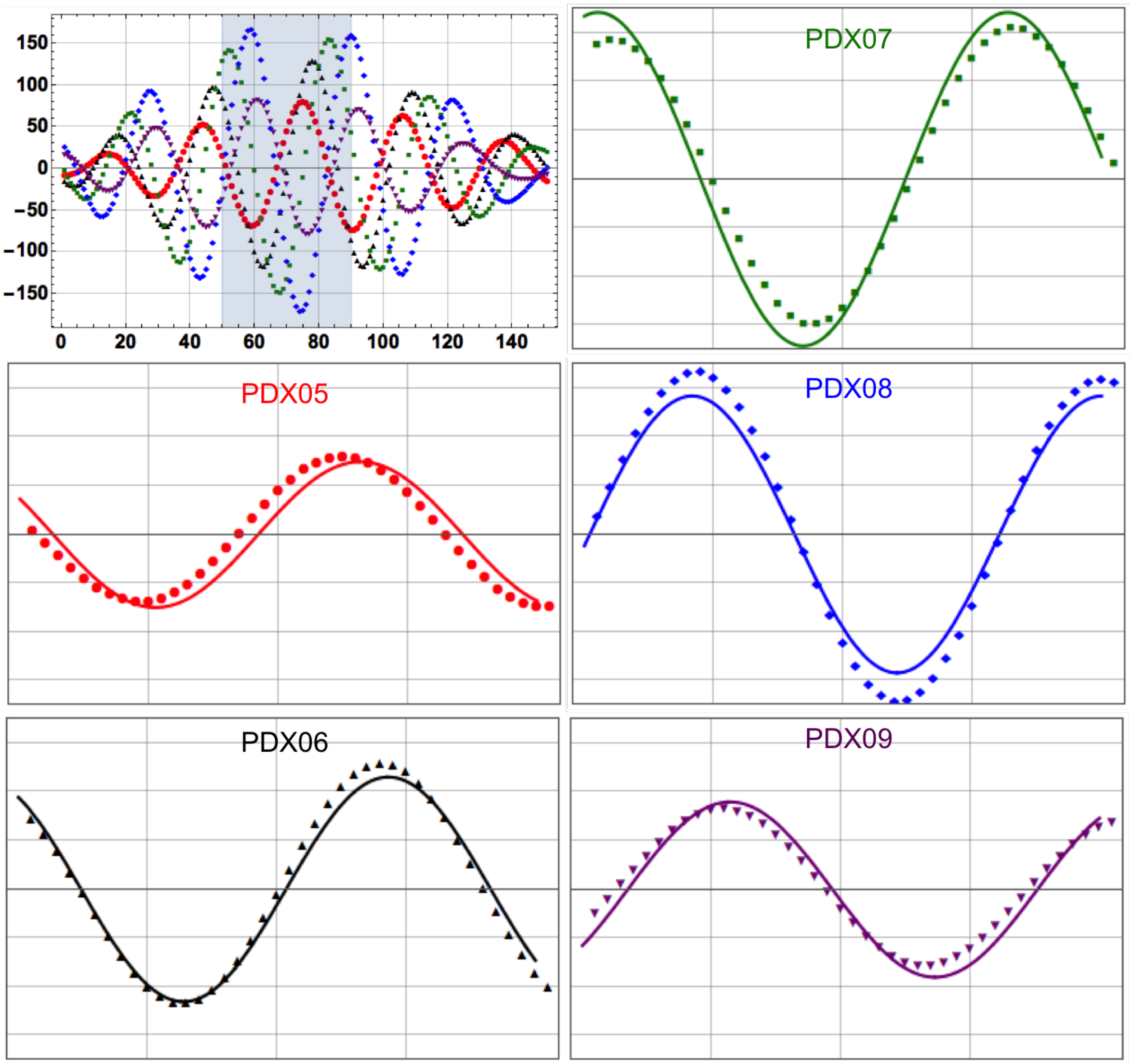

Figure 5.6: The top left pane shows a magnetic signal burst, and the 40 μs window of data used for the fit described in the text shaded. The remaining panes show graphs containing a blow-up of the measured signal at each of the probes in the 40 μs window as a point plot, and the model fit as a solid line.

with previous measurements and NIMROD simulations. While the resulting stream R from this technique is typically several centimeters inboard of the injector, this is very likely an artifact resulting from the simplicity of the infinite line current assumption. Establishing a final determination of R to centimeter accuracy will likely require this initial model, which has prioritized simplicity, be made more sophisticated.

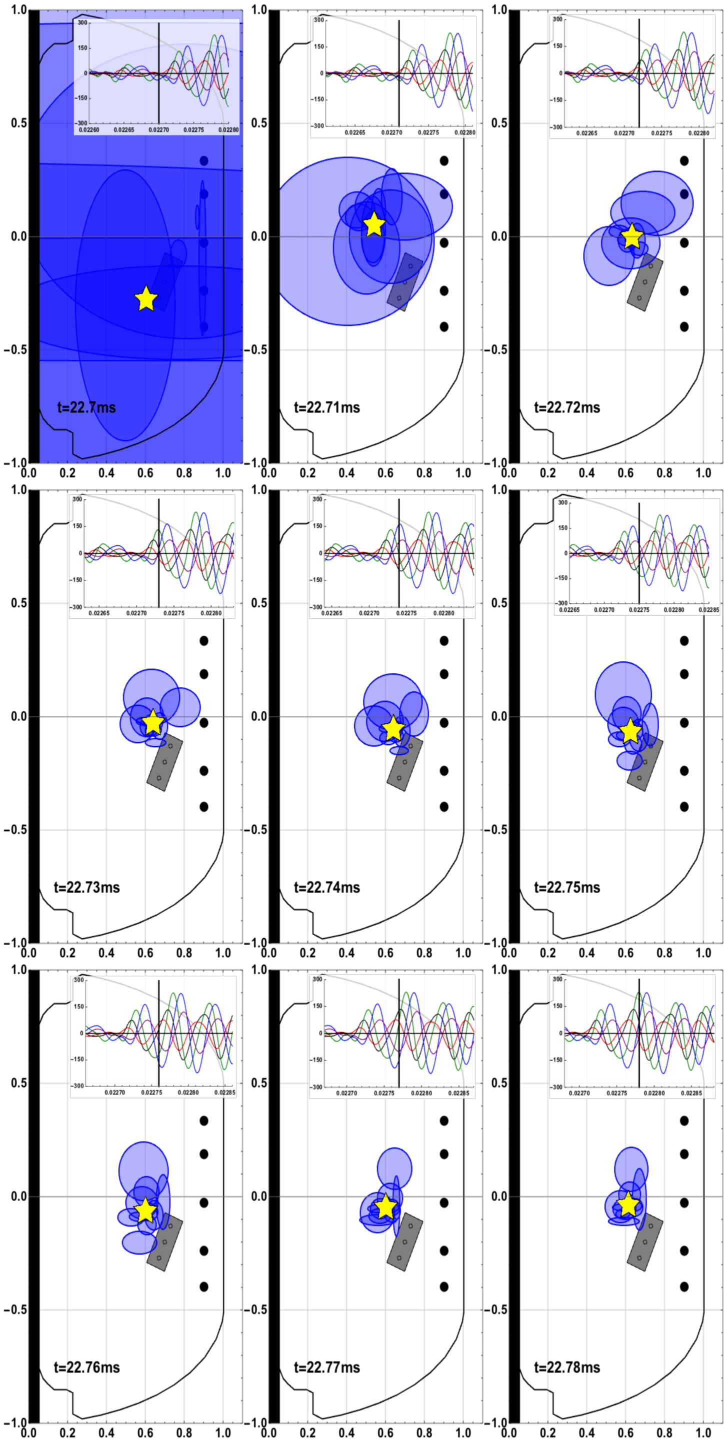

Figure 5.7: Model predictions from Eq. 5.14, with semi-major/minor radii determined by $\pm 1\sigma_{R,Z}$. Contemporaneous $\dot{B}_z$ probe data is in upper inset.

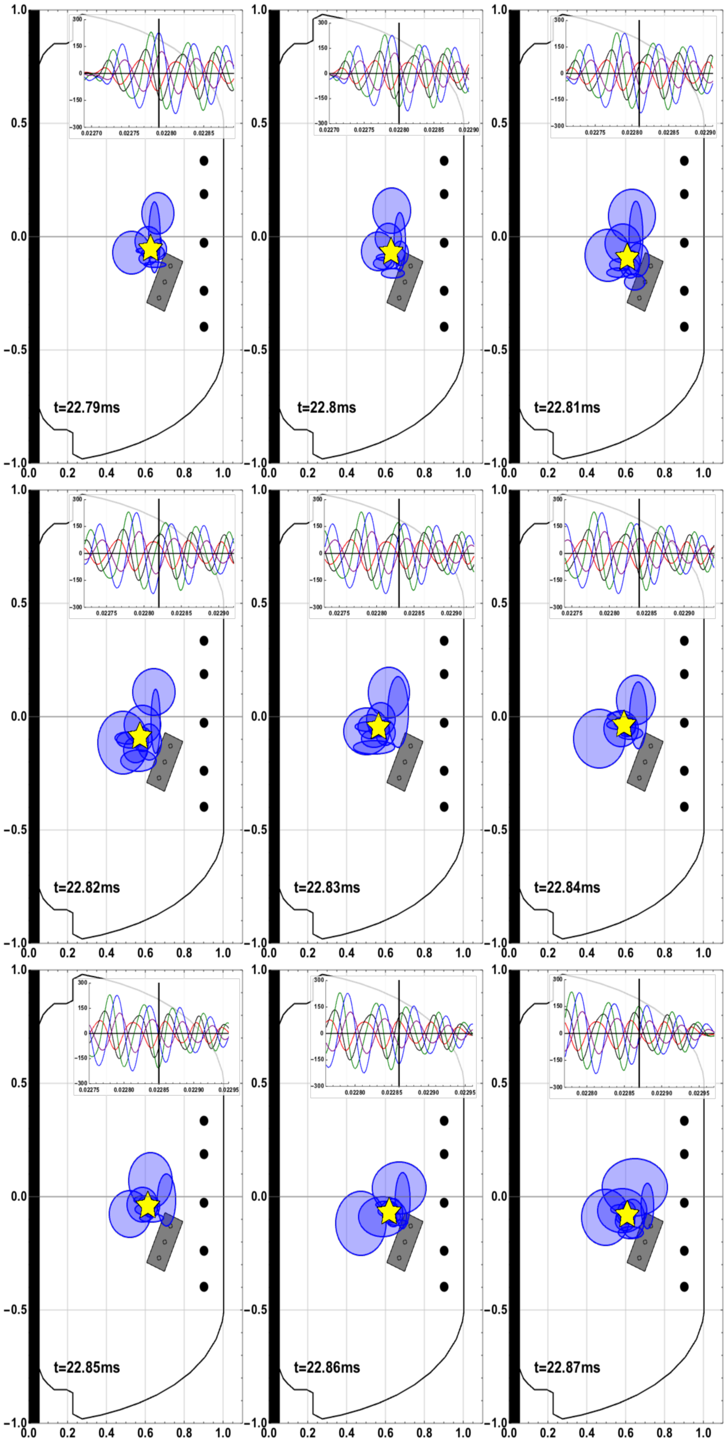

Figure 5.8: Continued from Fig. 5.7

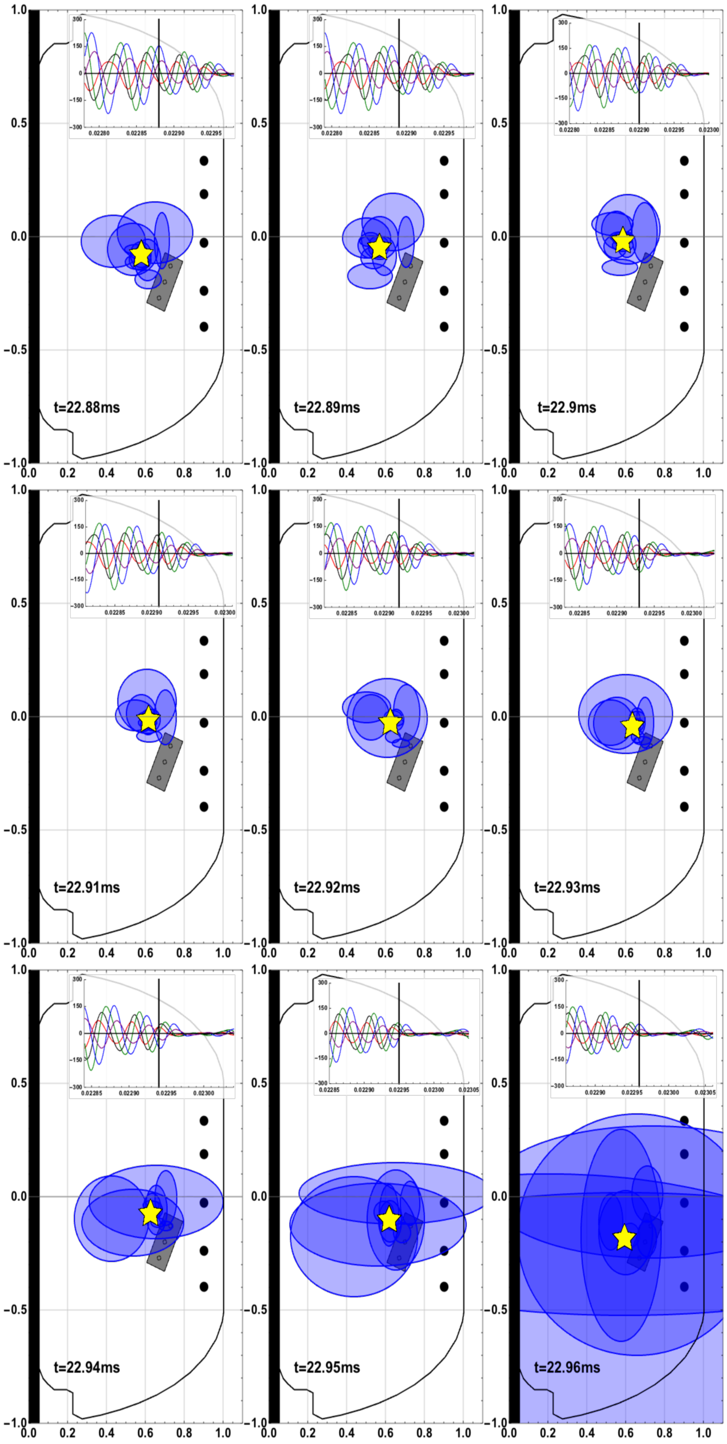

Figure 5.9: Continued from Fig. 5.7

Chapter 6

Conclusion

6.1 Injector Breakdown

The technical requirements for helicity injection include minimized plasma-material interactions, durability over many shots, high voltage standoff, operation with low gas loading, and large emission area. Voltages up to the power supply limit of 2kV, or up to a limit imposed by electrical breakdown via cathode spots on the injector cathode material, are in practice attainable.

Source construction exerts a decisive impact on breakdown thresholds. Recent designs emphasizing lower local density at electrode and shielded insulating surfaces have improved the robustness of the injector to cathode spot breakdown and other forms of arcing. When cathode spots do occur, they can now be directed away from sensitive components that can be damaged and that foster a larger breakdown. This was enabled by a unique optimization of injector geometry with respect to the acute angle rule tendency of cathode spots discussed in the Theory section. While the acute angle rule is well known, typical uses are in a low-current context where any arbitrary acute angle can be introduced. However, the narrow window of parameter space in Pegasus where inward motion can be obtained requires a quantitative acute angle model (obtained from [60]) and involved a unique, quantitative optimization. The tools developed in this work can also allow more extensive design work to be done, for example by guiding spots that occur under overhangs, potentially snuffing them out.

6.2 Impedance Model

Impedance data in Pegasus LHI discharges is consistent with a model employing sheath and beam physics concepts. Biasing a dense, $\sim 10^{21}\,\mathrm{m}^{-3}$ arc plasma cathode to draw electron current into the relatively vacuous $\sim 10^{18}\,\mathrm{m}^{-3}$ region produces a double layer space charge sheath at the aperture of the injector. The applied injection voltage manifests as a localized potential drop over this space-charge sheath, which launches a ~1 kV electron beam along the field line. The impedance expected is that described by the Child Langmuir $I \sim V^{3/2}$ relation. This physics is common for a device of this type, and is observed at voltages below approximately 100V, and currents below approximately 1 kA.

The impedance observed during Pegasus LHI discharges at $\gtrsim 100V$ obeys $I \sim V^{1/2}$. This $I\!-\!V$ dependence is here hypothesized to be an outcome of two independent processes limiting electron beam density n_b according to the dimensional relation $I_{inj} = n_b e\sqrt{2eV_{inj}/m_e}A_{inj}$. The first process is that of sheath expansion, which has the effect of fixing beam density at a value proportional to the density at the double layer $n_b = \alpha n_{DL}$, which in turn is proportional to density of the nearby arc source plasma, n_{arc}, and can be manipulated via arc fueling, arc current, I_{arc}, external field and device geometry.

The second process limiting n_b is the requirement for quasineutral beam propagation, which places a separate upper bound on beam density at the ion density of the drift space in which it propagates. Here n_{edge} is taken as a readily measured indication of this drift space density, giving expectation: $n_b \leq n_{edge}$. The more restrictive of these processes sets the upper limit to beam density, determining V_{inj} for a given I_{inj}.

The quantity n_{arc} represents the most natural control point for programming the impedance. It is more easily programmed than n_{edge}, and does not interfere with other discharge programming priorities, that include for example that n_{edge} be large enough to avoid a runaway regime. Further, n_{edge} tends to naturally rise with higher-I_p discharges, and thus small n_{edge} is generally incompatible with the goal of LHI. On the other hand, the quantities that control n_{arc} during a discharge, namely, I_{arc} and fueling rate, are easily programmed prior to the shot. Setting them appropriately can impose a lower bound on V_{inj} that is independent of expected values of n_{edge}.

However, n_{arc} is not arbitrarily programmable. Excessively low arc fueling rates at fixed I_{arc} can cause material damage to the arc's electrodes. A study of methods of minimizing n_{arc} without damaging the device is thus a reasonable next step. A potential knob for lower n_{arc} without corresponding damage to the electrodes is lower I_{arc}, which has been observed to be a control over n_{arc} both during the course of this work and in others [113, 81]. Minimizing n_{arc} to obtain higher V_{inj} requires simultaneous improvements in cathode voltage standoff. A successful cathode design must sustain high V_{inj} without a transition to cathode spots. The theory and experimental work presented above provide some guidelines and first steps toward accomplishing this task.

6.3 Magnetic Analysis

The method of MHD signal interpretation developed here suggests several conclusions. First, experimental evidence has been obtained that is consistent with both the assumptions used in the impedance model and with results of NIMROD simulations, suggesting that injected current remains a coherent stream in tokamak edge. Magnetic probe signals are in agreement across all the pairs of the array on a signal origin at a localized R, Z in the outboard edge, near the injector radius R_{inj}, somewhat above the vertical location Z_{inj}. This finding applies in the poloidal plane of the probe array, almost a full toroidal rotation downstream from the injector.

It is also consistent with the reconnection-based current drive mechanism isolated in NIMROD simulations, as the amplitude of stream oscillation r_0 is large enough to return the first pass of the kink unstable stream to the R_{inj}, Z_{inj} of the injector, enabling the reconnection between helical passes observed in the model.

The poloidal mode number of the stream motion is consistent with m=1. Additionally, the gyration behavior presented here is consistent with observations of current streams produced with similar guns in linear devices operated at similar parameters [114, 129, 130, 131]. The observed handedness of the motion was consistent for all shots examined. Motion was found in the '$\mathbf{J} \times \mathbf{B}$ direction' expected at a mostly field-aligned current which slightly deviates from $\mathbf{J}||\mathbf{B}$. Further research into the details of this dynamic is however necessary.

Appendix: Unipolar Arcing During LHI

Simple model of unipolar arcing to guide floating component design

Floating ring armor installed on the injector and shown in Fig. 6.1 have improved achievable V_{inj}. However, during periods of high V_{inj}, floating armor will occasionally break down via cathode spots, and can also be observed to glow, incandescing even after the discharge ends. An example is shown in Fig. 6.2. Another example, together with a cathode spot that has developed on a ring and migrated to the boron nitride insulator is shown in Fig. 6.3.

The local scraper limiter has also been observed to glow at regions of plasma contact during LHI, but does not break down. Breakdown occurs on floating components despite their lack of galvanic connection to the injector circuit, and does not occur in ohmic-driven discharges. This unipolar arcing occurs on the floating cathode frustum shield and the rings in the >1kV range, and is currently the limit to higher-voltage operations - particularly as it occurs on the frustum shield - as applied voltage thereafter often drop and components can be damaged.

Unipolar arcing is widely seen to occur in tokamaks on floating PFCs during ramp-up and instabilities to due to hot, dense edge plasma or an unconfined hot electron component. According to the standard model [51, 8], plasma bombardment at high T_e increases the floating potential $\Delta V_{sheath} = \frac{1}{2} T_e \log \left[\frac{2\pi m_e}{m_i} \right]$ to the point of breakdown. Here floating potential is obtained by setting ion Bohm flux equal to a Boltzmann-electron component.

In LHI plasmas, additional hot electrons produced by the injector are expected, and are very likely connected with the injector breakdown particular to LHI. When the customary

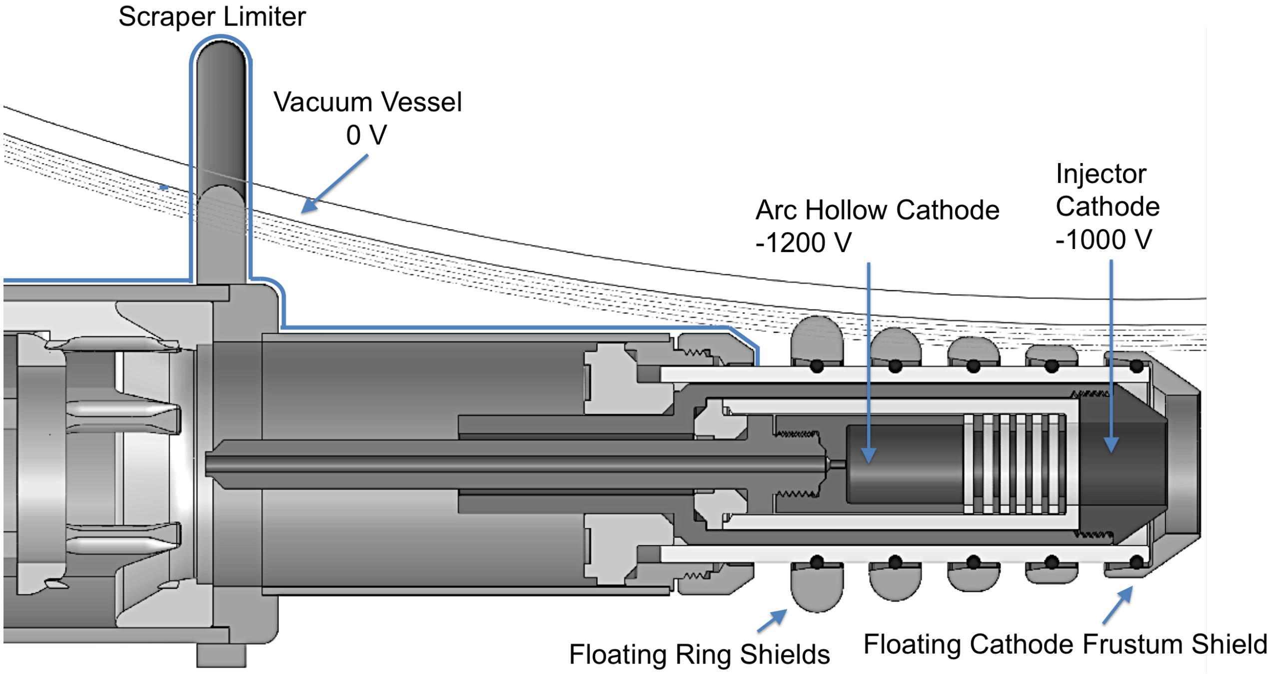

Figure 6.1: Injector geometry with installed rings. Blue contour indicates galvanically connected components. Nominal voltages for driven conductors are indicated.

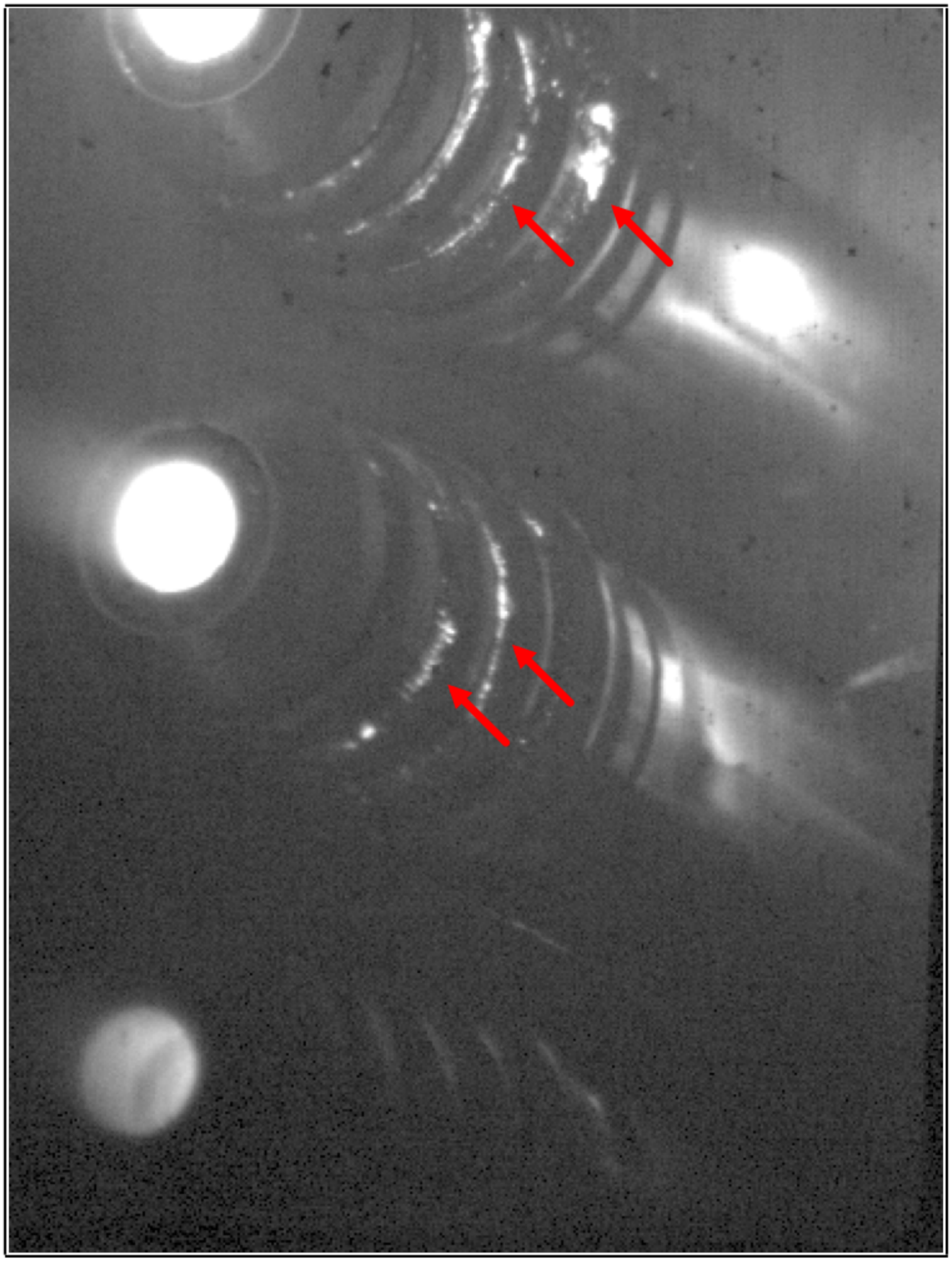

Figure 6.2: Injectors design depicted in 6.1 during operations. Glowing patches indicated.

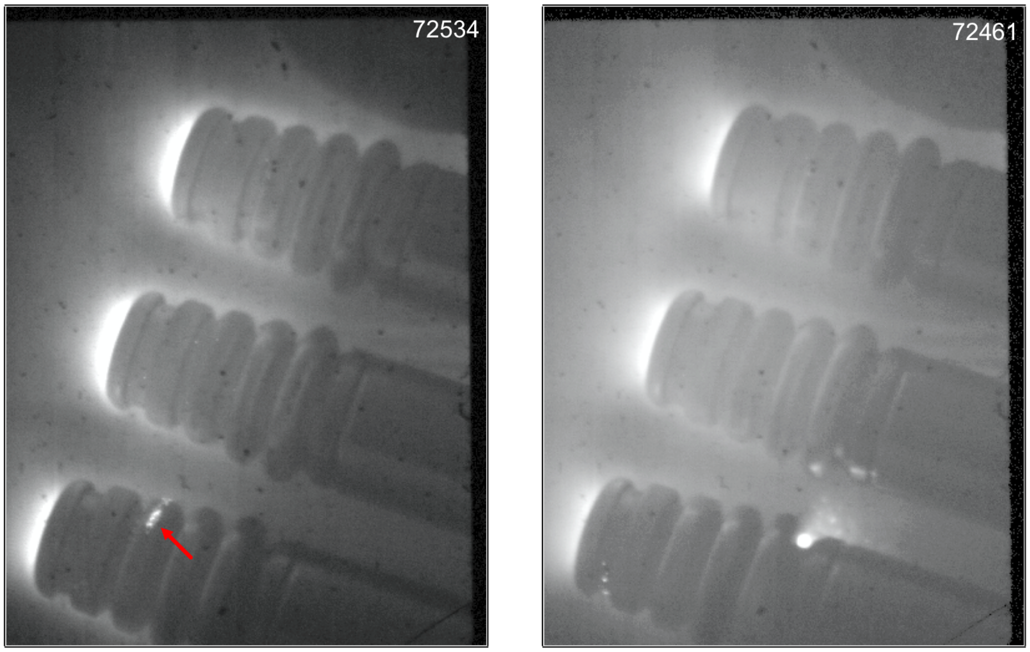

(a) (b)

Figure 6.3: a.) Glowing on ring during normal ∼1 kV operation. b.) Cathode spot on last ring of lower injector, which has migrated to insulator.

expression for floating potential is modified to account for the presence of a hot monoenergetic electron component, threshold voltage behavior results, which can be used as a simple breakdown criterion, and guideline for robust design.

The standard model for outbreak of unipolar arcs can be augmented to include the contributions of a hot electron beam, to obtain a similar criterion for breakdown of floating components during LHI, where these beaming particles are expected to originate from the injected beam, i.e. $V_{beam} = V_{inj}$, but $I_{beam} \ll I_{inj}$. The V_{beam} corresponding to breakdown would be regarded as the upper limit to V_{inj} before breakdown occurs on floating shields.

Impinging beam electrons are assumed to be at high voltage compared to local electron temperature $V_{beam} \gg T_{e,SOL}$ and floating potential $V_{beam} \gg V_{float}$ so that beaming particles are not affected by the sheath voltage, and beam density incident on the floating component, n_s is much less than background plasma density, n_{SOL}, in the scrape-off layer: $n_s \ll n_{SOL}$. Electrons are magnetized, impacting the field-projected area A_{proj} of the total plasma (ion)-exposed area A_{tot}. In addition to the customary ion saturation current and Boltzmann electron terms, current continuity now includes a term corresponding to incoming hot electron current I_{beam} and induced secondaries:

$$0 = I_{float} = I_{i,sat} + I_{e,th} + I_{beam}\left(1 - \delta_{se}\left[V_{beam}\right]\right) \tag{6.1}$$

$$0 = n_{SOL}e\sqrt{\frac{T_{SOL}}{m_i}}A_{tot} - n_{SOL}e\sqrt{\frac{T_{SOL}}{m_e}}\exp\left[\frac{-V_{float}}{T_{SOL}}\right]A_{proj} - n_s e\sqrt{\frac{V_{beam}}{m_e}}A_{proj}\left(1 - \delta_{se}\left[V_{beam}\right]\right) \tag{6.2}$$

$$\ln\left[\frac{A_{tot}}{A_{proj}}\sqrt{\frac{2\pi m_e}{m_i}} - \left(\frac{n_s}{n_{SOL}}\sqrt{\frac{2\pi V_{beam}}{T_{SOL}}}\left(1 - \delta_{se}\left[V_{beam}\right]\right)\right)\right]T_{SOL} = V_{float} \tag{6.3}$$

where ion saturation is $I_{i,sat}$, electron thermal current is $I_{e,th}$, and account has been taken in I_{beam} of secondary electron emission, via coefficient δ_{se}. The left term in the log is the customary partially-magnetized V_{float}, with the added hot e- term and resulting secondaries at right. Figure 6.3 describes beam-induced charging of a floating conductor in a plasma. Incoming negative charge from the incident beam is balanced by reductions in the thermal electron flux. A singularity occurs at $I_{beam} = I_{i,sat}, I_{e,th} \rightarrow 0$, where I_{beam} has fully replaced the 'hot tail' comprised by $I_{e,th}$, forcing $V_{float} \rightarrow$ -∞. While V_{float} is generally a gradual function of the log, near this singularity it drops very sharply negative, in practice leading to $V_{float} \rightarrow V_{beam}$, where beam particles can be turned back, or alternatively, prior to obtaining sheath field $V_{beam}/\lambda_{De} \sim 10^5$V/cm, to sheath breakdown. Requiring $I_{beam} < I_{i,sat}$ bounds the operating space according to:

$$V_{beam} < \frac{m_e}{m_i} \frac{A_{tot}^2}{A_{proj}^2} \frac{n_{SOL}^2}{n_s^2} \frac{T_e}{\left(\delta_{se}\left[V_{bias}\right] - 1\right)^2} \tag{6.4}$$

For most PFC materials, between 100V-1kV, $\delta_{se} \approx 1$ [8], drastically reducing beam-induced charging. Because $\delta_{se} \approx 1$ in the experimental range, expected breakdown voltage behavior from Eq. 6.4 is largely determined by the location of $\delta_{se}[V] < 1$. For molybdenum, above ~900V, where $\delta_{se}[V] < 1$, threshold divergence of V_{float} quickly occurs and this log [0] condition can be viewed as a rough threshold voltage for breakdown.

Using δ_{se}[V] data from [8] and $T_{SOL} \sim 10$ eV, Fig. 6.4 shows this breakdown condition plotted against its various dependences. For the Mo frustum shield, the breakdown condition contour is plotted together with a shaded region where $V_{float} > -40$ V as a function of hot particle fraction Log[n_s/n_{SOL}] and incident energy Log[V_{beam}]. The very fast divergence of V_{float} to infinity from -40V, a rather typical and 'safe' value, demonstrates the utility of the divergence to infinity as an effective breakdown threshold condition. The relationship of the breakdown curves to the thin line indicating $\delta_{se}\left[V\right] = 1$ indicates the importance of δ_{se} in setting the minimum breakdown threshold. As an example, an equivalent tungsten frustum shield breakdown contour is plotted as a dashed gray line.

Fig. 6.4 shows the expected breakdown threshold dependences on A_{proj}/A_{tot} , T_{SOL}, and n_s/n_{SOL} is less decisive, though marginal increases in voltage breakdown can in principle be obtained by changing these parameters. Minimizing exposed fraction A_{proj}/A_{tot} improves standoff, and this strategy has been implemented in experiment. It is <10% for rings in Fig. 6.4, which magnetically 'shadow' each other, and declines away from the injector cathode, resulting in a 'voltage division' effect converging toward unperturbed V_{float}. The frustum shield has the largest, least favorable exposed area fraction, $A_{proj}/A_{tot} \approx 0.3$, and shows the lowest breakdown voltage. The ratio n_s/n_{SOL} is clearly an unknown that is difficult to measure or manipulate, but only changes the threshold by a factor of two over several orders of magnitude, and any value greater than several 0.1% yields estimates consistent with experimental breakdown voltage range, $V_{inj} \sim 1\,\mathrm{kV} - 2\,\mathrm{kV}$.

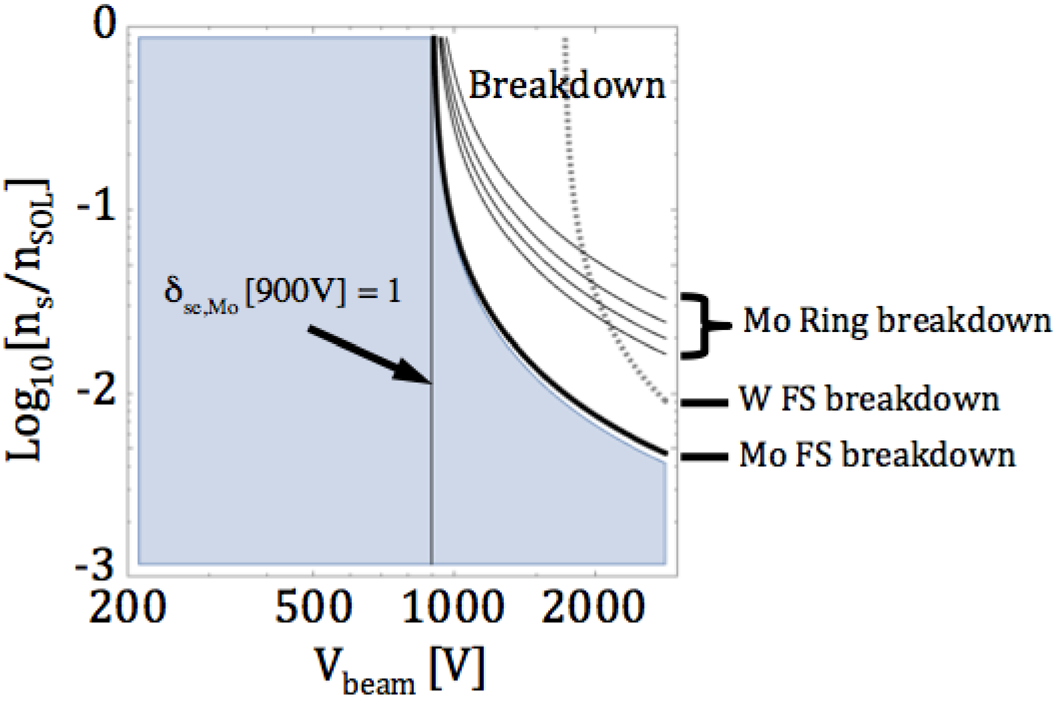

Figure 6.4: Molybdenum frustum shield (FS): Experimentally relevant $0 > V_{float} > -40\,\mathrm{V}$ region is shaded blue. Thick black contour indicates $V_{float} \rightarrow V_{beam}$ breakdown condition from text. Molybdenum rings: Thin black contours indicate breakdown condition for rings in design depicted in Fig. 6.1. Gray, dashed contour is breakdown condition for a tungsten frustum shield. Voltage where molybdenum δse=1 is indicated.

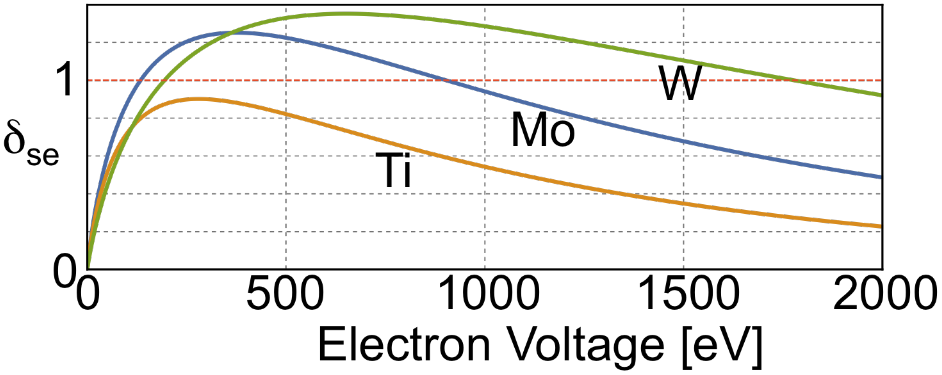

Figure 6.5: Secondary electron emission coefficients for Ti, Mo, W. From [8].

Observed Injector Breakdown Behavior

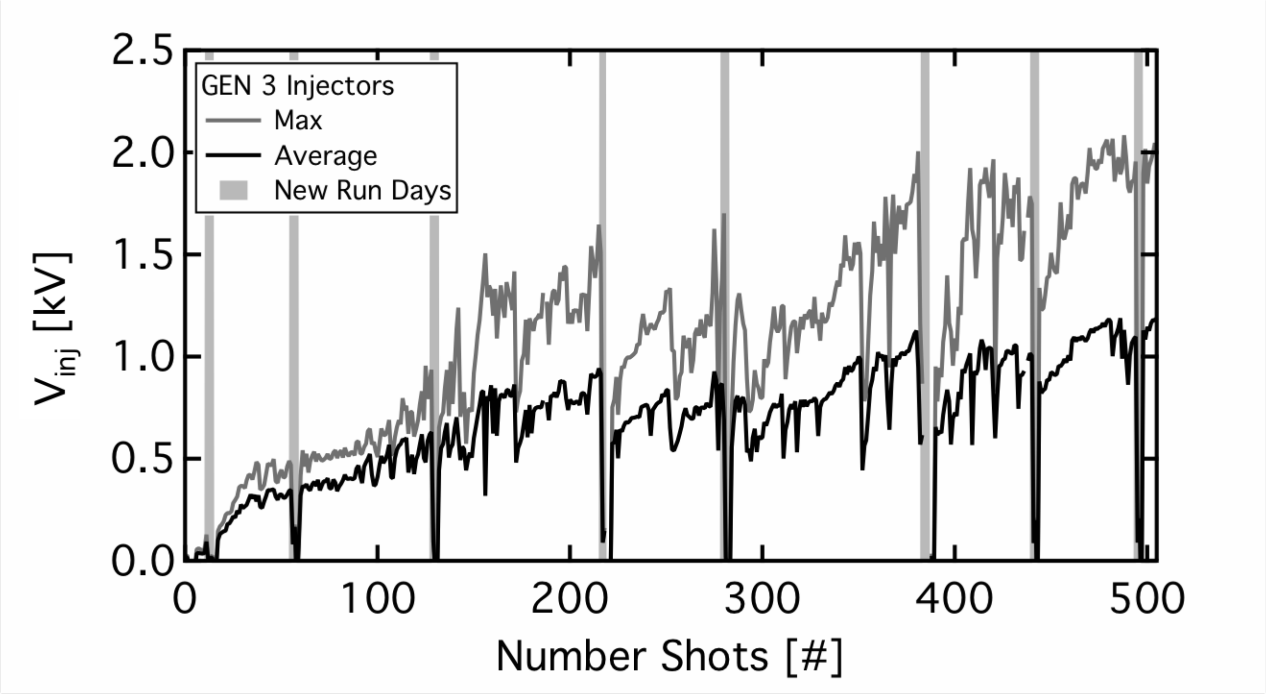

Figure 6.6: Achieved max and average V_{inj} for LHI discharges as a function of time during conditioning sequence of injectors design depicted in Fig. 6.1. Vertical bars indicate end of day.

Improvements in cleanly achievable V_{inj} without breakdown of floating components are observed to occur over a period of conditioning after a vent. These are in turn consistent with experimental 'conditioning' trends observed in $\delta_{se}[V]$, which show the high voltage $\delta_{se}[V] = 1$ condition to move to greater voltages after conditioning – from 1050V (partially conditioned) to 1450V (fully conditioned) in data from [132].

Experimental breakdown trends in LHI data have this general magnitude and trend behavior, as depicted in Fig. 6.6. Additionally, titanium gettering is used in Pegasus for vacuum quality, and getting is applied for periods of approximately an hour each morning before plasma operations begin. Fig. 6.5 indicates deposited layers of Ti might also reduce standoff by reducing $\delta_{se}[V]$.

Tungsten, due to greater $\delta_{se}[V]$ at high voltages ($\delta_{se}[1800\text{V}] = 1$, this quantity for W is plotted in Fig. 6.5), is expected to be more resistant to charging, and is therefore a promising next choice for floating components, as it also satisfies requirements for PFC-compatibility, heat-resistance and general durability. Initial steps to test W components are being made.

The source of electron bombardment of injector structures, apparently on the ion drift side, is not immediately clear. While hot impurity ions are observed during LHI, fast cameras often show a field-projected footprint on the injector structures consistent with the size scale of the an electron gyroradius: $\rho_e\,(10\,\text{eV} - 10\,\text{keV}) \sim 0.1\,\text{mm} - 1\,\text{mm}$ (see Fig. 6.2), whereas even deuterium ions would be expected to form a more diffuse footprint, that is not field-projected.

It is possible a small fraction of particles are reflected from a downfield inboard region. If sheath acceleration is not sufficiently field-aligned, or if injected electrons experience large-angle scattering, a single particle framework dictates that they will reflect from the high-field region via conservation of the 1st adiabatic invariant, returning to the injector's 'ion-side' plasma-facing surfaces. While sheath acceleration is likely close enough to field-alignment (within $\arcsin\left(\sqrt{B_{min}/B_{max}}\right) \sim 30°$ of field alignment is sufficient to avoid reflection), even for field-parallel acceleration, the Lorentz collision model gives $\nu_{coll} \approx 5 \times 10^3\ \text{s}^{-1}$ for a $V_{inj} = 1\,\text{kV}$ electron in a 10eV, 10^{18}m^{-3} D plasma, resulting in large-angle scattering event over a single circumference of the vessel, $2\pi R_{inj}$, for, as a fraction n_s/n_b of all particles exiting the injector:

$$\frac{n_s}{n_b} = \frac{L\nu_{coll}}{v_{drift}} = \frac{(2\pi R_{inj})\nu_{coll}}{\sqrt{2 \cdot eV_{inj}/m_e}} \sim 0.1\% \tag{6.5}$$

Since the density n_b of particles launched from the injector is near edge (and scrape-off layer) densities, $n_b \approx n_{SOL}$, then we conclude that n_s/n_{SOL} is of the order anticipated to cause breakdown of floating components in the foregoing model.

Bibliography

[1] O'Bryan J B 2014 *Numerical Simulation of Non-Inductive Startup of the Pegasus Toroidal Experiment* Ph.D. thesis University of Wisconsin-Madison Madison, WI

[2] Goertz C K and Joyce G 1975 *Astrophysics and Space Science* **32** 165–173

[3] Anders A 1999 *Surface and Coatings Technology* **120-121** 319–330 ISSN 0257-8972

[4] Zhao W, Koch A, Bauder U and Behrisch R 1984 *Journal of Nuclear Materials* **128-129** 613–617 ISSN 0022-3115

[5] Rohde V, Balden M, Lunt T and Upgrade Team t A 2009 *Physica Scripta* **T138** 014024 ISSN 0031-8949, 1402-4896

[6] Rohde V 2010 Tungsten Erosion by Arcs in ASDEX Upgrade (San Diego)

[7] Rohde V, Endstrasser N, Toussaint U, Balden M, Lunt T, Neu R, Hakola A and Bucalossi J 2011 *Journal of Nuclear Materials* **415** S46–S50 ISSN 0022-3115

[8] Langley R, Bohdansky J, Eckstein W, Mioduszewski P, Roth J, Taglauer E, Thomas E, Verbeek H and Wilson K 1984 *Nuclear Fusion* **24** S9–S117 ISSN 0029-5515, 1741-4326

[9] Peng Y K M, Fogarty P J, Burgess T W, Strickler D J, Nelson B E, Tsai J, Neumeyer C A, Bell R, Kessel C, Menard J, Gates D, LeBlanc B, Mikkelsen D, Fredrickson E, Grisham L, Schmidt J, Rutherford P, Sabbagh S, Field A, Sykes A, Cook I, Mitarai O and Takase Y 2005 *Plasma Physics and Controlled Fusion* **47** B263 ISSN 0741-3335

[10] Peng Y K and Strickler D 1986 *Nuclear Fusion* **26** 769–777 ISSN 0029-5515, 1741-4326

[11] Garstka G, Diem S, Eidietis N, Fonck R, Lewicki B, Taylor G, Battaglia D, Bongard M, Frost M, Kujak-Ford B, Squires B and Winz G 2006 *Nuclear Fusion* **46** S603–S612 ISSN 0029-5515, 1741-4326

[12] Sovinec C R and Prager S C 1996 *Physics of Plasmas* **3** 1038–1046 ISSN 1070664X

[13] Sovinec C R, Cohen B I, Cone G A, Hooper E B and McLean H S 2005 *Physical Review Letters* **94** 035003

[14] Jarboe T R, Wysocki F J, Fernandez J C, Henins I and Marklin G J 1990 *Physics of Fluids B: Plasma Physics* **2** 1342 ISSN 08998221

[15] O'Bryan J B, Sovinec C R and Bird T M 2012 *Physics of Plasmas* **19** 080701–080701–4 ISSN 1070664X

[16] Berger M A 1999 *Plasma Physics and Controlled Fusion* **41** B167–B175 ISSN 0741-3335, 1361-6587

[17] Boozer A H 1986 *Physics of Fluids* **29** 4123–4130 ISSN 00319171

[18] Taylor J B 1986 *Reviews of Modern Physics* **58** 741–763

[19] Battaglia D J 2009 *Non-Solenoidal Tokamak Startup Using Localized Current Sources Near The Outboard Midplane* Ph.D. thesis University of Wisconsin-Madison Madison, WI

[20] Battaglia D, Bongard M, Fonck R and Redd A 2011 *Nuclear Fusion* **51** 073029 ISSN 0029-5515, 1741-4326

[21] Jensen T H and Chu M S 1984 *Physics of Fluids* **27** 2881 ISSN 00319171

[22] Battaglia D, Bongard M, Fonck R and Redd A 2011 *Nuclear Fusion* **51** 073029 ISSN 0029-5515

[23] Child C D 1911 *Physical Review (Series I)* **32** 492–511

[24] Langmuir I 1913 *Physical Review* **2** 450–486

[25] Langmuir I 1929 *Physical Review* **33** 954

[26] Miller R B 1982 *An Introduction to the Physics of Intense Charged Particle Beams* (New York: Plenum Press) ISBN 0-306-40931-3

[27] Hershkowitz N 1985 *Space Science Reviews* **41** 351–391

[28] Raadu M A 1989 *Physics Reports* **178** 25–97 ISSN 0370-1573

[29] Oks E 2006 *Plasma Cathode Electron Sources* (Weinheim, Germany: Wiley-VCH Verlag) ISBN 978-3-527-40634-0

[30] Brown I G 2005 *The Physics and Technology of Ion Sources* 2nd ed (Wiley-VCH Verlag) ISBN 978-3-527-60395-4

[31] Smith R A 1982 *Physica Scripta* **T2A** 238–251 ISSN 0031-8949

[32] Maskrey J T and Dugdale R A 1966 *British Journal of Applied Physics* **17** 1025–1034 ISSN 0508-3443

[33] Goebel D and Schneider A 2005 *Plasma Science, IEEE Transactions on* **33** 1136–1148 ISSN 0093-3813

[34] Schwirzke F 1991 *IEEE Transactions on Plasma Science* **19** 690–696 ISSN 0093-3813

[35] Lenef A, Budinger B and Peters C 2002 *IEEE Transactions on Plasma Science* **30** 208–218 ISSN 0093-3813

[36] Mesyats G A 2005 *Pulsed Power* (New York: Springer) ISBN 0-306-48653-9

[37] Engel A 1965 *Ionized Gases* 2nd ed (Oxford: Oxford: Clarendon)

[38] Mesyats G A 2005 *Plasma Physics and Controlled Fusion* **47** A109–A151 ISSN 0741-3335

[39] Bugaev S P, Litvinov E A, Mesyats G A and Proskurovskiĭ D I 1975 *Soviet Physics Uspekhi* **18** 51–61 ISSN 0038-5670

[40] Juettner B 2001 *J. Phys. D: Appl. Phys.* **34** 103

[41] Boxman R L and Zhitomirsky V N 2006 *Review of Scientific Instruments* **77** 021101 ISSN 00346748

[42] Lefort A and Abbaoui M 2012 *IOP Conference Series: Materials Science and Engineering* **29** 012006 ISSN 1757-899X

[43] George H M 1976 *Journal of Nuclear Materials* **63** 331–336 ISSN 0022-3115

[44] Vogel N 1993 *Journal of Physics D: Applied Physics* **26** 1655–1661 ISSN 0022-3727, 1361-6463

[45] Anders A 2002 *Vacuum* **67** 673–686 ISSN 0042-207X

[46] Juttner B 1984 *Plasma Physics and Controlled Fusion* **26** 249–258 ISSN 0741-3335

[47] Boxman R L, Sanders D M and Martin P J 1995 *Handbook of Vacuum Arc Science and Technology* (Park Ridge, New Jersey: Noyes Publication) ISBN 0-8155-1375-5

[48] Kimblin C W 1973 *Journal of Applied Physics* **44** 3074 ISSN 00218979

[49] Wesson J 1997 *Tokamaks* 2nd ed (*Oxford Engineering Science Series* no 48) (Oxford: Oxford University Press)

[50] Rakhovskii V I 1976 *IEEE Transactions on Plasma Science* **4** 81–102 ISSN 0093-3813

[51] Robson A E and Thonemann P C 1959 *Proceedings of the Physical Society* **73** 508 ISSN 0370-1328

[52] McCracken G M 1980 *Journal of Nuclear Materials* **93-94, Part 1** 3–16 ISSN 0022-3115

[53] Schwirzke F, Hallal M and Maruyama X 1993 *Plasma Science, IEEE Transactions on* **21** 410–415 ISSN 0093-3813

[54] Schwirzke F and Taylor R 1980 *Journal of Nuclear Materials* **93-94, Part 2** 780–784 ISSN 0022-3115

[55] Jüttner B 2001 *Journal of Physics D: Applied Physics* **34** R103–R123 ISSN 0022-3727, 1361-6463

[56] Hintze W and Laux M 1981 *Beiträge aus der Plasmaphysik* **21** 247–260 ISSN 1521-3986

[57] Chaly A M 2005 *IEEE Transactions on Plasma Science* **33** 1497– 1503 ISSN 0093-3813

[58] Robson A E and von Engel A 1956 *Physical Review* **104** 15–16

[59] Robson A E 1960 The motion of an arc in a magnetic field

[60] Barengolts S A, Litvinov E A, Sadovskaya E Y and Shmelev D L 1998 *Technical Physics* **43** 668–672 ISSN 1063-7842, 1090-6525

[61] Litvinov E A 1990 *Sov. Phys. - Tech. Phys. Lett.* **16** 92

[62] Garner A L 2008 *Applied Physics Letters* **92** 011505 ISSN 00036951

[63] Saksaganskii G 1994 *Getter and Getter-Ion Vacuum Pumps* (Routledge) ISBN 978-3-7186-5668-4

[64] Wroe H 1958 *British Journal of Applied Physics* **9** 488–491 ISSN 0508-3443

[65] Boxman R L, Beilis I I, Gidalevich E and Zhitomirsky V N 2005 *IEEE Transactions on Plasma Science* **33** 1618– 1625 ISSN 0093-3813

[66] Unterberg E A, Battaglia D J, Bongard M W, Eidietis N W, Fonck R J, Frost M J, Garstka G D, Kujak-Ford B A, Lewicki B T, Squires B J and Winz G R 2006 *Journal of Fusion Energy* **26** 221–225 ISSN 0164-0313, 1572-9591

[67] Eidietis N W, Fonck R J, Garstka G D, Unterberg E A and Winz G R 2007 *Journal of Fusion Energy* **26** 43–46 ISSN 0164-0313

[68] Redd A J, Battaglia D J, Bongard M W, Fonck R J, Hinson E T, Kujak-Ford B A, Lewicki B T, Sontag A C and Winz G R 2008 *Journal of Fusion Energy* **28** 203–207 ISSN 0164-0313, 1572-9591

[69] Battaglia D J, Bongard M W, Fonck R J, Redd A J and Sontag A C 2008 *Journal of Fusion Energy* **28** 140–143 ISSN 0164-0313, 1572-9591

[70] Battaglia D J, Bongard M W, Fonck R J, Redd A J and Sontag A C 2009 *Physical Review Letters* **102** 225003

[71] Wise P, Lesch B, Muntau H, Intrator T, Fonck R and Winz G 1998 *Physica B: Condensed Matter* **246-247** 350–352 ISSN 0921-4526

[72] Redd A J, Battaglia D J, Bongard M W, Fonck R J, Hinson E T, Kujak-Ford B A, Lewicki B T, Sontag A C and Winz G R 2008 *Journal of Fusion Energy* **28** 203–207 ISSN 0164-0313, 1572-9591

[73] Den Hartog D J, Craig D J, Fiksel G and Sarff J S 1997 *Plasma Sources Science and Technology* **6** 492

[74] Fiksel G, Almagri A F, Craig D, Iida M, Prager S C and Sarff J S 1996 *Plasma Sources Science and Technology* **5** 78–83 ISSN 0963-0252, 1361-6595

[75] Fiksel G 1991 *Ph.D Thesis: Experimental Simulation of a Gaseous Divertor* Ph.D. thesis University of Wisconsin-Madison Madison, WI

[76] Davydenko R I, Morozov I I, Roslyakov G V and Savkin V Y 1987 *Instrum. Exp. Tech.* **29** 6

[77] Davydenko V I, Dimov G I, Morozov I I and Rosliakov G V 1983 *(Zhurnal Tekhnicheskoi Fiziki, vol. 53, Feb. 1983, p. 258-263) Soviet Physics - Technical Physics (ISSN 0038-5662), vol. 28, Feb. 1983, p. 160-163. Translation.* **53** 258–263 ISSN 0044-4642

[78] Dimov G I and Roslyakov G V 1974 *Sov. Prib. Tech. Exp.* **1** 29

[79] I V Kandaurov, Astrelin, V T, Burdakov, A V, Derevyankin, G E and Trunev, Yu A 2008 Study of Intensive Long-Pulse Electron Beam Generation in a Source with Arc Plasma Emitter *15th SHCE Proceedings* Intense Electron and Ion Beams (Tomsk, Russia) pp 121–124

[80] Belchenko Y I, Davydenko V I, Derevyankin G E, Dimov G I, Dudnikov V G, Morosov I I, Roslyakov G V and Schabalin A L 1990 *Review of Scientific Instruments* **61** 378 ISSN 00346748

[81] Vijvers W A J, Schram D C, Shumack A E, Lopes Cardozo N J, Rapp J and van Rooij G J 2010 *Plasma Sources Science and Technology* **19** 065016 ISSN 0963-0252, 1361-6595

[82] Shkol'nik S M 2011 *Plasma Sources Science and Technology* **20** 013001 ISSN 0963-0252

[83] Parker R K 1974 Explosive Electron Emission and the Characteristics of High-Current Electron Flow Technical Report AFWL-TR-73-92 Air Force Weapons Laboratory Kirtland Air Force Base

[84] Ferreira C M and Delcroix J L 1978 *Journal of Applied Physics* **49** 2380 ISSN 00218979

[85] Delcroix J L and Trindade A R 1974 *Advances in Electronics and Electron Physics* **Volume 35** 87–190

[86] Humphries S, Coffey S, Savage M, Len L K, Cooper G W and Woodall D M 1985 *Journal of Applied Physics* **57** 709 ISSN 00218979

[87] Humphries S 1990 *Charged particle beams* (Wiley) ISBN 978-0-471-60014-5

[88] Witalis E A 1981 *Physical Review A* **24** 2758–2764

[89] Putnam S D 1972 Theoretical Studies of Intense Relativistic Electron Beam-Plasma Interactions Final Report PIFR-72-105 Defense Nuclear Agency DNA 2849F (PIFR-72-105) Washington, D.C. dNA-2849F

[90] Lawson J D 1959 *Journal of Nuclear Energy. Part C, Plasma Physics, Accelerators, Thermonuclear Research* **1** 31–35 ISSN 0368-3281

[91] Guo-Zhi L, Wen-Hua H and Zhan-Feng Y 2005 *Chinese Physics* **14** 949–952 ISSN 1009-1963, 1741-4199

[92] Jones M E and Thode L E 1980 *Journal of Applied Physics* **51** 5212–5214 ISSN 00218979

[93] Liu G Z, Yang Z F, Sun J and Zhang Y P 2009 *Plasma Science, IEEE Transactions on* **37** 2048 –2054 ISSN 0093-3813

[94] Sheffield R L, Montgomery M D, Parker J V, Riepe K B and Singer S 1982 *Journal of Applied Physics* **53** 5408–5413 ISSN 00218979

[95] Di Capua M, Creedon J and Huff R 1976 *Journal of Applied Physics* **47** 1887–1896 ISSN 00218979

[96] Goldstein S A, Cooperstein G, Lee R, Mosher D and Stephanakis S J 1978 *Physical Review Letters* **40** 1504–1507

[97] Guo-Zhi L, Wen-Hua H, Hao S and Ren-Zhen X 2006 *Chinese Physics* **15** 600–603 ISSN 1009-1963, 1741-4199

[98] Quintenz J P and Poukey J W 1977 *Journal of Applied Physics* **48** 2287–2293 ISSN 00218979

[99] Swanekamp S B, Stephanakis S J, Grossmann J M, Weber B V, Kellogg J C, Ottinger P F and Cooperstein G 1993 *Journal of Applied Physics* **74** 2274–2286 ISSN 00218979

[100] Swanekamp S B, Commisso R J, Cooperstein G, Ottinger P F and Schumer J W 2000 *Physics of Plasmas* **7** 5214–5222 ISSN 1070664X

[101] Cooperstein G and Condon J J 1975 *Journal of Applied Physics* **46** 1535–1538 ISSN 00218979

[102] Goldstein S A, Davidson R C, Siambis J G and Lee R 1974 *Physical Review Letters* **33** 1471–1474

[103] Li L, Men T, Liu L and Wen J 2007 *Journal of Applied Physics* **102** 123309–123309–6 ISSN 00218979

[104] Yonas G, Poukey J, Prestwich K, Freeman J, Toepfer A and Clauser M 1974 *Nuclear Fusion* **14** 731–740 ISSN 0029-5515, 1741-4326

[105] Bailey V L, Creedon J M, Ecker B M and Helava H I 1983 *Journal of Applied Physics* **54** 1656–1665 ISSN 00218979

[106] Burdovitsin V and Oks E 2008 *Laser and Particle Beams* **26** 619–635

[107] Burdovitsin V and Oks E 1999 *Review of Scientific Instruments* **70** 2975 ISSN 00346748

[108] Oks E M and Schanin P M 1999 *Physics of Plasmas* **6** 1649 ISSN 1070664X

[109] Oks E M 1992 *IOPscience Plasma Sources Science and Technology* **1** 249

[110] Ozur G 2009 *Plasma Science, IEEE Transactions on* **37** 1897 –1900 ISSN 0093-3813

[111] Ozur G, Popov S and Fedushchak V 2008 *Technical Physics* **53** 919–926 ISSN 10637842

[112] OZUR G, PROSKUROVSKY D, ROTSHTEIN V and MARKOV A 2003 *Laser and Particle Beams* **21** 157–174

[113] Hamagaki M, Hara T, Sadamoto Y and Ohgo T 1995 *Review of Scientific Instruments* **66** 3469 ISSN 00346748

[114] Furno I, Intrator T P, Hemsing E W, Hsu S C, Abbate S, Ricci P and Lapenta G 2005 *Physics of Plasmas (1994-present)* **12** 055702 ISSN 1070-664X, 1089-7674

[115] Zielinski J J, Meiden H J v d, Morgan T W, Schram D C and Temmerman G D 2012 *Plasma Sources Science and Technology* **21** 065003 ISSN 0963-0252, 1361-6595

[116] Rapp J, Koppers W R, van Eck H J N, van Rooij G J, Goedheer W J, de Groot B, Al R, Graswinckel M F, van den Berg M A, Kruyt O, Smeets P, van der Meiden H J, Vijvers W, Scholten J, van de Pol M, Brons S, Melissen W, van der Grift T, Koch R, Schweer B, Samm U, Philipps V, Engeln R A H, Schram D C, Lopes Cardozo N J and Kleyn A W 2010 *Fusion Engineering and Design* **85** 1455–1459 ISSN 0920-3796

[117] Vella M 1981 *Nuclear Instruments and Methods in Physics Research* **187** 313–321 ISSN 0167-5087

[118] Maenchen J, Cooperstein G, O'Malley J and Smith I 2004 *Proceedings of the IEEE* **92** 1021 – 1042 ISSN 0018-9219

[119] Hugel H 1980 *IEEE Transactions on Plasma Science* **8** 437 –442 ISSN 0093-3813

[120] Raizer Y P 1991 *Gas Discharge Physics* (Moscow: Springer) ISBN 978-3-642-64760-4

[121] Janev R K, Langer W, Evans K and Post D 1987 *Elementary Processes in Hydrogen-Helium Plasmas, Cross Sections and Reaction Rate Coefficients* (Spring-Verlag) ISBN 978-0-387-17588-1

[122] Janev R, Post D, Langer W, Evans K, Heifetz D and Weisheit J 1984 *Journal of Nuclear Materials* **121** 10–16 ISSN 0022-3115

[123] Sontag A C 2002 *Determination of Equilibrium and Stability Characteristics of low-A ST plasmas in the PEGASUS Toroidal Experiment* Ph.D. thesis UW Madison Madison, WI

[124] Fonck R J, Ramsey A T and Yelle R V 1982 *Applied Optics* **21** 2115–2123

[125] Hutchinson I H 2002 *Principles of Plasma Diagnostics* 2nd ed (Cambridge: Cambridge University Press) ISBN 978-0-521-67574-1

[126] Mijatovic Z, Nikolic D, Kobilarov R and Ivkovic M 2010 *Journal of Quantitative Spectroscopy and Radiative Transfer* **111** 990–996 ISSN 0022-4073

[127] Intrator T P, Sun X, Lapenta G, Dorf L and Furno I 2009 *Nature Physics* **5** 521–526 ISSN 1745-2473

[128] Rosenblum M and Kurths J 1998 Analysing Synchronization Phenomena from Bivariate Data by Means of the Hilbert Transform *Nonlinear Analysis of Physiological Data* (Springer) pp 91–99

[129] Hemsing E, Furno I and Intrator T 2005 *IEEE Transactions on Plasma Science* **33** 448–449 ISSN 0093-3813

[130] Hemsing E, Furno I, Intrator T and Wei D 2004 *Review of Scientific Instruments* **75** 4106–4108 ISSN 0034-6748, 1089-7623

[131] Furno I, Intrator T, Torbert E, Carey C, Cash M D, Campbell J K, Fienup W J, Werley C A, Wurden G A and Fiksel G 2003 *Review of Scientific Instruments* **74** 2324–2331 ISSN 0034-6748, 1089-7623

[132] Petry R L 1925 *Physical Review* **26** 346–359